

Small Electrical, Mechanical, and Biomechanical Systems of Electromagnetic Radiation

by

Navid Barani Lonbani

A dissertation submitted in partial fulfillment
of the requirements for the degree of
Doctor of Philosophy
(Electrical Engineering)
in the University of Michigan
2021

Doctoral Committee:

Professor Kamal Sarabandi, Chair
Professor Theodore B. Norris
Professor Leung Tsang
Professor Angela Violi

Navid Barani Lonbani

nbarani@umich.edu

ORCID iD: 0000-0002-7835-5982

© Navid Barani Lonbani 2021

To my beloved family

Acknowledgements

First and foremost, I would like to express my sincere gratitude to my advisor, Professor Kamal Sarabandi, for his believing in me and providing me this unique opportunity to work with him and conduct research in the field of applied electromagnetics. None of this work would have been possible without his continuous guidance, support, and encouragement throughout this journey. Beside a great advisor and mentor, he has been truly a great friend and also lifelong inspiration for me.

I am also deeply thankful to my other committee members, Prof. Theodore B. Norris, Prof. Angela Violi, and Prof. Leung Tsang for their insightful comments and valuable suggestions on my thesis to make it a more complete work. Additionally, I am appreciative of the RadioBio team at the University of Michigan for constructive discussions on my research. None of my fabrication and measurements works were possible without the invaluable help of Dr. Adib Nashashibi. I like to take this opportunity and express my gratitude to him as well.

Special thanks are going to my former and current fellow lab-mates in the Radiation Laboratory for their friendship and sharing views and thoughts on my research. You all deserve all the accolades for your persistently-creative works. I am also immensely thankful to my dear friends in Ann Arbor, who made Ann Arbor as my second hometown after Isfahan. I would never forget all the wonderful moments we had together.

Above all, I like to express my deepest appreciation to my parents, Batoul and Hamidreza for their endless love and support. They are the ones who encouraged me to reach for my goals

and aim high. I certainly owe all my accomplishments to them. Finally, a big thank you goes to my dearest younger brother, Nima, who has been always a great friend and support for me.

Navid

December 2020

Ann Arbor

Table of Contents

Dedication	ii
Acknowledgements.....	iii
List of Figures.....	viii
List of Tables	xv
List of Appendices	xvi
Abstract	xvii
CHAPTER 1 Introduction.....	1
1.1. Recent Advances on Efficient, Low-Frequency, and Small Antennas Design.....	2
1.1.1. Mechanical Antennas.....	2
1.1.2. Fragmented Antennas	6
1.2. Background and Motivation for Electromagnetic Signaling among Biological Cells.....	9
1.3. Dissertation Overview And Contributions	13
CHAPTER 2 Mechanical Antennas.....	17
2.1. Introduction.....	17
2.2. Field Equations and Numerical Simulations for Rotating Magnets.....	20
2.2.1. Far-Field Analysis.....	20
2.2.2. Near-Field Numerical Simulations	23
2.3. Theory of the Proposed Phase Modulation and Frequency Multiplication.....	25
2.3.1. The Concept	25
2.3.2. Near-Field Numerical Simulations and Parametric Studies	28
2.3.3. Far-Field Semi-Analytical Simulations	32
2.4. Fabrication Process and Measurement Results	37
2.4.1. Fabrication Process using 3D Printing.....	37
2.4.2. Signal Integrator for Magnetic Field Profile Detection	38

2.4.3. Trigger Signal for Phase Modulation Characterization	40
2.4.4. Measurement Results and Discussions	41
2.5. Conclusion.....	47
CHAPTER 3 Fragmented Antennas	49
3.1. Introduction	49
3.2. Proof of Concept and Design Approach	52
3.2.1. Single Antenna Design Considerations	52
3.2.2. Coupling Mechanisms in Fragmented Coupled Antenna	55
3.2.3. Fragmented Antenna Design Methodology	57
3.2.4. Sensitivity Analysis	61
3.2.5. Platform Effects on Fragmented Antenna’s Performance	65
3.2.6. Tunable Matching Circuit.....	66
3.3. Fabrication and Measurement Results	67
3.4. Conclusion	73
CHAPTER 4 Electromagnetic-based Communication among Biological Cells	74
4.1. Introduction	74
4.2. Source of EM Signal Emission In Biofilms.....	77
4.2.1. Structural Mechanics Analysis of Single Amyloid Fibril and Cells.....	78
4.2.2. Amyloid Fibrils Community as EM-Coupled Mechanical Oscillators.	82
4.2.3. Mathematical Analysis of EM-coupled Mechanical Oscillators	83
4.2.4. Possible EM-based Communication Frequencies and Synchronization Level.....	87
4.3. Multiphysics Model of EM Communication within Biofilms	95
4.3.1. Purposeful EM Communication Hypothesis.	95
4.3.2. COMSOL Simulation for Purposeful Communication.....	99
4.4. Comparative Study between EM Signaling and Quorum Sensing (QS) in Biofilms:	
Communication Data Rate	103
4.4.1. EM-Based Channel Capacity Estimation.....	104
4.4.2. QS Channel Modeling.....	107
4.4.3. Results and Comparative Study	111
4.5. Conclusion.....	114
CHAPTER 5 Conclusion and Future Directions	116

5.1. Research Summary and Contributions	116
5.2. Recommended Future Works	117
5.2.1. Mechanical Antennas	117
5.2.2. Fragmented Antennas	118
5.2.3. Multiphysics Modeling of EM Signaling among Biological Cells.....	120
5.3. Closing	122
APPENDICES	123
BIBLIOGRAPHY.....	135

List of Figures

Figure 1.1. Attenuation constant as a function of frequency associated with EM waves propagating in the seawater ($\sigma = 4 \text{ S/m}$).....	4
Figure 1.2. (a) 2-D view of signal transmission into seawater using a magnetic short dipole above the surface of water. The transmitted magnetic field into the water by a magnetic dipole moment at (b) 10 kHz and (c) 200 Hz. All the field profiles are normalized to the corresponding maximum field at the boundary.	5
Figure 1.3. U.S. Navy’s VLF antennas at Cutler, Maine. Current VLF transmitters have length scales of many kilometers.....	6
Figure 1.4. Coverage maps of point-to-point wireless communication at low-VHF (40 MHz) and at 2.4 GHz (enabled by a ZigBee radio) in non-line-of-sight multi-floor indoor to outdoor scenario.	8
Figure 1.5. Swarming drones in different configurations [55]. Recent advances on autonomous control has enabled arbitrary flight formations for UAVs.....	9
Figure 1.6. Concept of fragmented antenna formed by many electromagnetically-coupled small antennas on a cluster of UAVs.....	9
Figure 1.7: SEM image of bacterial biofilms. (a) Staphylococcus aureus biofilm. (b) Pseudomonas aeruginosa biofilm. The bacterial cells in a biofilm are supported by the EPS matrix.....	13
Figure 1.8. Overview of the topics that are covered in this dissertation.....	15
Figure 2.1. (a): Rotating cylindrical permanent magnet (around z-axis) represents a mechanical antenna. θ and φ are representation of the observation point in spherical coordinate system. (b) 2D top view of the rotating magnet. (c): Equivalent magnetic dipole representation of the rotating magnet. (d): Equivalent magnetic current model associated with the rotating magnet.	21
Figure 2.2. (a): Time profile of near-field \mathbf{B} at a point along the x axis (25 cm away from the magnet’s center). The \mathbf{B} -field components have frequency of 50 Hz. (b): Near-field components of magnetic field (\mathbf{B}) as a function of distance along the x -axis. The solid lines are the numerical results and the dashed lines represent the analytical solution.....	24
Figure 2.3. Main idea (desired solution) for achieving phase modulation. Each curve represents an amplitude-modulated sinusoidal signal shifted in the time domain (having a distinguished phase).	26

Figure 2.4. (a): Three dimensional proposed configuration for achieving phase modulation and frequency multiplication in a mechanical antenna. The rotating magnet is sandwiched between two pairs of orthogonal bow-tie shape high- μ magnetic plates. φ_0 is measured between the point A and the x -axis (b): Its side view..... 26

Figure 2.5. (a): An electric dipole is brought in the proximity of a dielectric sphere with large permittivity. The separation distance between the charges and the sphere is h . (b): Its equivalence based on the image theory for a special case when $h \rightarrow 0$. (c): Top-view of proposed configuration for achieving phase modulation (the rotating magnet is modeled as rotating magnetic dipole). (d): Comparison between desired and realizable amplitude modulation through using bow-tie shape magnetic plates (in one time period)..... 27

Figure 2.6. (a): Time domain radial magnetic field (Br) in the near-field region at a point along the x -axis for (a): various distances between the magnet and ferrite sheets (h), (b): various ferrite thicknesses ($t\mu$). Dashed line represents the corresponding magnetic field without the presence of magnetic plates..... 29

Figure 2.7. Fourier transform of the near-field Br with the time-domain profile given in Figure 2.6 ($h = 3$ mm, $t\mu = 5$ mm). 30

Figure 2.8. The effect of magnetic plates' initial position (φ_0) on the near-field Br . Variation of φ_0 gives a unique phase to the EM field. 31

Figure 2.9. The effect of magnetic posts initial position (φ_0) on the amplitude and phase of the frequency components of (a): Br fields and (b): $B\varphi$ fields. Changing the initial position of the magnetic posts, changes the phase corresponding to odd harmonics of the rotation frequency (50 Hz). All the phases are in degree. 31

Figure 2.10. (a): The application of uniqueness theorem for finding the far-field components of the rotating magnet integrated with ferrite sheets. (b): The Application of the uniqueness theorem when only the information about the magnetic field components exists..... 33

Figure 2.11. The application of reciprocity theorem for finding the radiation of a surface electric current over a PMC sphere. 34

Figure 2.12. The radiation pattern of the proposed mechanical antenna. (a): $E\theta$ ($H\varphi$), (b): $E\varphi$ ($H\theta$). The $E\theta$ has an isotropic radiation pattern. 35

Figure 2.13. (a): Three dimensional CAD model of proposed phase modulating and frequency multiplier mechanical antenna with all its plastic holders. (b): Its side view. (c): Its top view. The bottom ferrite plates are cut into trapezoidal shapes so as to let the DC motor shaft go through them and rotate the magnet. 38

Figure 2.14. Op-amp based integrator circuit used for detection of the time-domain profile of the magnetic field from the magnetic sensor output..... 39

Figure 2.15. The proposed technique for generating a reference signal to detect the phase-modulated signal. A small piece of black tape is used here to block the laser light illuminating a phototransistor from the top.....	41
Figure 2.16. Three dimensional view of the fabricated mechanical antenna with phase modulation and frequency multiplication capability. The size of the antenna is 10 cm×8.5 cm. The magnetic plates' plastic holder can independently rotate around the rotating magnet to provide the phase modulation scheme.	42
Figure 2.17. (a): Measured voltage using the magnetic probe for various φ_0 . (b): Numerically simulated received voltage by the probe. Pretty good agreement is observed.	43
Figure 2.18. Frequency spectrum of the received voltage by the magnetic probe. The frequency multiplication capability can be readily captured from this figure.	44
Figure 2.19. The measured time-domain profile of radial magnetic-field (Br) at $r=20$ cm for various φ_0 indicating phase modulation feature.	44
Figure 2.20. The measured (solid line) and simulated (dashed line) near-field Br as a function of distance (r). Higher harmonics have smaller decay rate compared to the fundamental frequency.	46
Figure 2.21. The measured voltage from the phototransistor circuit for various φ_0 (in four cycles). This signal is generated to trig the oscilloscope displaying signal sensed by the magnetic probe.	46
Figure 3.1. The proposed fragmented antenna concept for bandwidth enhancement of miniaturized antenna elements mounted on robotic flyers.	51
Figure 3.2. The configuration of an inductively end-loaded folded dipole antenna element on a thin printed circuit board.	53
Figure 3.3. The configuration of an inductively end-loaded folded dipole antenna element on a thin printed circuit board.	54
Figure 3.4. The normal magnetic and electric field intensities (along the axis of end-loads, x-axis) associated with the dipole, folded dipole, and 3-fold dipole antennas (all the fields are normalized to the maximum field value which is for the 3-fold dipole antenna).....	55
Figure 3.5. The different coupling mechanisms between the adjacent antennas in the fragmented antenna configuration (The end-loops are in the y-z plane and the x-axis is along the axis of the loops).....	56
Figure 3.6. The normal magnetic and electric field intensities (along the axis of end-loads) associated with the dipole arms and end-loads of single element antenna shown in Figure 3.2..	57

Figure 3.7. The performance analysis of the coupled antennas with optimized load and other possible load configurations in terms of (a): bandwidth, and (b): radiation efficiency. (The radiation efficiency is important only over the -10 dB return loss bandwidth).	60
Figure 3.8. The formation of double resonances in the fragmented antenna configuration.	61
Figure 3.9. The coupling (S_{21} or S_{31}) between the driver antenna and each of the two assistive antennas.....	62
Figure 3.10. (a): The separation distance effect on the bandwidth of the proposed coupled array configuration. (b): The variation of the real and the imaginary parts of the input impedance for different separation distances.....	62
Figure 3.11. The simulated radiation efficiency for different separation distances.....	63
Figure 3.12. The effect of misalignment of the inductive end-loads along the y-direction on the bandwidth of the proposed antenna configuration.....	64
Figure 3.13. The single inductively end-loaded folded dipole antenna mounted on a small dielectric-made ($\epsilon_r = 4$) quadcopter, (a): 3-D view, (b): top view.....	65
Figure 3.14. The simulation results for comparison between the performance of coupled antennas in the presence and absence of the platform.	66
Figure 3.15. The proposed tunable matching circuit containing a tuning diode (varactor).....	67
Figure 3.16. (a): Fabricated antennas inside anechoic chamber. (b): Fabricated tunable matching circuit integrated with the driver antenna.	68
Figure 3.17. The measured and simulated return loss for the different separation distances.	69
Figure 3.18. The measured and simulated peak-gain (in the boresight direction) over band for the different separation distances.....	69
Figure 3.19. Measured and simulated radiation pattern in E-plane (red) and H-plane (black) for three different frequencies (from left to right: 234 MHz, 240 MHz, 246 MHz) over the achieved frequency bandwidth (a): $d= 12$ cm, (b): $d= 14$ cm, (c): $d= 16$ cm. The solid lines are simulations and the dashed lines are measurements.	72
Figure 4.1. (a) SEM image of <i>Staphylococcus aureus</i> biofilm [126]. (b) Formation of amyloid fibrils as a result of charged peptides aggregation through hydrophobic and hydrophilic forces. The amyloid fibril will have a net dipole moment [127]. (c) Amyloid fibrils in composition with the extracellular matrix attached to the cell membrane (TEM image) [125]. The scale bar is $1\mu\text{m}$. (d) A 2D illustration of a biofilm with elastic amyloid fibrils (helical strings) playing the role of natural built-in antennas. The cells are represented by circles.	76
Figure 4.2. (a): A bacterial call and its attached amyloid fibril are modeled as a solid sphere and a beam for modal analysis. (b): Structural mechanics modal analysis on the amyloid fibril and cell.	

At low-frequencies, cantilever beam vibrational modes are observed for the fibrils within the kHz-MHz range. At higher frequencies, the cell's vibrational modes will combine with the higher order modes of the cantilever beam associated with the fibril and then complex mode configurations appears. The given resonant frequencies in the parenthesis are the ones obtained from the analytical solution which are in agreement with COMSOL FEM simulation. (c): Attached amyloid fibril to a cell can be treated as a cantilever beam having dipole charges at its ends. 79

Figure 4.3. Resonant frequency of amyloid fibril cantilever beam mode as a function of length for its first four modes. To have better understanding of resonant frequency values, the plot is divided into two separate plots with different length ranges. 80

Figure 4.4. (a): An elastic amyloid fibril connected to the EPS matrix and not attached to any cells can be modeled as a charged spring (longitudinal mode). (b): Transverse spring mode for the floating fibrils. (c): Amyloid fibril natural resonant frequency for spring vibrational mode (longitudinal vibration) as a function of length. (d): Amyloid resonant frequency for transverse spring vibration. 81

Figure 4.5. (a): Illustration of a biofilm including cells and amyloid fibrils. (b): EM-coupled system of mechanical oscillators representing interacting amyloid fibrils in a biofilm (cantilever beam mode). (c): Coupled spring vibrational mode for fibrils in biofilms. The arrows indicate the electromagnetic coupling existing between the charges of fibrils. 83

Figure 4.6. (a): The developed flowchart for generating non-intersecting fibrils (cylinders) inside a box. (b): One 3D realization for the developed algorithm. (c): Realization of a biofilm image with different volume fractions (φ_{max}). 88

Figure 4.7. (a): Possible resonant frequencies of electromagnetically-coupled amyloid fibrils (cantilever beam mode, $q = \pm 3e-$, $Q = 4$). (b): Relative amplitude of vibration of fibrils at one of those eigenfrequencies (13.6 kHz). (c): Relative amplitude of oscillation of fibrils at 3.3 kHz. 91

Figure 4.8. Impact of stronger dipole moment ($q = \pm 15e-$, $Q = 4$) on the synchronization and natural resonant frequencies. (a): Frequency spectrum. (b): The relative amplitude of fibrils' vibration is plotted at 8 kHz. (c): The relative amplitude of fibrils' vibration at 27.6 kHz. 92

Figure 4.9. Impact of lower quality factor ($q = \pm 3e-$, $Q = 2$) on the synchronization and natural resonant frequencies. (a): Frequency spectrum. The relative amplitude of fibrils' vibration are shown at (b): 3.4 kHz, and (c): 13.7 kHz. 93

Figure 4.10. (a): Possible resonant frequencies for the spring mode. (b): Relative amplitude of fibrils' oscillation for spring mode at 0.9 GHz. (c): Relative amplitude of fibrils oscillation for spring mode at 8.13 GHz. Only the initially-excited fibril vibrates and cannot couple to other fibrils. 94

Figure 4.11. Our hypothesis for electromagnetic-based communication between two transmitting (TX) and receiving (RX) biological cells. The vibration of charged amyloid fibrils caused by the cell will induce EM radiation. 96

Figure 4.12. Structural mechanics modal analysis on an individual bacterial cell (analytical and numerical simulation). The natural resonant frequencies of the first four modes are in the sub-GHz range. Close agreement between the analytical frequencies and COMSOL eigenfrequencies is achieved. The given values in the parenthesis are for the COMSOL simulation results..... 99

Figure 4.13. (a): 3D view of a bacterial cell with its attached amyloid fibril surrounded by water. The cell is experiencing an initial strain along the z –axis which in turn start vibrating and moving the amyloid fibril. The center of the TX and RX cells are located at $O(0,0,0)$ and $O'(0,0,1) \mu\text{m}$, respectively. (b): Time-domain profile of the applied strain to the cell. 100

Figure 4.14. (a): Vibration amplitude of the transmitting fibril’s ends at point A ($dA(t)$). (b): Vibration amplitude at point B ($dB(t)$). (c): Received electric by the RX cell at point O' . (d): Received electric field at point D . (e): FFT of the received electric field at point O' . (f): FFT of received E-field at point D . For the definition of points A , B , O' , and D , refer to Figure 4.13(a). 102

Figure 4.15. (a): Two individual cells are communication through either chemical messengers (autoinducers or ions) or EM waves. (b): Communication channel representation for these schemes. Individual cells are considered as transmitters and receivers..... 105

Figure 4.16. (a): Two cells communicate through EM waves by moving their hinged amyloid fibrils. (b): Its equivalent antenna system model as the dipole charges radiate through mechanical vibration of the amyloid fibrils. (c): Blackbody assumption for noise power estimation at the receiving cell..... 106

Figure 4.17. (a): Physical model proposed for estimating channel capacity of quorum sensing based on diffusion phenomena. (b): Its binary channel representation. (c): Brownian motion of one autoinducer released by the transmitting cell to be captured by the receiving cell as a purposeful message. The distance between two cells is Rd 108

Figure 4.18. The channel capacity estimation for QS as a function of the number of messenger molecules released by the transmitting cell ($N1$). (a): $Rd = 1 \mu\text{m}$ ($\tau c = 1.7 \text{ ms}$). (b): $R = 2 \mu\text{m}$ ($\tau c = 6.7 \text{ ms}$). Rd is the distance between the two communicating cells. The channel capacity estimation as a function of distance between two cells. (c): quorum sensing. (d): EM-based communication..... 113

Figure 5.1. The proposed idea for enhancing the far-field strength of mechanical antennas (rotating magnet) through using magneto-dielectric resonance concept. 118

Figure 5.2. Two electromagnetically-coupled antennas with inductive end-loads, (a): 3fold dipole antennas, (b): folded dipole antennas..... 119

Figure 5.3. Application of negative resistance in fragmented antenna for gain enhancement. .. 120

Figure 5.4. (a): Acoustically-coupled biological cells induce stronger electric field compared to an individual cells. (b): Simulated biofilm sample in COMSOL. 121

Figure 5.5. Impact of acoustic coupling between the cells on the emitted E-field from the biofilm sample at points (a): $(2,-2,5)\mu\text{m}$, and (b): $(2,-8,1)\mu\text{m}$. The coordinate system for these points is defined on Figure 5.4(b). The origin of the coordinate system is also shown in that figure. 121

Figure A.1. The periodic pulse function applied to modulate the pure sinusoidal EM signal from the rotating 125

Figure B.1. The simulation setup for quality factor estimation associated with the fibril vibration. (a): cantilever beam mode (vibration would be mainly along z axis). (b): mechanical spring mode (vibration is mainly along the y axis). Time-domain profile of amyloid fibril's open-end vibration with and without water background. (c): Cantilever beam mode. (d): spring mode. All the amplitudes are normalized to the corresponding one in the free-space. 128

Figure C.1. The short dipole embedded in a multi-layer magneto-dielectric sphere and its dual problem. (a): electric dipole problem . (b): magnetic dipole problem..... 130

Figure C.2. A magneto-dielectric sphere is illuminated by a plane wave. 131

Figure C.3. (a): A 2-layer magneto-dielectric sphere is illuminated by a plane wave. (b): The magneto-dielectric resonance condition for the EM fields at the center of the sphere. (c): A short electric dipole covered by the same multilayer magneto-dielectric sphere. (d): The ratio of far-fields of the dipole with and without the magneto-dielectric material. 132

Figure C.4. (a): The application of magneto-dielectric resonance for enhancing the radiated power from a rotating charged capacitor (electric dipole). (b): The field enhancement as a function of the relative permeability of the material ($\epsilon_r = 1$) covering the rotating capacitor. (c): The application of magneto-dielectric resonance for enhancing the radiated power from a rotating magnet. (d): The field enhancement as a function of the relative permittivity of the material ($\mu_r = 1$). 134

List of Tables

Table 2.1. Phase Variation of the Rotation Frequency Harmonics of the Near-Field for Different Values of φ_0 (with respect to $\varphi_0=0$).....	32
Table 2.2. Phase Variation of the Rotation Frequency Harmonics of the Far-Field EM Components for Different Values of φ_0 (with respect to $\varphi_0=0$).	36
Table 2.3. Comparison between measured and simulated phase variation ($\Delta\varphi$) of the rotation frequency harmonics in the near-field region for different values of φ_0 (with respect to $\varphi_0 = 0$). The given values in parenthesis are the magnitude of \mathbf{B} -fields at frequency harmonics.....	45
Table 3.1. Coupled Antennas Characteristics for Different Separation Distances.	63
Table 3.2. Simulated and Measured Impedance Bandwidth.....	70
Table 3.3. Simulated and Measured Peak-Gain Variations in Impedance Bandwidth.	71
Table 4.1. Structural Mechanics Properties of the Cells and Amyloid Fibrils.	78
Table 4.2. Summary of Proposed Models for EM Signaling among Biological Cells.....	103
Table 4.3. Summary of Proposed Multiphysics Models for Channel Capacity Estimations.....	114
Table 5.1. Comparative Study between Bandwidth and Input Impedance of Two Coupled Antennas.	119

List of Appendices

APPENDIX A: Mathematical Representation of Proposed Phase Modulation (PM) in Mechanical Antennas	124
APPENDIX B: Quality Factor Estimation for Vibration of Amyloid Fibrils in Water as Viscous Medium.....	127
APPENDIX C: Radiation Enhancement in Mechanical Antennas using Magneto-Dielectric Resonance Concept.....	129

Abstract

This thesis presents novel solutions to certain emerging problems related to electrically small radiating systems and antennas for effectively increasing the radiation efficiency and/or bandwidth of physically small antennas radiating at low frequencies. The thesis introduces the concept of fragmented antennas for the first time. It also provides a completely novel solution for implementation of mechanical antennas with frequency multiplication and phase modulation capabilities for the first time. These concepts are borrowed to develop mechano-electromagnetic radio concept for biological cells to explain how communication can occur in community of cells.

The proposed mechanical antenna provides unique capabilities for communication at very-low frequency band (3-30 kHz) and lowers. In mechanical antennas, the radiation is mainly induced through accelerating (rotating) electric charges or permanent magnets by means of fast electric motors. This work presents a novel phase modulation and frequency multiplication scheme for radiation at frequencies up to seven time rotation frequency of their mechanical motor and at the same time provides phase modulation capability. This is done by incorporating two pairs of orthogonal bow-tie shape high- μ magnetic material plates through which super magnetic bar is rotated by a fast electric motor. By moving the angular position of the magnetic plates, it is shown that the phase and amplitude of the EM signal can be modulated. This thesis also reports on the feasibility of formation of an electrically large antenna at low frequencies using a number of miniaturized antennas through electromagnetic coupling for achieving high bandwidth. The proposed fragmented antenna system is intended for a linear flight formation of small UAVs

carrying individual antennas. Inductively end-loaded folded dipole antennas are used as the individual antenna that can provide radiation at the desired frequency over a narrow bandwidth. The overall dimensions and the total mass of the individual elements are $12 \times 10 \times 10 \text{ cm}$ ($0.096\lambda_0 \times 0.08\lambda_0 \times 0.08\lambda_0$ at 240MHz) and 18g (including the matching network), respectively. Each miniaturized antenna can only provide 2.4 MHz ($\sim 1\%$) bandwidth and 25Ω input impedance. It is shown that a cluster of three of such elements operating in the vicinity of each other, the center element can provide 18.4 MHz bandwidth (an improvement of 770%) through inductive coupling while the other two elements are loaded with optimal reactive elements.

The fundamentals of operation of embedded radios within cellular structures and biofilms is based on mechanical antennas. Certain bacterial cells within their biofilms are equipped with elastic helical fibers called amyloid fibrils which pose permanent electric dipole. We propose that the cells transmit electromagnetic (EM) signal to their surrounding environment through mechanical vibration of these fibrils. Different vibrational modes associated with fibrils including cantilever beam mode, longitudinal spring vibrational mode, and transverse spring modes are investigated indicating potential EM signaling within kHz-MHz, GHz, and sub-THz ranges, respectively. A novel and theoretical Multiphysics model based on coupled system of electrical and mechanical structures is also proposed to study the impact of this signaling on crowd of fibrils in a biofilm sample. Next, to demonstrate the advantage of EM-based communication, using communication channel theory, we have compared performance of EM signaling with its biochemical counterpart (quorum sensing) and shown that EM signaling provides much higher data rate, 5 to 7 orders of magnitude, and over much longer ranges. Thus, it could be potentially more efficient and a preferred method for communication among cells. In quorum sensing,

biological cells release auto-inducers intercepted by the adjacent cells as a purposeful message signal.

CHAPTER 1

Introduction

Electromagnetic (EM) radiation basically happens when electric or magnetic charges get accelerated [1]. For instance, if a wire conductor is fed by time-varying current, it radiates EM waves. For the purpose of efficient radiation, the size of these antenna must be proportional to $\frac{\lambda}{2}$ [1] where λ is the wavelength of the radiation. For low-frequency communication links (kHz to MHz) in electromagnetic-cluttered environment including urban and indoor settings, underwater as well as underground, the wavelength size becomes long which mandates design of electrically-small antennas if there is a constraint on the volume and size. Electrically-small antennas by definition are the antennas that their physical length is considerably smaller than the wavelength. This could be for example a nano-scale antenna that is operating at GHz frequencies, or a *cm*-size antenna radiating at kHz frequencies. The drawbacks of electrically-small antennas are their narrow bandwidth and poor radiation efficiency according to the well-known Chu-Harrington limit [1]. In order to overcome these drawbacks, new ways of EM signal generation and antenna design must be considered and introduced specifically for low-frequency communication applications. As a new paradigm, in this dissertation, we have first revisited acceleration of charges enabling efficient radiation at very-low frequencies. This scheme is called mechanical antennas. Then, it has been addressed how one can create an electrically-large antenna from small coupled radiators. These developed electrically-small antenna design concepts are then borrowed to unravel the

concept of electromagnetic-based communication which has been recently hypothesized to be existing among biological cells [2], [3].

It is known that many biological functions are mediated by electrical signals. There is also a growing amount of knowledge indicating that biological cells and bacteria communicate through electromagnetic (EM) waves. The frequency spectrum associated with this signaling is not yet known well and must be explored. Questions of importance as regard to the nature of such EM signaling among biological cells are as follows: 1) what mechanisms are available to individual cells to enable them for EM signal transmission and reception?, 2) how to predict the frequency and waveform of signal generated by cells?, and 3) if there is going to be radiation at low-frequencies ($< GHz$), how such nano-scale structures can radiate efficiently?. In other words, as electromagnetic engineers, we require to identify the nature electrically-small antennas among these cellular structures especially if communication frequency is in the GHz range or below. Here, It has been shown that the fundamentals of operation of embedded radios within cellular structures is based on mechanical antennas.

1.1. Recent Advances on Efficient, Low-Frequency, and Small Antennas Design

1.1.1. Mechanical Antennas

Underwater wireless communication (UWC) and underground wireless sensor networks are of great interest for many applications including remote control in the off-shore oil industry, pollution monitoring, and security [4]. Establishing reliable underwater and underground communication is a really challenging task mainly due to the large conductivity of seawater ($\sigma = 4 \text{ S/m}$) and wet soil (up to $\sigma = 1 \text{ S/m}$) [5]. This conductivity would cause drastic attenuation for the wave propagating inside the seawater and soil. To illustrate this fact, the attenuation constant

(α) for propagating waves in seawater is plotted in Figure 1.1 as a function of frequency (1 Hz-100 MHz) using,

$$\alpha = \Re\{\sqrt{j\omega\mu(j\omega\varepsilon + \sigma)}\} \quad (1.1)$$

where μ and ε are the permeability and permittivity associated with water. The seawater can be considered as a non-magnetic material ($\mu_r = 1$) with relative permittivity $\varepsilon_r = 81$. As can be concluded from this figure, the lower the frequency of propagation is, the lower attenuation the wave will experience. In fact, lower attenuation provides more signal coverage. This phenomena is also demonstrated here by investigating the wave propagation at water/air boundaries. Figure 1.2(a) shows 2-D view for a scenario at which a time-harmonic short magnetic dipole ($I_m dl$) is placed at height z' above the seawater surface. In practice, a time harmonic magnetic dipole can be realized by rotating either a permanent magnet or a short loop carrying DC current. For simplicity, a flat interface (boundary) is assumed between the air and water. The transmitted magnetic field into the seawater can be analytically derived as [6],

$$B_\rho^t = \frac{I_m dl}{4\pi\omega} \int_0^\infty (jk_{1z}) dk_\rho \frac{k_\rho^2}{k_z} J_1(k_\rho \rho) e^{jk_{1z}z} e^{-jk_z z'} T_{TE} \quad (1.2)$$

$$B_z^t = \frac{-I_m dl}{4\pi\omega} \int_0^\infty dk_\rho \frac{k_\rho^3}{k_z} J_0(k_\rho \rho) e^{jk_{1z}z} e^{-jk_z z'} T_{TE} \quad (1.3)$$

$$T_{TE} = \frac{2k_z}{k_z + k_{1z}} \quad (1.4)$$

$$k_{1z} = \sqrt{k_1^2 - k_\rho^2}, \quad k_z = \sqrt{k_0^2 - k_\rho^2} \quad (1.5)$$

Where k_ρ is the tangential component of wave vector which is continuous across the boundary and k_{1z} and k_z are the normal components of the wave vector inside the water and air, respectively.

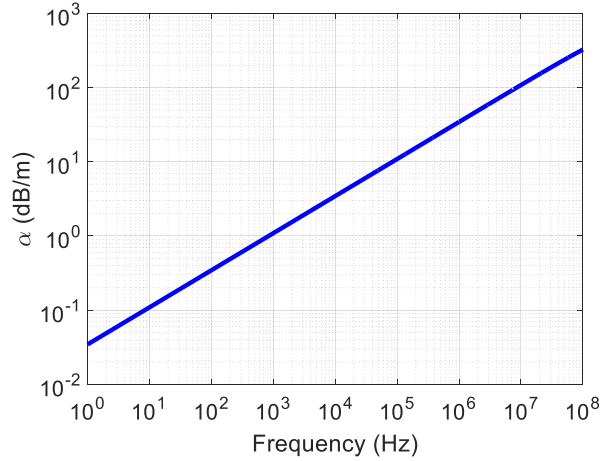


Figure 1.1. Attenuation constant as a function of frequency associated with EM waves propagating in the seawater ($\sigma = 4$ S/m).

Based on the defined coordinate system, the electric field of the magnetic dipole is expected to have only $\hat{\phi}$ component. This is why the transmission coefficient used here is the one associated with a TE wave. It is assumed that the magnetic dipole is placed at $z'=150$ m above the seawater and $I_m dl = 1$. Figure 1.2(b) and Figure 1.2(c) depict the profile of total transmitted magnetic field into the seawater for $f = 10$ kHz and $f = 200$ Hz, respectively. All the field profiles are normalized to the amplitude of the magnetic field at the surface of water. As expected, the lower the frequency of transmitted signal is, the more signal coverage it can provide.

Currently, there are numerous underwater and underground communication systems operating at the microwave frequencies [7], [8]. However, they are typically limited to shallow depths while providing large data rate. Based on the abovementioned calculations, among the radio frequency (RF) communication bands, Ultra-Low Frequency (ULF, 0.3 kHz-3 kHz) and Very-Low Frequency (VLF, 3 kHz-30 kHz) bands are becoming potential candidates for deep underwater and underground communication applications due to the wide field of coverage provided by the EM waves at such frequencies [9], [10]. It should be noted that there are also other alternatives to underwater communication, namely acoustic communication and optical

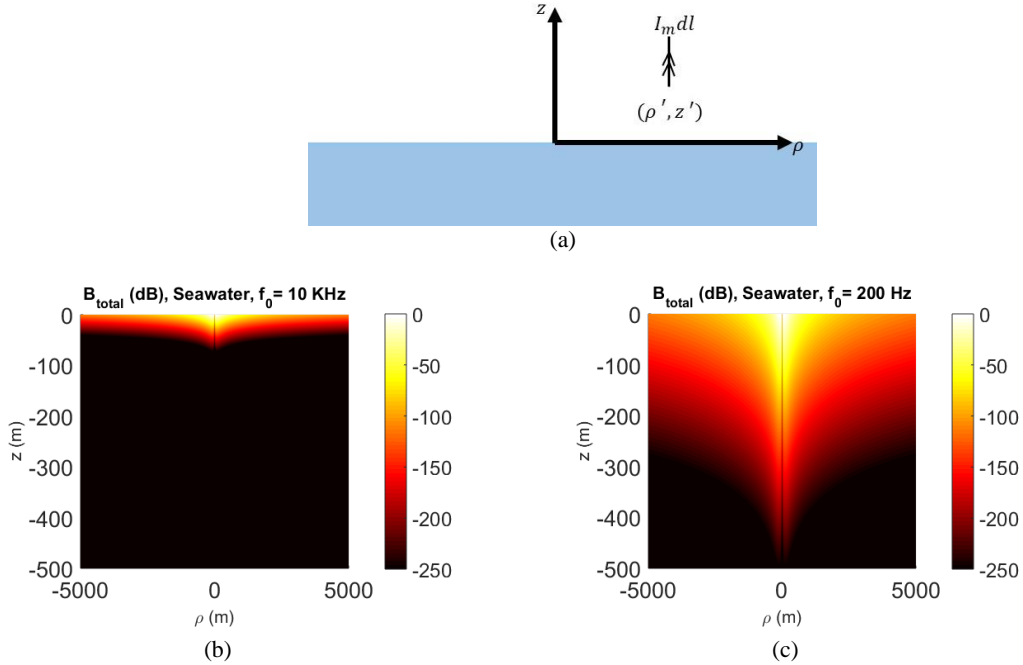


Figure 1.2. (a) 2-D view of signal transmission into seawater using a magnetic short dipole above the surface of water. The transmitted magnetic field into the water by a magnetic dipole moment at (b) 10 kHz and (c) 200 Hz. All the field profiles are normalized to the corresponding maximum field at the boundary.

communication [11], [12], but these are not as appropriate as electromagnetic-based communication. Optical communication is more affected by the turbidity of the water, and it is usually more appropriate for short distance communication requiring line of sight. Acoustic waves also require both the transmitter and receiver to be underwater, and the performance is degraded by interference from other acoustic sources [13].

The drawbacks of ULF/VLF communication are twofold: 1) the size of the transmitter antenna, and 2) the low available bandwidth. To radiate electromagnetic wave effectively, the size of the antenna must be comparable to half a wavelength or larger. Figure 1.3 represents one of the U.S. Navy's VLF antenna at Cutler, Maine. The antenna occupies 2,000 acres on a peninsula with 850 to 1000 ft. height. It has radiation efficiency up to 75% and only 140 Hz bandwidth which is extremely narrow [9]. Considering the wavelength at for example 10 kHz (~ 30 km), it is obvious that fabrication of a portable, reasonably small, and efficient VLF antenna using even

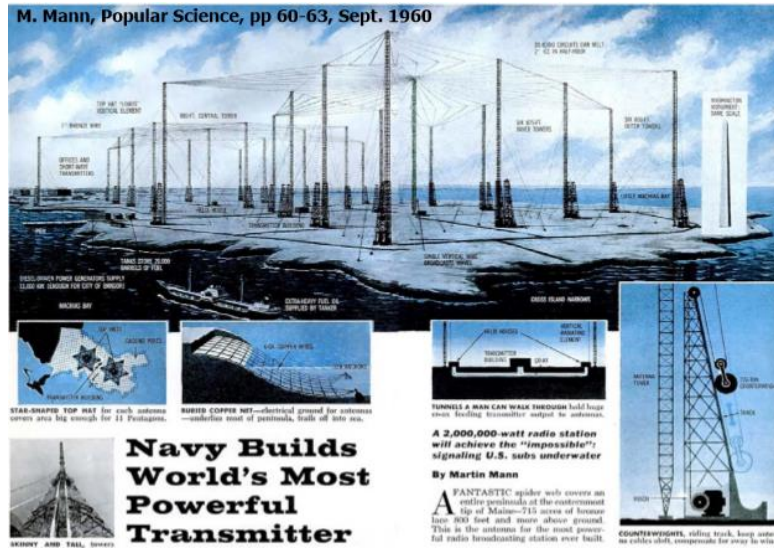


Figure 1.3. U.S. Navy’s VLF antennas at Cutler, Maine. Current VLF transmitters have length scales of many kilometers.

miniaturization techniques [14], [15], is not feasible. Hence, other alternatives must be considered to realize hand-held transceivers at such low frequencies. In the past few years, the concept of mechanical antennas has been introduced and investigated for this purpose [16], [17]. In mechanical antennas, instead of using signal generators to drive the antenna for radiation, the radiation is induced by mechanically-accelerating (rotating) electric charges or permanent magnets. It has been analytically shown that the radiation efficiency of mechanical antennas can be many orders of magnitude higher than conventional electrically small antennas [17].

As part of my contributions in this dissertation, I have addressed the challenges of mechanical antennas namely signal modulation, and mechanical system stability and proposed a unique solution that can alleviate these problems significantly.

1.1.2. Fragmented Antennas

The ever-increasing demands for microwave frequencies (300 MHz-300 GHz) compared to the VHF band (30-300 MHz) and lowers in modern wireless communication is mainly attributed

to more available bandwidth (higher data rate), compatibility with the size of consumer electronic devices, and also higher resolution for imaging and radar applications [18]-[20]. Despite these advantages, experimental studies indicate that the communication channel complexity at the VHF band and lowers is far less since significant signal penetration through obstacles and manmade objects is possible [21]. It has been shown that reflection, scattering, and multi-path at such low frequencies are far lower than what is observed at the UHF band (300 MHz-3 GHz) and higher [22]. Figure 1.4 provides a comparison between coverage map of a point-to-point wireless communication operating at 40 MHz (low-VHF) and at 2.4 GHz (ZigBee radio) [23]. In this scenario, the transmitting node is placed inside a multi-floor building with numerous rooms (walls) while the receiver is outside and surrounded by dense vegetation and other buildings. As can be observed, the low-VHF link can simply provide 5 times longer signal coverage. Then, such significant signal penetration through the soil and building materials allowing for direct communication makes the lower frequencies more favorable for communication in urban, indoor, and subsurface environment.

Antennas are among the most important components of a wireless network, and as far as efficiency and size are concerned, they may impose stringent restrictions on the size and performance of any wireless system. At low frequencies, the size of the conventional antennas is very large, making the application of communication systems at low-VHF and HF bands limited to stationary nodes. On the other hand, for mobile nodes, extremely small antennas must be designed. Major drawbacks of very small antennas are their extremely narrow bandwidth ($\sim 0.1\%$) and low radiation efficiency ($\sim 5\%$) [24]. This would limit the data rate significantly considering the fact that the operating frequency is by itself rather low ($BW \sim 10\text{-}20\text{ kHz}$). Also, the transmitter power needs to be high to compensate for the poor radiation efficiency. It is highly desirable to

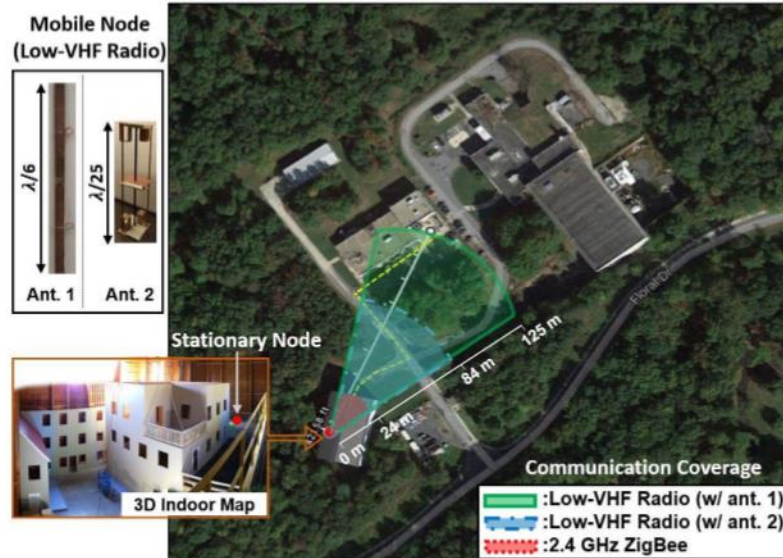


Figure 1.4. Coverage maps of point-to-point wireless communication at low-VHF (40 MHz) and at 2.4 GHz (enabled by a ZigBee radio) in non-line-of-sight multi-floor indoor to outdoor scenario.

enable low-VHF and HF communication for small mobile platforms such as unmanned aerial vehicles while achieving high radiation efficiency and bandwidth [25]. Unmanned aerial vehicles (UAVs) are nowadays becoming an integral part of autonomous systems and they can be used for advanced imaging technologies, tactical communication, as well as cargo and medicine transportation [26], [27]. For some of these applications such as tactical communication, the UAV must be able to communicate in an electromagnetically-cluttered indoor environment and thus equipped with an efficient low frequency communication system. Thus, a new approach must be considered to design small antennas for such platforms which can operate at VHF band and if needed can provide wider bandwidth with acceptable high radiation efficiency values. This task might be accomplished through constructing a larger antenna using small segments of the antenna on many adjacent but disconnected platforms. In recent years, much effort has been devoted into control and autonomous operation of small UAVs [28], [29]. These flyers can perform complex and tight flight formation not possible before (see Figure 1.5). Such advances may be utilized to construct a bigger radiator from individual small elements aboard small UAVs. Near-field electric



Figure 1.5. Swarming drones in different configurations [30]. Recent advances on autonomous control has enabled arbitrary flight formations for UAVs.



Figure 1.6. Concept of fragmented antenna formed by many electromagnetically-coupled small antennas on a cluster of UAVs.

and magnetic coupling can be efficiently used for formation of a larger antenna from disparate small elements. Through such couplings, it is expected to enhance the bandwidth and radiation efficiency while being able to have small antennas operating at low-VHF and HF bands and are compatible with the size of small platforms [31], [32]. To better visualize the concept, Figure 1.6 depicts our proposed concept for a special case where a cluster of small UAVs in a linear flight formation construct a fragmented low frequency antenna through some appropriate electromagnetic coupling of many electrically small radiators. Chapter 3 of this dissertation is devoted into this topic.

1.2. Background and Motivation for Electromagnetic Signaling among Biological Cells

Cell biology is a branch of biology which focuses on unraveling the structure and function of cells such as bacteria, archaea, microbe, and fungi, to just name a few. By understanding how

cells would work in healthy and diseased conditions, cell biologists working in animal, plant and medical science will be able to develop new vaccines, more effective medicines, and plants with improved qualities. Thus, this realm of science is crucial as it can potentially save many lives every day. According to CDC reports, it is estimated that antibiotic resistance was responsible for 25,000 deaths in a year in the European Union alone, with similar statistics present in countries around the world [33]. The World Health Organization considers antibiotic resistance to be one of the biggest threats to global health, and food security and emphasizes that infections such as pneumonia, tuberculosis, gonorrhoea, and salmonellosis are becoming more challenging to treat as they evolve to resist treatments [34].

One of the sub-topics in cell biology is cell communication aimed to identify different types of communication methods between living cells. It is a well-known fact that biological cells, whether belonging to unicellular or multicellular organisms, do not function in isolation. Their proper function or even survival depends on their ability to interact with each other and the outside environment [35]. Critical environmental information that cells need to sense and process includes population, temperature, pH, availability of nutrients, etc. [36]. Cells can make adjustments to their internal workings in response to information received from adjacent cells. Cell signaling in unicellular organisms is used for coordinating tasks, and in multicellular organisms allows for formation of tissues such as muscles and nerves [37]. The commonly accepted communication mechanism between biological cells, known as quorum sensing, is a process of communication by which cells release chemical molecules (auto-inducers) to adjacent cells through the process of diffusion [38]. For instance, gram-positive bacteria, such as *Staphylococcus aureus*, utilize Oligopeptides as chemical messengers [39]. Signaling molecules are continually secreted by bacteria to announce their presence to their neighbors. Auto-inducers let bacteria sense population

density and change their behavior in a synchronized fashion when the density reaches a certain threshold. Bacterial populations will activate some genes only when they are able to sense that their population is numerous enough [40]. This communication scheme however is quite a bit slow as it relies on the diffusion of molecules in water. Additionally, estimations indicate that individual cells requires large amount of energy (\sim mJ/mL) to produce the auto-inducers for quorum sensing [41]. Alternatively, many functions among biological cells (neurons, muscle cells, and specific plant cells) are mediated by the electricity [42], [43]. For instance, neurons generate electric signals by the means of an action potential. Initiated by voltage-gated ion channels embedded in a cell's plasma membrane, an action potential occurs when the membrane potential rapidly rises and falls [44]. This depolarization waveform propagates through axons then to transmit. There is also a growing body of knowledge that in addition to the chemical signaling using auto-inducers, biological cells also transmit/receive electromagnetic waves. Electromagnetic signaling can take place at the speed of light and is expected to be relatively faster. Latest studies show some bacterial DNA sequences induce electromagnetic waves (\sim kHz) at high aqueous dilutions [45], [46]. Microtubules as ubiquitous organelles in the cytoskeleton of eukaryotic cells are also conjectured to emit time-varying electric fields (\sim GHz) through mechanical vibration of their tubulin monomers having permanent electric dipoles [47], [48]. However, no experimental evidence has confirmed these high frequency oscillations to date. Similarly, protein chains have demonstrated high frequency oscillations (\sim THz) which can be the source of an endogenous electric field [49], [50].

Inspired by the abovementioned observations, recently there exists significant interests toward investigating a possibility at which biofilms can also transmit/receive EM waves as a means of communication within their communities [2], [3], [51]. Biofilms are a collection of one or

multiple types of microorganisms including bacteria, microbes, and fungi [52]. They can form and grow in different environment on the earth. The human body hosts biofilms in the mouth and intestinal track that can protect our health or harm it [53]. Bacterial biofilms are responsible for a vast majority of clinical infections [54]. Biofilms also pose a serious threat to public health due to their resistance against antibiotics compared to individual bacteria [55]. Hence, understanding the characteristics of biofilms under diverse conditions is of great importance. Profound investigation is initially required to unravel how community of biological cells in a biofilm communicate to for example coordinate metabolic states among themselves to evolve and grow over time. Then, biologists can further evaluate how to facilitate or hamper such communication so as to efficiently control their related physiological activities.

Figure 1.7 depicts the scanning electron microscope (SEM) image of two different biofilm samples associated with *Staphylococcus aureus* and *Pseudomonas aeruginosa* bacteria [56]. Cells in a biofilm live in a self-produced matrix of hydrated extracellular polymeric substances (EPS) which constitute their immediate environment [57]. The major matrix components are polysaccharides, lipids, proteins and DNA distributed between the cells in a non-homogeneous pattern. EPS matrix provides mechanical stability for biofilms, mediate their adhesion to surfaces and interconnects biofilm cells through formation of a three-dimensional polymer network.

To date, there is no compelling experimental evidence regarding the hypothesis for electromagnetic emission from biofilms. The main objective of this dissertation is to explore all possible mechanisms of EM signaling among the cells in a biofilm (here, specifically focused on *Staphylococcus aureus*, and *Bacillus subtilis*) for the first time and clarify what the built-in antennas actually are. It is known that the primary building block for any electromagnetic-based communication is antennas. Therefore, we require to first identify the nature of these antennas and

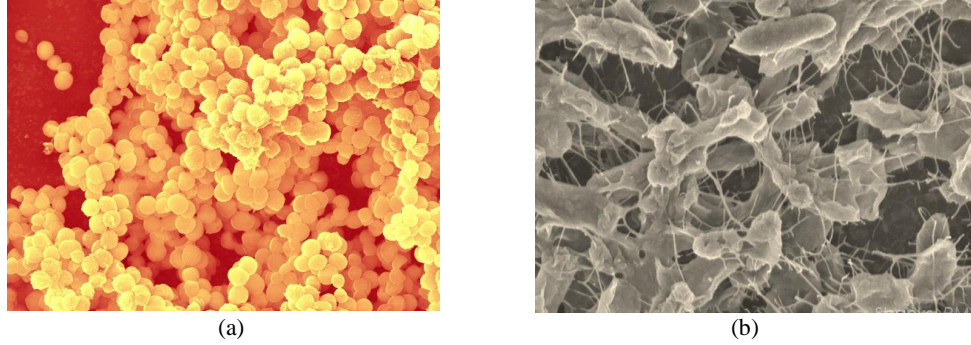


Figure 1.7: SEM image of bacterial biofilms. (a) *Staphylococcus aureus* biofilm. (b) *Pseudomonas aeruginosa* biofilm. The bacterial cells in a biofilm are supported by the EPS matrix.

then develop models that can conceptually explain such communication phenomena. Next, as a theoretical indication, we also need to develop comparisons between the EM signaling and quorum sensing performance to unravel why EM signaling would be potentially required and can be a preferred method for communication among cells. In order to accomplish these tasks, we have borrowed our newly developed antenna design concepts for low-frequency applications namely, fragmented antennas and mechanical antennas.

1.3. Dissertation Overview and Contributions

Figure 1.8 shows an overview of the topics that are covered in this dissertation. The ultimate goal of this work is to propose a novel Multiphysics model which can conceptually unravel the electromagnetic-based communication phenomena among biological cells and also develop theoretical indications to clarify the advantage of EM signaling compared to the biochemical communication (quorum sensing). These objectives are achieved using two newly developed concepts in antenna design namely fragmented antenna and mechanical antenna and expanded in six chapters.

In Chapter 2, the concept of mechanical antennas is investigated analytically and numerically using ANSYS Maxwell first, and then, a novel phase modulation scheme is introduced

for rotating permanent magnets. Phase modulation compared to the amplitude modulation is proven to be less sensitive to the additive noise [58]. The proposed approach is based on rotating a permanent magnet (by means of a high speed electric motor) sandwiched between two pairs of orthogonal bow-tie shape plates made of a high- μ magnetic material. Changing the position of the magnetic plates with respect to the magnet is shown to modulate both phase and amplitude of the EM signal. The amplitude modulation is also significant and this provides an additional important feature, which allows the mechanical antenna to generate higher signal harmonics of the rotation frequency and thereby it facilitates radiation at a much higher frequency than the rotational frequency of the motor. Hence, higher range and more radiated power can be achieved.

In Chapter 3, the concept of near-field electromagnetic coupling (electric coupling + magnetic coupling) is applied to a cluster of three detached inductively end-loaded folded dipole antennas mounted on three separate mobile platforms in order to effectively realize a larger antenna and thus, provide wider bandwidth than that of a single element [32]. The overall antenna configuration is called fragmented antenna. It is shown that the input impedance of the coupled antenna array is highly sensitive to their separation distance with each other requiring a tunable matching circuit. A tunable matching circuit is also proposed to overcome the problems associated with the flight formation fluctuations of the mobile platforms. Measurement results indicate that having proper electromagnetic coupling between these three fabricated elements, the middle element can provide 7.7 fold improvement in bandwidth compared to the single element in isolation when the other two adjacent elements are loaded with optimal reactive loads (here, a capacitor). Moreover, the proposed configuration shows 1 dB gain improvement at boresight direction and higher efficiency.

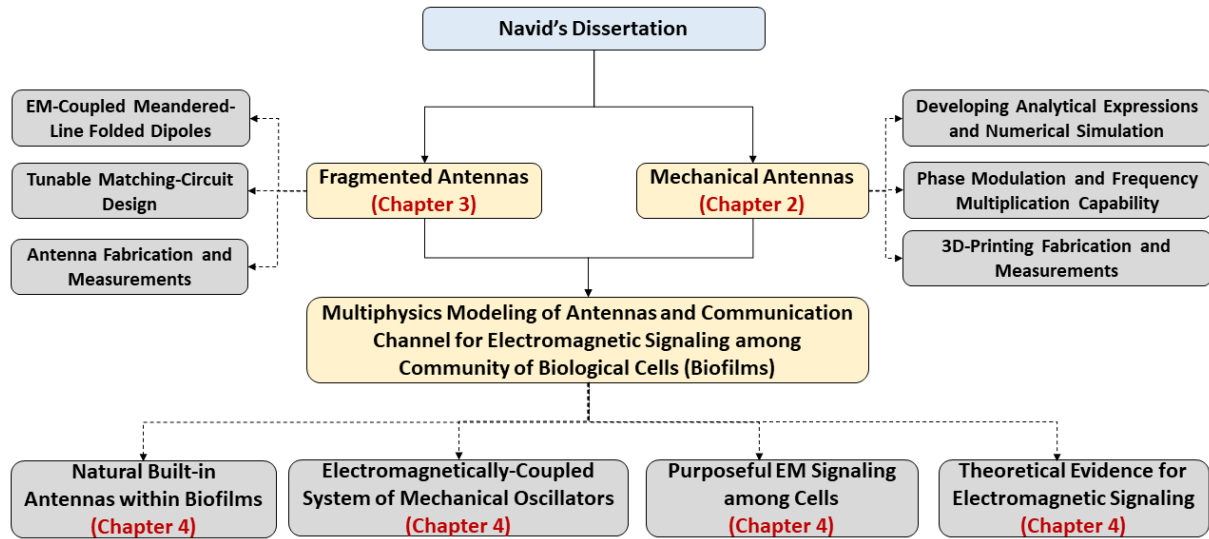


Figure 1.8. Overview of the topics that are covered in this dissertation.

In Chapter 4, a novel Multiphysics model is presented that describes a possible mechanism for electromagnetic (EM) signal transmission and reception by individual cells within their communities called biofilms. Certain biological cells such as *Staphylococcus aureus* bacteria, within their biofilms are equipped with charged helical fibrils (amyloid fibrils) for which we postulate that mechanical vibration of these fibrils allows the cells to transmit EM signal to their neighboring cells and the surrounding environment (concept of mechanical antenna). The reverse mechanism, acting as a matched filter, is also used by other cells to receive the transmitted signal. Thus, charged amyloid fibrils would play the role of antennas for their corresponding cells within biofilms.

As there is no compelling experimental evidence to date, to demonstrate the advantage of EM signaling, using communication channel modeling, comparison with commonly believed biochemical communication method known as quorum sensing is presented and shown that EM-based communication provides much higher data rate and over longer distances [59]. For electromagnetic (EM) signaling, the Shannon channel capacity theorem is applied to find the

corresponding data rate. To examine the quorum sensing performance, a Multiphysics-based binary channel model combining information theory and 3D molecular diffusion is developed. As another indication, it has been demonstrated that the energy required for EM signaling is far less than that for quorum sensing as the cells do not produce messaging chemicals.

Finally, Chapter 5 is dedicated to the concluding remarks and future directions for the topics covered in this thesis.

CHAPTER 2

Mechanical Antennas

2.1. Introduction

Very-low frequency electromagnetic (EM) signals have been the focus of interest for over the horizon communication and communication between nodes on the earth's surface and deep submarines and underground mines [60]-[62]. The long signal wavelength (kilometers to hundreds of kilometers) is the key factor for the significant signal penetration into the seawater ($\sigma = 4 \text{ S/m}$) and wet soil compared to higher frequencies [63]. Ultra-low frequency (ULF) and very-low frequency (VLF) bands corresponding to 0.3-3 kHz and 3-30 kHz, respectively, are also potential candidates for long-range, over-the-horizon, and transcontinental communication mainly due to the strong reflection of the signal caused by the ionosphere [64]. Basically, the signal reflection between the ground and the ionosphere supports waveguide modes at such low frequencies. ULF/VLF signals are also considered appropriate for monitoring fractures in ships and oil containers as they can easily propagate through any metallic enclosures [65]-[67].

Application of such low frequency communication links is usually hampered by the requirement in using giant-size transmitting and receiving antennas and the very small available bandwidth such systems can provide. Considering the extremely long wavelength at 1 kHz (300 km), design and fabrication of a reasonably small, portable, and efficient ULF/VLF antenna using the conventional miniaturization techniques [14], [15], [68], [69] is not possible. Hence, alternatives must be considered to realize hand-held transceivers at such low frequencies. In the

past few years, the concept of mechanical antennas has been introduced and investigated extensively for this purpose. It is well-known that mechanical acceleration of charged particles induces electromagnetic radiation at the fundamental frequency of motion [6]. The frequency of intended radiation (0.3-30 kHz) is low enough to imagine the possibility of inducing it by mechanical rotation of charged particles or electrets or permanent magnets. It is shown that the radiation efficiency of mechanical antennas can be many orders of magnitude higher than conventional electrically small antennas [17]. In [16], an ultra-low loss lithium niobate piezoelectric electric dipole driven at its acoustic resonance radiates EM waves at around 35 kHz. The same approach based on acoustically actuated ultra-compact NEMS is applied to induce EM radiation at around 60 MHz [70]. The above mentioned mechanical radiators are basically electric-based radiators which may not be potential candidates for communication in highly conductive media such as wet soil and seawater. For reliable communication in such electrically conductive environment, it is proposed that magnetic-based radiators could outperform their electric counterparts [71]-[72].

Another issue with the communication at ULF/VLF bands is the small available bandwidth. One can take the advantage of different signal modulation schemes to overcome such drawback [73], [74]. A Challenging aspect, however, is how to modulate the mechanical antenna's signal with the intended information. The common modulation techniques for mechanical antennas would be the frequency modulation (FM), amplitude modulation (AM) and phase modulation (PM). In frequency modulation, it is required to change the rotation frequency of magnets mechanically and instantaneously [75]. However, this approach is constrained by the moment of inertia of magnet (bulky) and is considered inefficient. The large mass density of magnets typically would not allow to change the rotation frequency instantaneously and hence the bandwidth is

small. A new amplitude modulation scheme has been recently proposed in [76] through surrounding a spinning spherical magnet with a magnetic shielding wrapped with an AC current-carrying coil. This modulation technique is shown to provide improved bandwidth compared to the frequency modulation. However, communication based on amplitude modulation, especially with small modulation depth ($\sim 30\%$), is prone to performance degradation with distances due to the additive manmade and thermal noise. To offer better performance in terms of noise, in this chapter, a novel phase modulation scheme is introduced for rotating permanent magnets. Phase modulation compared to the amplitude modulation is proven to be less sensitive to the additive noise [74]. The proposed approach is based on rotating a permanent magnet (by means of a high speed electric motor) sandwiched between two pairs of orthogonal bow-tie shape plates made of a high- μ magnetic material. The application of a moving magnetic material in close proximity of a stationary permanent for designing a mechanical antenna was recently presented in [77] and was also exploited over 100 years ago as an early AC signal generator [78]. In [77], through rotating a plate made of magnetically-soft material with multiple openings, the field of a static permanent magnet is amplitude-modulated to generate EM signals around 1 kHz. In this contribution, however, it is shown that changing the position of static bow-tie shape magnetic plates (displacing them) with respect to a mechanically rotating magnet can modulate not only the amplitude but also the phase of the EM signal emitted from the magnet. The achieved phase modulation can provide higher modulation bandwidth and make the communication link immune to additive noise. Also, as is mentioned in [77], the high index amplitude modulation allows the mechanical antenna to generate higher harmonics of the rotation frequency and thereby it facilitates radiation at a much higher frequency than the rotational frequency of the motor. This feature can overcome the instabilities and bearing friction of a rotating system at very high speeds needed for radiation at

VLF band. Additionally, it is analytically shown that, higher range and more radiated power can be achieved compared to a rotating magnet without magnetic plates. Numerical simulations are first performed to optimize the geometry and dimensions of the bow-tie shape ferrite plates. Then, near-field numerical simulations and far-field analytical analysis are provided to demonstrate the capabilities and unique features of the proposed mechanical antenna. As the majority of numerical simulation software cannot perform far-field analysis at very low frequencies (huge computational resources required), a new analytical approach based on the equivalence principle and reciprocity theorem is proposed and developed for this purpose.

2.2. Field Equations and Numerical Simulations for Rotating Magnets

It is known that sinusoidal mechanical motion of charged particles (electric or magnetic) induces EM radiation at the fundamental frequency [79]. The frequency of desired radiation (0.3-30 kHz) seems to be low enough to imagine the possibility of inducing it by mechanical rotation of electrets or permanent magnets specifically for the ULF band (0.3-3 kHz) and lowers. In this section, the fields generated by a single rotating magnet in the near-field and the radiation zone are derived. The same results could be readily obtained for electrets using the duality relations.

2.2.1. Far-Field Analysis

Figure 2.1(a) shows a cylindrical magnet (length l) rotating with angular frequency ω around the z -axis (passing through its center of mass) in the $x - y$ plane. Such rotating magnet can be fundamentally modeled as a rotating magnetic dipole with equivalent magnetic dipole moment $p_m = 2Q_m r_0$ (see Figure 2.1(b) and Figure 2.1(c)). Here, Q_m and $2r_0$ are the equivalent magnetic charge and dipole arm length associated with the permanent magnet. As depicted in

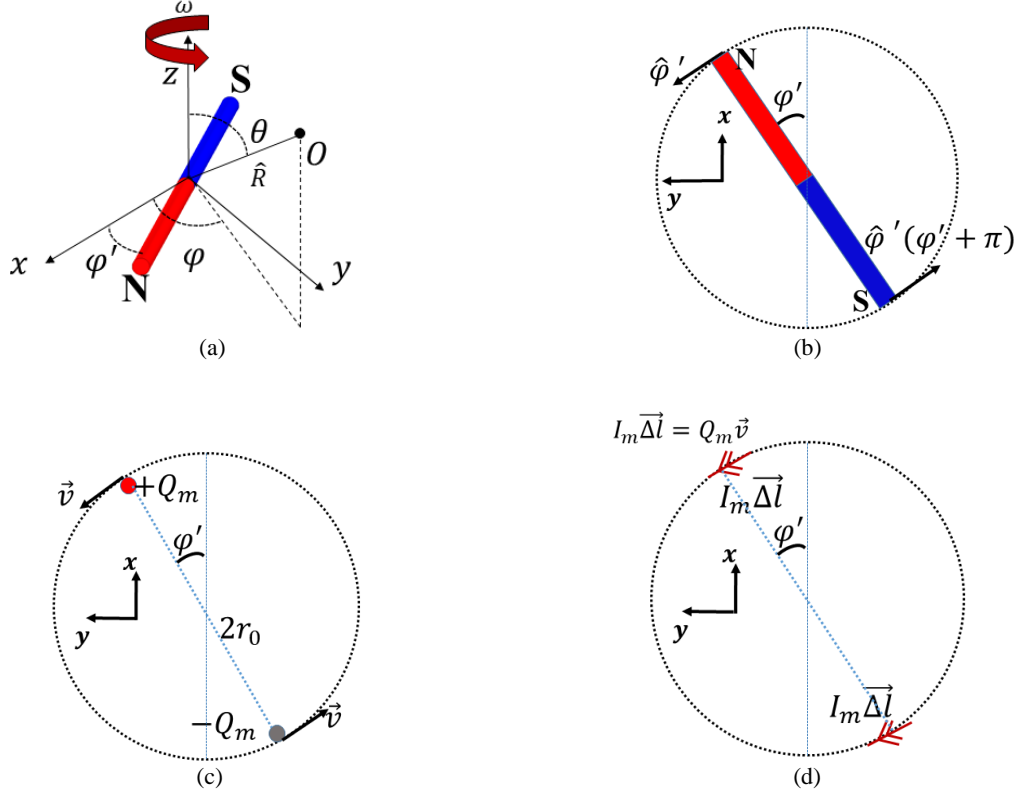


Figure 2.1. (a): Rotating cylindrical permanent magnet (around z-axis) represents a mechanical antenna. θ and φ are representation of the observation point in spherical coordinate system. (b) 2D top view of the rotating magnet. (c): Equivalent magnetic dipole representation of the rotating magnet. (d): Equivalent magnetic current model associated with the rotating magnet.

Figure 2.1(d), a rotating magnetic charge can be considered as a magnetic current filament ($I_m \vec{\Delta \ell}$) whose direction of flow is parallel to the charge velocity (\vec{v}) as [10],

$$I_m \vec{\Delta \ell} = Q_m \vec{v} \quad (2.1)$$

Defining the primed coordinate system for moving magnet, at an angular location $\varphi' = \omega t$, the filament current is in the direction $\hat{\varphi}'$, and therefore,

$$I_m \vec{\Delta \ell} = I_m \Delta \ell \hat{\varphi}'(\omega t) = I_0 \Delta \ell [-\sin(\omega t) \hat{x} + \cos(\omega t) \hat{y}] \quad (2.2)$$

Also, as shown in Figure 2.1(c), the negative magnetic charge is moving in the $\hat{\varphi}'(\varphi' + \pi)$ direction, and therefore the current associated with the negative magnetic charge is the same as what given in Eq. (2.2). For the far-field approximations, one can assume these currents are co-

centered at the origin. In fact, the small phase delay associated with the location of the two currents could be ignored in the far-field region. Defining the propagation constant $k = \frac{\omega}{c}$ and applying Eq. (2.1) with $v = r_0\omega$, the expressions for the radiated electric and magnetic fields in the far-field region are expressed as,

$$\vec{E} = \frac{Q_m r_0 \omega k}{2\pi R} \{ \cos(\omega t - kR) \hat{x} + \sin(\omega t - kR) \hat{y} \} \times \hat{R} \quad (2.3)$$

$$\vec{H} = -\frac{Q_m r_0 \omega^2 \epsilon_0}{2\pi R} \{ \cos(\omega t - kR) \hat{x} + \sin(\omega t - kR) \hat{y} \} \times \hat{R} \times \hat{R} \quad (2.4)$$

where $\hat{R} = \sin \theta \cos \phi \hat{x} + \sin \theta \sin \phi \hat{y} + \cos \theta \hat{z}$ denotes a unit vector from the origin of coordinate system in the direction of observation point (O). The above expressions indicate that in the free-space, the rotating magnet radiates circularly polarized wave along the z -axis. The total radiated power can be also computed through integrating the Poynting vector over the surface of an enclosing sphere. The time-average radiated power is,

$$P_{rad} = \frac{2Q_m^2 r_0^2 \omega^4}{3\pi\eta c^2} = \frac{\epsilon_0 p_m^2 \omega^4}{6\pi c} \quad (2.5)$$

For a rotating magnet with remnant magnetic flux B_r , and volume V , the magnetic dipole moment can be expressed as,

$$p_m = 2Q_m r_0 \triangleq B_r V \quad (2.6)$$

Explicitly, the radiated power from the rotating magnet is,

$$P_{rad} = \frac{\epsilon_0 (B_r V)^2 \omega^4}{6\pi c} \quad (2.7)$$

It should be noted here that the total radiated power is proportional to the fourth order power of rotation frequency (ω) and therefore the higher the frequency of rotation is, the much higher the radiated power is.

2.2.2. Near-Field Numerical Simulations

Considering the long wavelength size at the ULF/VLF bands (\sim kilometers), for most practical applications, we deal with the near-field components of electromagnetic waves. Therefore, EM analysis of the antenna near-field is needed as well. The analytical expression for near-field magnetic field components of a low-frequency rotating permanent magnet can be calculated from its quasi-static approximation as [79],

$$\vec{B} = \frac{B_r V}{4\pi r^3} [3(\hat{R} \cdot \hat{m})\hat{R} - \hat{m}] \quad (2.8)$$

Based on the geometry of rotating permanent magnet shown in Figure 2.1(a), $\hat{m} = \cos(\omega t + \varphi_i)\hat{x} + \sin(\omega t + \varphi_i)\hat{y}$ defines the magnetization vector and \hat{R} denotes the observation point vector. Here, φ_i takes into account the initial magnetization vector of magnet. To validate the concept of mechanical antenna and this approximation at the same time, a two-pole cylindrical NdFe42 magnet with relative permeability $\mu_r=1.099$ and magnetic coercivity of 926 kA/m is chosen for numerical simulations using ANSYS Maxwell [80]. The magnetic coercivity of 926 kA/m corresponds to a remnant magnetic flux (B_r) equals to 1.28 T . The diameter (d) and length (l) of the magnet are $d= 0.3175 \text{ cm}$, and $l=5.08 \text{ cm}$, respectively. The same magnet with these features are used in the following sections for the measurements. The initial magnetization vector is also assumed to be along the x -axis ($\varphi_i = 0$). The next step is to assign rotational motion to the magnet in ANSYS Maxwell. For this purpose, a “band object” is required to be defined first. The band object is a vacuum object which separates moving parts and stationary parts of a simulation

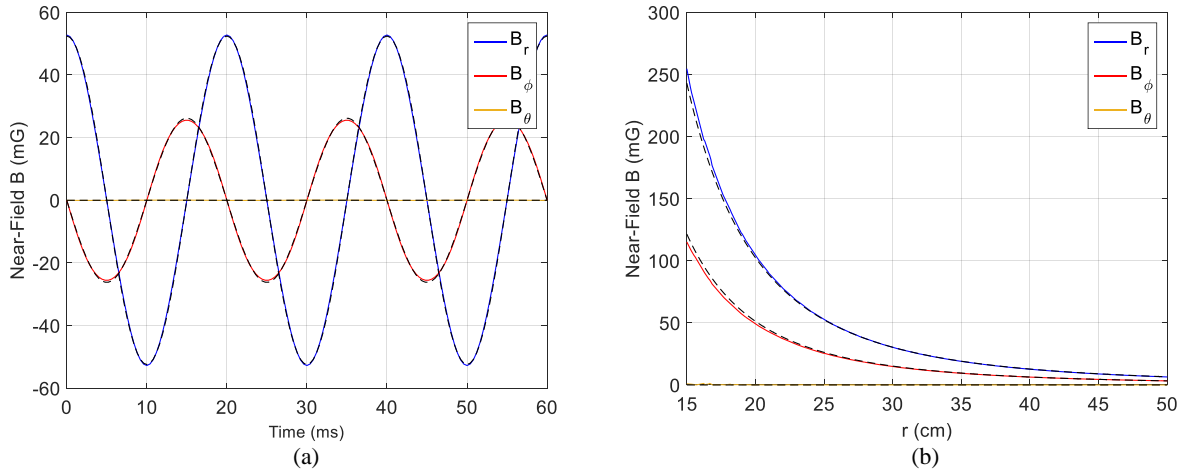


Figure 2.2. (a): Time profile of near-field \mathbf{B} at a point along the x axis (25 cm away from the magnet's center). The \mathbf{B} -field components have frequency of 50 Hz. (b): Near-field components of magnetic field (\mathbf{B}) as a function of distance along the x -axis. The solid lines are the numerical results and the dashed lines represent the analytical solution.

model. All the model components encompassed by the band object, undergo a pre-selected motion. This motion can be either rotational (around any of the coordinate system axes) or translational. In our simulations, by defining a band object for the magnet and choosing rotational motion, the frequency of spinning around the z -axis is set to be 50 Hz. The reason for choosing such low frequency is the fact that all the measurements are performed for a 50Hz-rotating magnet (for fabrication simplicity). The same results are valid for ULF/VLF bands. For the simulation setup, transient magnetic solver is chosen. This transient solver solves for the instantaneous magnetic field at each time-step using a highly accurate finite element method. The time-step value of 0.2 ms is used here to have 101 sample points in every period. The time domain profile of B -field components at a point along the x -axis (25 cm away from the magnet's center) is plotted in Figure 2.2(a). As obvious from this figure, the magnetic field in space has a fundamental frequency of 50 Hz. Considering the cylindrical symmetry of the problem, the amplitude of time-harmonic B -field components along the x -axis is calculated numerically and compared with the analytical solution (Eq. (2.8)) as shown in Figure 2.2(b). As expected, the field profiles follow the known

$1/r^3$ behavior. Moreover, excellent agreement is observed between the numerical results and the analytical solution.

2.3. Theory of the Proposed Phase Modulation and Frequency Multiplication

2.3.1. The Concept

As explained in the previous section, the EM field profile associated with a rotating magnet is purely sinusoidal. To achieve signal modulation, the simplest solution would be to change its frequency instantaneously. However, the frequency modulation suffers from narrow bandwidth and poor efficiency because of mechanical limitations. On the other hand, the amplitude modulation provides improved bandwidth but the operation of commutation using AM is highly sensitive to the additive noise [74]. It is well-known that phase modulation compared to the amplitude modulation is less sensitive to the noise. The main idea for achieving the phase modulation is depicted in Figure 2.3. This approach is based on modulating the amplitude of rotating magnet's sinusoidal EM fields with a square wave first and then controlling the zero-crossings (or peaks) of the modulated signal through shifting the square wave in the time domain to achieve the desired phase modulation. However, as explained and also simulated in the following sections, it will be shown that such perfect and selective cancellation (square wave with 0, +1 values) is just an ideal scenario and practical limitations will impede creation of such waveforms. The proposed geometry to achieve the desired amplitude and phase modulation for a rotating magnet is illustrated in Figure 2.4. It is based on the application of a material with high relative permeability (μ_r) as a stator in the design. In fact, the rotating magnet is sandwiched between two pairs of slowly-moving orthogonal bow-tie shape high- μ plates. The principle of operation of this structure can be explained through the analogy of its dual. According to the image

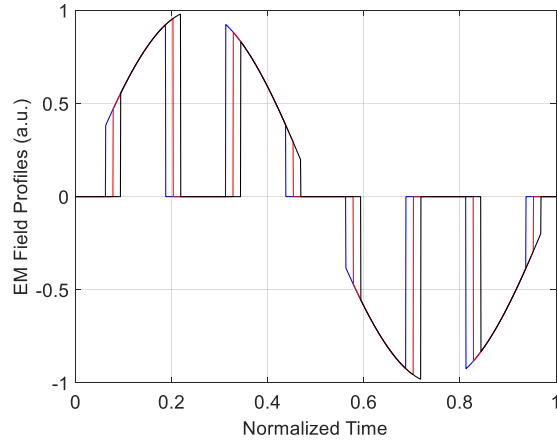


Figure 2.3. Main idea (desired solution) for achieving phase modulation. Each curve represents an amplitude-modulated sinusoidal signal shifted in the time domain (having a distinguished phase).

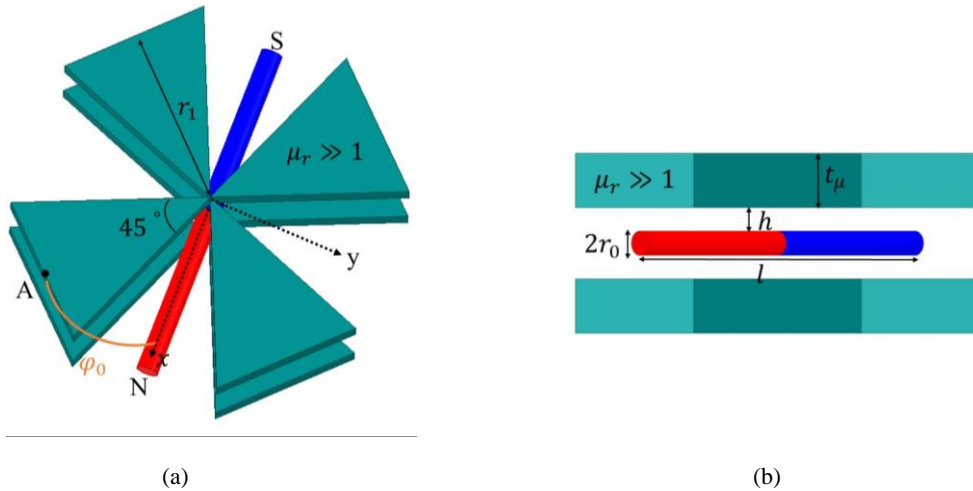


Figure 2.4. (a): Three dimensional proposed configuration for achieving phase modulation and frequency multiplication in a mechanical antenna. The rotating magnet is sandwiched between two pairs of orthogonal bow-tie shape high- μ magnetic plates. φ_0 is measured between the point A and the x -axis (b): Its side view.

theory [81], placing charges of an electric dipole near the surface of a sphere made up of a high-permittivity material reduces its field amplitudes. As shown in Figure 2.5(a) and Figure 2.5(b), for the special case where $h \rightarrow 0$, images of a positive point charge on a dielectric sphere with high relative permittivity ($\epsilon_r \gg 1$) are a positive charge at the center and a negative charge just below the charge on the surface. The latter charges will cancel out each other. The same is true for the negative charge of the dipole on the surface. The positive image charge on the surface will be

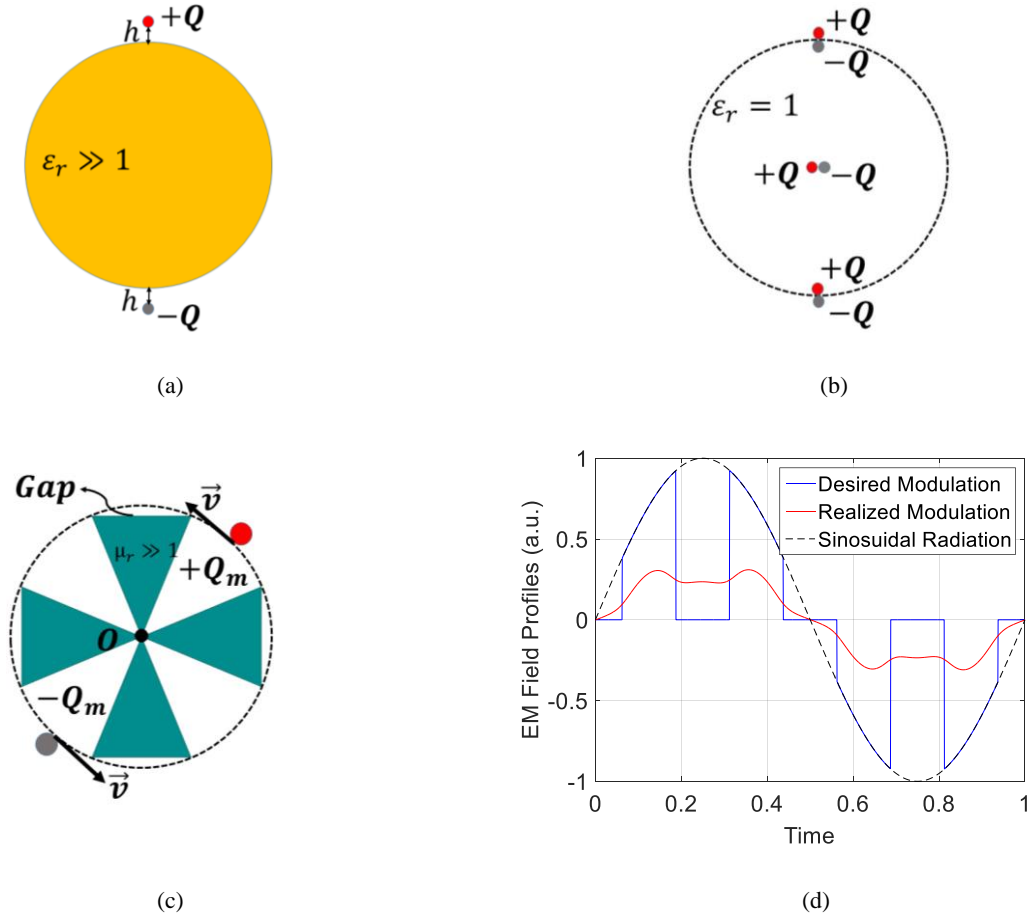


Figure 2.5. (a): An electric dipole is brought in the proximity of a dielectric sphere with large permittivity. The separation distance between the charges and the sphere is h . (b): Its equivalence based on the image theory for a special case when $h \rightarrow 0$. (c): Top-view of proposed configuration for achieving phase modulation (the rotating magnet is modeled as rotating magnetic dipole). (d): Comparison between desired and realizable amplitude modulation through using bow-tie shape magnetic plates (in one time period).

cancelling out the negative charge of the dipole and the second image is a negative charge at the center that cancels out the image of the positive dipole charge at the center. As a result, there will be no net radiation if a high-dielectric material is brought in very close proximity of a rotating electric dipole. In practice, the existence of the gap (h) and the resulting fringing fields would not allow for such perfect cancellation of the radiation. Likewise, placement of a material with high relative permeability ($\mu_r \gg 1$) between charges of a rotating magnetic dipole could stop its radiation based on the duality theorem. Consequently, if a high-permeability material with configuration depicted in Figure 2.5(c) is brought in close proximity of a rotating magnetic dipole,

its sinusoidal EM field can be amplitude-modulated. Every time the magnetic charges appear in front of the bow-tie shape magnetic plates, the radiation is reduced significantly. It should be also noted that the presence of magnetic material causes lower EM field intensities for all the times than what could be achieved from the rotating dipole in the absence of the high- μ plates. Figure 2.5(d) compares our desired and actual amplitude modulation (obtained from the following section simulations). In fact, the resulting signal, although qualitatively agree with the ideal case, is quantitatively different but still has significant harmonic contents. For achieving phase modulation, by slowly displacing the initial position of the magnetic plates and rotating them independently around the origin (O), emitted EM fields will be attenuated at different time slots and thus the phase of the signal can be changed. Consequently, in the proposed configuration in Figure 2.4 which is the 3D realization of Figure 2.5(c), every time the rotating magnet passes in between the magnetic plates, its radiation is reduced significantly. Changing the initial position of the magnetic plates with respect to the rotating magnet (changing φ_0) modulates the radiated EM signal and at the same time modulates the phase [82], [83]. Following subsection is dedicated to the numerical verification of this idea.

2.3.2. Near-Field Numerical Simulations and Parametric Studies

To prove this concept, a rotating permanent magnet sandwiched between two pairs of orthogonal bow-tie shape magnetic plates is simulated using ANSYS Maxwell. It is assumed that the magnetic plates are ferrite slabs with $\mu_r = 600$. The magnet has the same dimensions and properties as described in Section 2.2.2. The rotation frequency is set to be 50 Hz. The initial magnetization vector is assumed to be along the x -axis and the orthogonal plates are placed such that $\varphi_0 = 0$ (see Figure 2.4(a)). To ensure the magnet is covered completely by the magnetic

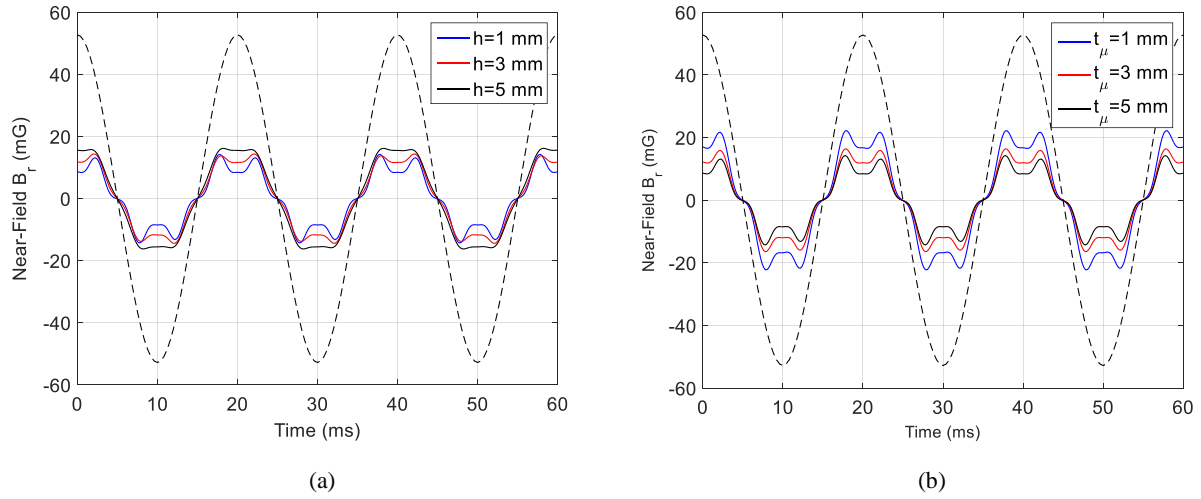


Figure 2.6. (a): Time domain radial magnetic field (B_r) in the near-field region at a point along the x -axis for (a): various distances between the magnet and ferrite sheets (h), (b): various ferrite thicknesses (t_μ). Dashed line represents the corresponding magnetic field without the presence of magnetic plates.

plates while rotating, r_1 is set to be 26 mm ($> l/2 = 25.4 \text{ mm}$). Important design parameters which would affect the field modulation performance by the magnetic plates are the relative permeability of ferrite sheet (μ_r), its thickness (t_μ) and its distance from the magnet (h) as all defined in Figure 2.4(b). Figure 2.6(a) shows the time domain profile of simulated B_r at a point along the x -axis (25 cm away from the magnet's center) for different h values with $t_\mu = 5 \text{ mm}$. It can be concluded that the magnetic field intensity is reduced within certain time slots which is the duration at which the magnet is sandwiched by the high- μ material. As can also be observed, the closer the ferrite posts are to the magnet, the stronger is the field suppression which corresponds to the deeper amplitude modulation. However, in practice, if the ferrite plates become too close to the magnet, they attract the magnet and stop its mechanical rotation. That's why the perfect cancellation of the field is impossible. For the rest of the simulations and measurements, we have set $h = 3 \text{ mm}$. A parametric study is also performed on the thickness of ferrite sheets (t_μ) the result of which is shown in Figure 2.6(b). As expected, thicker ferrite slabs would result in stronger field suppression and of course at the expense of weaker \mathbf{B} -field. It should be noted that since the magnet

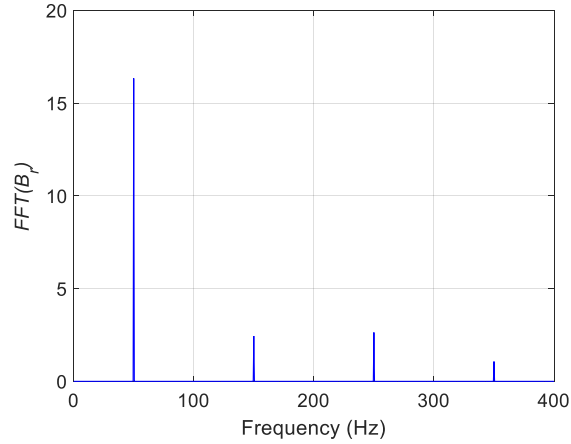


Figure 2.7. Fourier transform of the near-field B_r with the time-domain profile given in Figure 2.6 ($h = 3$ mm, $t_\mu = 5$ mm).

is volumetric in its nature and is not exactly identical to charges of a magnetic dipole, the field suppression phenomena does not occur perfectly. One interesting phenomena associated with the amplitude distortion is the strong harmonic generation which results in frequency multiplication. In fact, higher harmonics of the rotation frequency (50 Hz) are generated as can be observed from Figure 2.7. Taking the Fourier transform of the \mathbf{B} -field components illustrates that the near-field EM components have the odd harmonics of the rotation frequency. As will be shown in the following sections, the higher harmonics of the signal decay slower with range compared to the fundamental frequency in the near-field range ($\propto 1/(kr)^3$) and carry more power in the far-field domain ($P_{rad} \propto \omega^4$).

To verify the phase modulation capability, the initial position of the magnetic plates with respect to the initial position (φ_0 , see Figure 2.4(a)) is varied from -20° to 20° and the simulation results for B_r are shown in Figure 2.8 at the same observation point as in the previous analysis. The magnetic fields are plotted over one cycle ($T = 20$ ms). The phase modulation phenomena can be readily observed in this figures. As illustrated in Figure 2.9, by taking the Fourier transform of the B_r and B_φ components, higher odd harmonics of the rotation frequency (150, 250, 350, 450

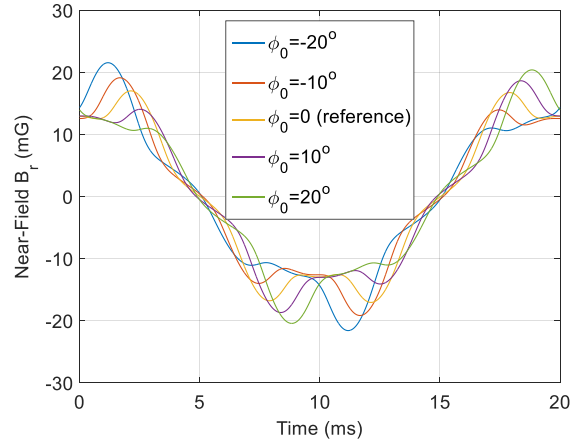


Figure 2.8. The effect of magnetic plates' initial position (φ_0) on the near-field B_r . Variation of φ_0 gives a unique phase to the EM field.

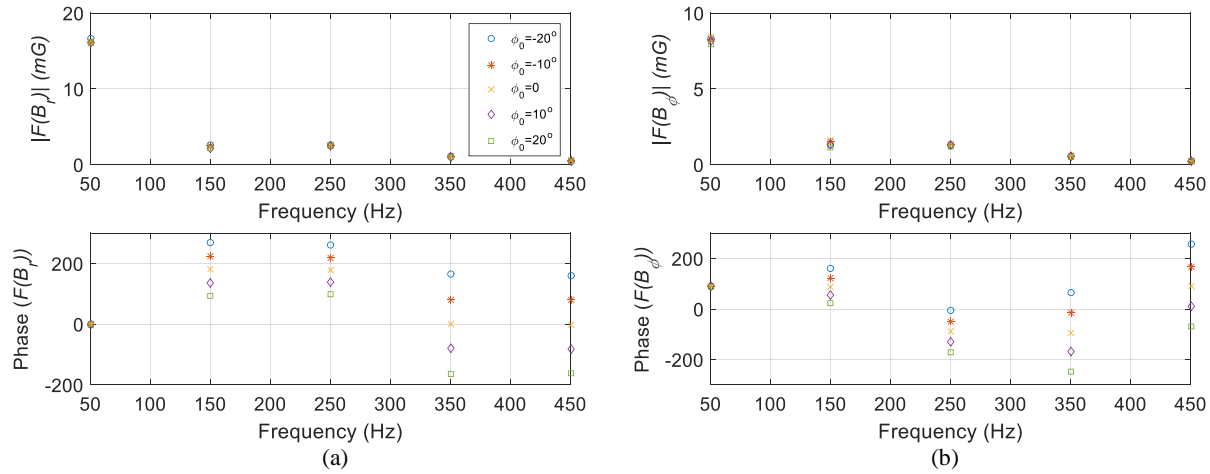


Figure 2.9. The effect of magnetic posts initial position (φ_0) on the amplitude and phase of the frequency components of (a): B_r fields and (b): B_ϕ fields. Changing the initial position of the magnetic posts, changes the phase corresponding to odd harmonics of the rotation frequency (50 Hz). All the phases are in degree.

Hz) are all generated. Additionally, these higher harmonics demonstrate phase variation as φ_0 changes. The numerical simulations also indicate that the phase variation is not a function of observation point and in fact all the points in the 3D space show the same phase variation. Therefore, using such modulation scheme, one can transmit different information signals through variation of φ_0 . Table 2.1 summarizes the phase variation dependency of the rotation frequency

Table 2.1. Phase Variation of the Rotation Frequency Harmonics of the Near-Field for Different Values of φ_0 (with respect to $\varphi_0=0$).

Ferrite initial position (φ_0)	1 st Harmonic	3 rd Harmonic	5 th Harmonic	7 th Harmonic
-20°	-0.45°	88.8°	81.7°	163.1°
-10°	0.17°	43.7°	40.3°	77.6°
10°	-0.1°	-44.3°	-40°	-81.3°
20°	0.72°	-88.1°	-78.1°	-164.9°

harmonics on the φ_0 . The fundamental harmonic has no phase modulation through variation of φ_0 while, the third and fifth harmonics get approximately an additional phase of -40° for each 10° rotation associated with the φ_0 . The seventh and ninth harmonic also get an additional phase of -80° for each 10° rotation of φ_0 , but because of their relatively small amplitude compared to the previous odd harmonic are not the focus of this work. For mathematical explanation of the phase variation values, see the Appendix A.

2.3.3. Far-Field Semi-Analytical Simulations

As mentioned before, the majority of numerical simulation software are not capable of performing far-field simulations at very low frequency bands. So far, we have investigated the performance of proposed mechanical antenna in the near-field region. To study its performance in the far-field region, one can take the advantage of the uniqueness theorem along with the reciprocity theorem. This method has been effectively utilized to compute the second-order scattered field of two adjacent objects using only the knowledge of scattering from isolated objects [84] and in calculation of the far-field from the measured electric near-field over an arbitrary surface [85]. According to the uniqueness theorem, to determine the EM fields of a radiating structure (here, the rotating magnet integrated with ferrite plates) everywhere in the surrounding

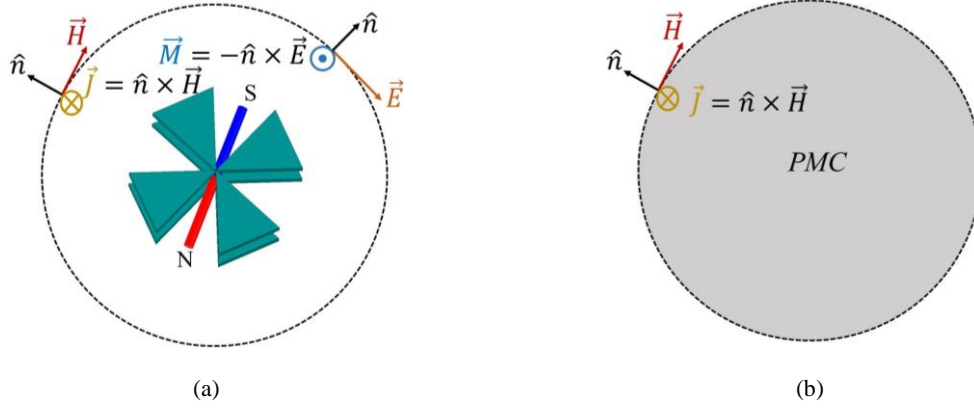


Figure 2.10. (a): The application of uniqueness theorem for finding the far-field components of the rotating magnet integrated with ferrite sheets. (b): The Application of the uniqueness theorem when only the information about the magnetic field components exists.

space, it is only required to have the knowledge of the tangential electric field, or tangential magnetic field, or both on the surface of a hypothetical closed surface around the structure [81]. As depicted in Figure 2.10(a), these tangential electromagnetic field components can be modeled as surface electric and magnetic current densities to find the associated radiation everywhere. As the quasi-magnetostatic solver used here, ANSYS Maxwell, only provides the magnetic field components not the electric fields, to use the uniqueness theorem effectively, we can assume that the hypothetical closed surface around the radiating structure is filled with a perfect magnetic conductor (PMC). Therefore, the problem of finding the far-field components of the rotating magnet reduces to the problem of finding the radiation of the equivalent surface current density (electric) over a PMC sphere as illustrated in Figure 2.10(b). To further simplify the problem, the reciprocity theorem can be utilized as follows. Knowing the fact that EM fields associated with a short electric dipole (\vec{J}) can be approximated by plane waves in its far-field domain, the problem of finding radiation from a surface current density over a PMC sphere (problem 1) is reduced to the problem of scattering from the same PMC sphere illuminated by a plane wave (problem 2) as,

$$\iint \vec{E}_1 \cdot \vec{J}_2 dv = \iint \vec{E}_2 \cdot \vec{J}_1 dv \quad (2.9)$$

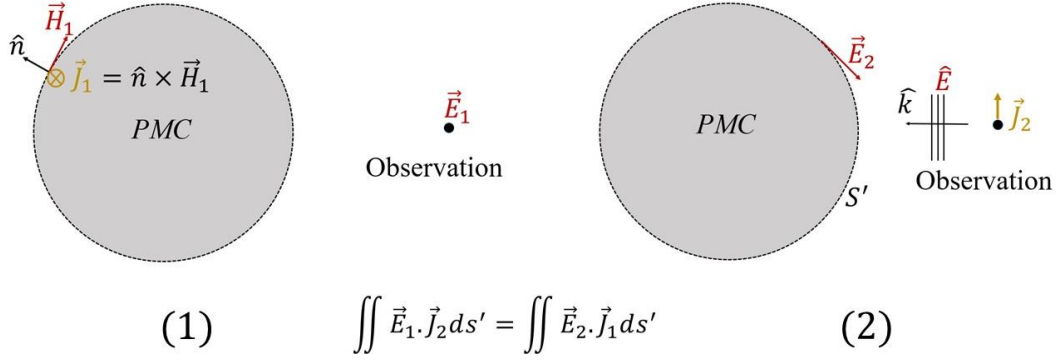


Figure 2.11. The application of reciprocity theorem for finding the radiation of a surface electric current over a PMC sphere.

where, as shown in Figure 2.11, \vec{E}_1 is the far-field electric field associated with the rotating magnet integrated with the ferrite plates, \vec{E}_2 is the total surface field over the PMC sphere illuminated by a plane wave, \vec{J}_1 is the surface current density over the PMC sphere calculated from magnetic field components of the radiating structure in its near-field region, and \vec{J}_2 is a short electric dipole oriented arbitrarily in the far-field region ($\hat{\theta}$ or $\hat{\phi}$). Having obtained the analytical solution for the total electric field over the PMC sphere (\vec{E}_2) illuminated by a plane wave for any arbitrary direction (\vec{J}_2) [86], and extracting the time-domain profile of magnetic field components of the proposed mechanical antenna numerically (ANSYS Maxwell) over an sphere with the same radius as the PMC sphere (here, $r = 60 \text{ cm}$) and then taking their Fourier transform to find the corresponding phasor expressions ($\vec{J}_1 = \hat{n} \times \vec{H}$), the radiation pattern of the mechanical antenna is calculated using Eq. (2.9) and is shown in Figure 2.12. It should be noted that all the rotation frequency harmonics (first, third, and fifth) have the same radiation pattern. Then, by changing the initial position of the magnetic plates (φ_0) for every ten degrees, the equivalent electric current density is calculated numerically for each case and the corresponding phase variation for the electric or magnetic field components in the far-field region is calculated (which is the same as it is a plane wave), the result of which is summarized in Table 2.2. Similar to the near-field simulations, for

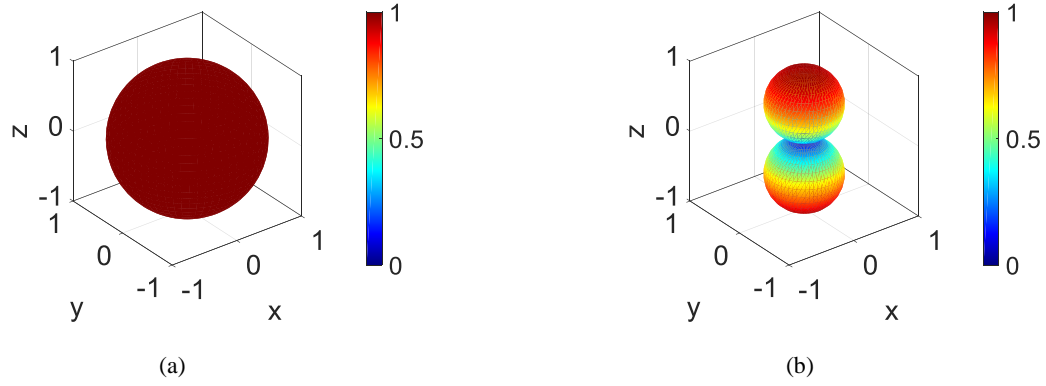


Figure 2.12. The radiation pattern of the proposed mechanical antenna. (a): $E_\theta (H_\phi)$, (b): $E_\phi (H_\theta)$. The E_θ has an isotropic radiation pattern.

every 10° rotation of the magnetic plates, the third and fifth harmonics undergo a phase variation of approximately 40° . Also, the fundamental harmonic (50 Hz) has no phase variation for a slowly rotating magnetic plates.

One important parameter of interest is the total radiated power for the proposed mechanical antenna. As shown in Figure 2.6, the electromagnetic field components of the antenna with amplitude and phase modulation are smaller than the corresponding ones for the rotating magnet in the absence of the magnetic plates. But, since the proposed configuration provides a frequency multiplication feature (generation of higher odd harmonics) and the radiated power is proportional to ω^4 according to Eq. (2.7), it is expected this antenna in fact can generate more power in the far-field for the desired harmonic than what can be produced at the fundamental frequency. Considering the same permanent magnet used for the numerical simulations before, using Eq. (2.7), the far-field radiated power from it without the magnetic plates when rotating with frequency 50 Hz is calculated and found to be $2.020 \times 10^{-24} W$. Now, considering the same magnet in the presence of the magnetic plates, the radiated power associated with the fundamental, third, and fifth harmonics are calculated through integration of corresponding Poynting vectors in the 3D space and found to be $2.702 \times 10^{-25} W$, $6.09 \times 10^{-25} W$, and $4.70 \times 10^{-24} W$, respectively. The fifth

Table 2.2. Phase Variation of the Rotation Frequency Harmonics of the Far-Field EM Components for Different Values of φ_0 (with respect to $\varphi_0=0$).

Ferrite initial position (φ_0)	1 st Harmonic	3 rd Harmonic	5 th Harmonic	7 th Harmonic
-20°	0°	79°	80°	159.1°
-10°	0°	39°	39.4°	79°
10°	0°	-41°	-41°	-81°
20°	0°	-81°	-81°	-160°

harmonic in fact carries more power compared to the fundamental harmonic of a single rotating magnet in the far-field region. This unique characteristics again emphasizes on the significance of this mechanical antenna. In general, the magnetostatic analysis cannot predict the relatively small radiation emitting from the rotating magnet. Basically for frictionless motor and ignoring air drag, no power is required to rotate the magnet according to magnetostatic analysis. Hence the additional radiated power in the harmonics cannot be explained by the change in the derived power from the motor. However, intuitively there is a time varying torque delivered by the motor as the permanent magnet crosses through the ferrite plates and thus the net power transferred from the motor to the radiated power generates the harmonics.

Finally, it should be noted that in practice, there are commercial magnetic sensors (magnetometers) with sensitivity as small as 1fT [87]-[89] that would allow reception of such extremely weak magnetic field signals calculated here. Additionally, by rotating larger magnets at higher frequencies (\sim kHz), more power could be extracted from mechanical antennas.

2.4. Fabrication Process and Measurement Results

2.4.1. Fabrication Process using 3D Printing

To demonstrate the concepts of phase modulation and frequency multiplication in the proposed mechanical antenna, we fabricated one prototype of the antenna including a rotating magnet integrated with triangular ferrite plates. A DC motor with maximum rpm value of 50000 (716 Hollow Cup Motor), was used to rotate a 2" long cylindrical N42 neodymium magnet with diameter 0.125" (K&J Magnetics). The same dimensions were also used for the previous numerical simulations analysis. To be able to pass the motor shaft through the bottom ferrite layer for rotating the magnet, we chose trapezoidal shape for bottom ferrite posts as shown in Figure 2.13. Eight triangular and eight trapezoidal ferrite pieces (33P2098-0M0, Laird) with 2.5 mm thickness were cut to be utilized as magnetic posts on the top and bottom of the rotating magnet, respectively. To achieve the 5 mm-thick ferrite sheets as resulted from the simulation optimizations, each two of them were stacked and glued together. The ferrite was cut into the required triangular and trapezoidal shapes using an ADT 7100 dicing saw. This saw is primarily used for cutting silicon wafers into dies, but was in this case able to cut the 2.5mm thick ferrite sheet with a specialty blade. The saw cuts only in straight lines, so several cuts were made at various angles to produce the desired shapes. Prior to dicing, cut marks were engraved into the surface of the sheet with an LPKF Proto Laser S printed circuit board prototyping machine. All the holders for the motor, magnet, and ferrite plates were fabricated using 3D-printing technology and then assembled together.

Figure 2.13 shows the CAD model of our prototype used for fabrication. The plastic holder of the ferrite posts was designed such that it rotates slowly and independently around the center of the

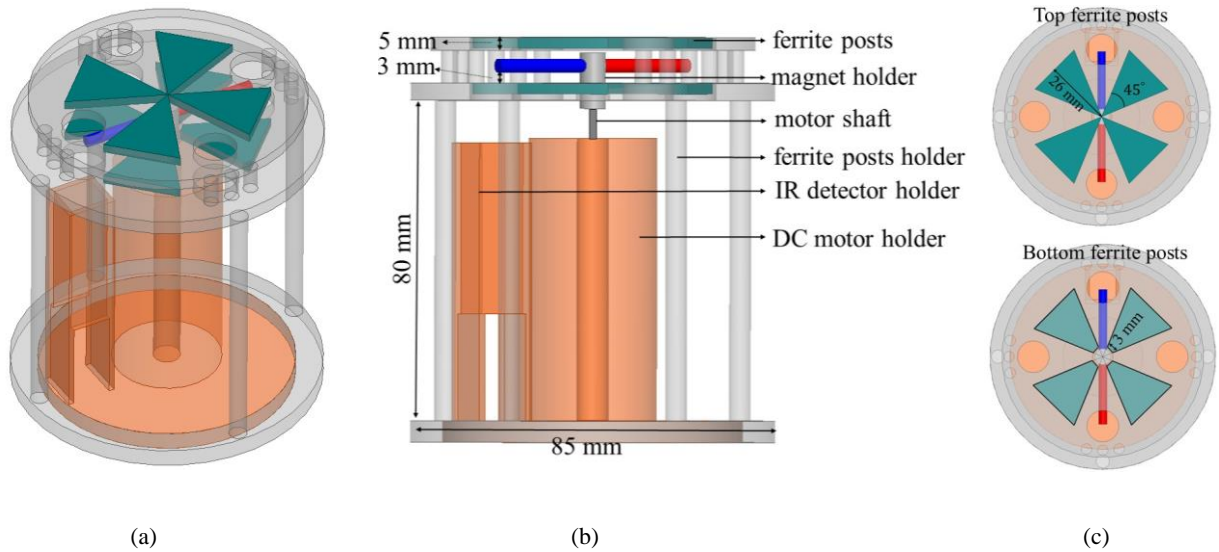


Figure 2.13. (a): Three dimensional CAD model of proposed phase modulating and frequency multiplier mechanical antenna with all its plastic holders. (b): Its side view. (c): Its top view. The bottom ferrite plates are cut into trapezoidal shapes so as to let the DC motor shaft go through them and rotate the magnet.

rotating magnet to achieve the aforementioned modulation. There are also four holes on the top and bottom holders of the ferrite plates which are used for the purpose of trigger signal generation explained in following subsections.

2.4.2. Signal Integrator for Magnetic Field Profile Detection

For measuring the magnetic field profile of the mechanical antenna, a magnetic sensor from the Magnetic Science Company (MC90R) was used [90]. The sensor is cylindrical with cross section's diameter of 29 mm. It measures the \mathbf{B} -field (\mathbf{H} -field) directed along its main axis. In fact, the sensor measures an open-circuit voltage ($V_{oc}(t)$) induced in a multi-turn loop inside it by a time-varying \mathbf{B} -field and then amplified using a low-noise amplifier. One can transfer this measured voltage to the magnetic field strength using a calibrated voltage-magnetic field curve provided by the manufacturer in its datasheet. This transformation is only valid for the magnitude of the \mathbf{B} -field. If one is seeking to measure the time-domain profile of the \mathbf{B} -field, one simple way is to integrate the sensor's output using a low-frequency op-amp integrator. As the sensor has

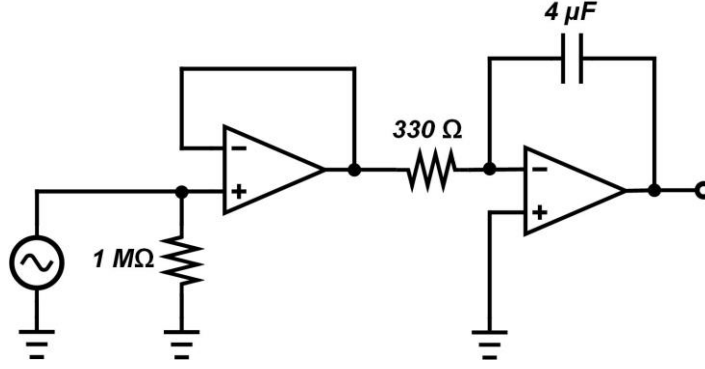


Figure 2.14. Op-amp based integrator circuit used for detection of the time-domain profile of the magnetic field from the magnetic sensor output.

relatively small cross section, the \mathbf{B} -field can be assumed to have uniform distribution across it.

Therefore,

$$V_{oc}(t) = -\alpha \frac{d}{dt} \iint \vec{B}(t) \cdot \vec{ds} \approx -\alpha A \frac{d}{dt} \vec{B}_n(t) \rightarrow \vec{B}_n(t) = \frac{-1}{\alpha A} \int V_{oc}(t') dt' \quad (2.10)$$

Or equivalently in the frequency domain,

$$\vec{B}_n = \frac{-1}{j\omega\alpha A} V_{oc} \quad (2.11)$$

Here α is the proportionality constant which is function of internal amplifier gain and A is the sensor's cross section area. \vec{B}_n and V_{oc} are also phasor representation of $\vec{B}_n(t)$ and $V_{oc}(t)$. Schematic of the designed integrator is shown in Figure 2.14. The first stage acting as buffer, provides 1 MΩ input impedance. This impedance is basically required to have accurate data acquisition from the magnetic sensor. According to its data sheet, the magnetic sensor must be connected to a display instrument with 1 MΩ input impedance (for frequencies below 100 kHz). The second stage (cascaded) is a typical RC op-amp integrator commonly used in low frequency applications. Therefore, the output would be proportional to the magnetic field sensed by the

magnetic probe. The op-amp we used here (THS4031, Texas Instrument) has a cut-off frequency of 100 MHz [91].

2.4.3. Trigger Signal for Phase Modulation Characterization

For detecting the phase modulation, the magnetic sensor output (or the integrator output) was directly connected to an oscilloscope for display. To observe the aforementioned phase modulation in the received magnetic field, we required to generate a reference signal so as to trigger the input of the oscilloscope. The basic idea for generating a simple reference signal is shown in Figure 2.15. It is based on placing a small piece of black color tape placed on one pole of the rotating magnet such that it blocks laser light illumination from the top of mechanical antenna on a phototransistor (IR detector) placed beneath the rotating magnet. Whenever that pole blocks the laser light, the phototransistor generates no current and therefore the output voltage is equal to zero. For the rest of times, the laser shines the phototransistor and its excited current creates a voltage on a resistor ($R_E=47\text{ k}\Omega$) in series with the phototransistor (see Figure 2.15). The phototransistor used here (HW5P-1, adafruit) has a very fast timing response ($2\text{ }\mu\text{s}$) with maximum sensitivity for the green light ($\lambda\sim 550\text{nm}$). Additionally, its photocurrent is reported to be approximately $50 - 70\text{ }\mu\text{A}$. For the measurements, the biasing voltage for the phototransistor (V_{CC}) was set to be 2.4 V.

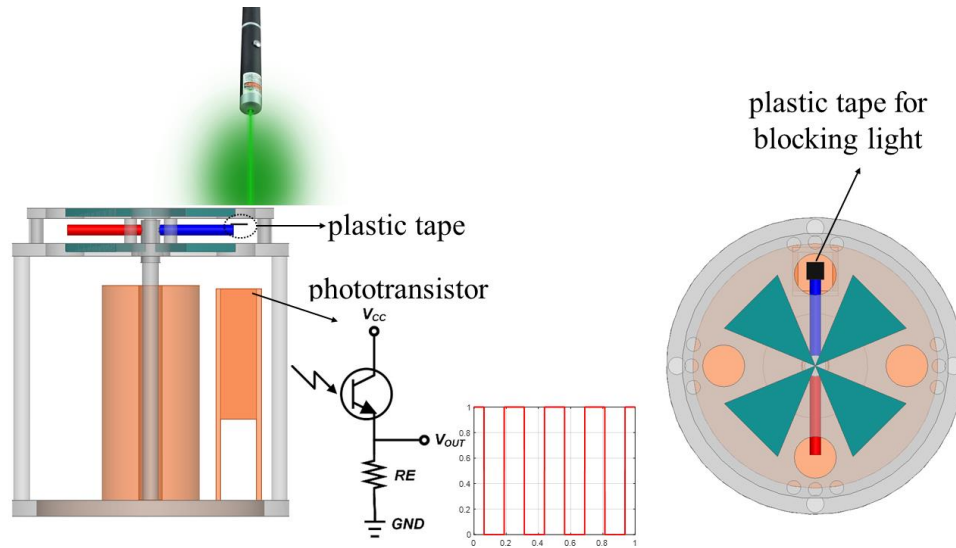


Figure 2.15. The proposed technique for generating a reference signal to detect the phase-modulated signal. A small piece of black tape is used here to block the laser light illuminating a phototransistor from the top.

2.4.4. Measurement Results and Discussions

For most of practical applications, the antenna is used in the near-field zone at ULF/VLF bands. Also, here the measurements were limited only to the near-field ranges. Figure 2.16 depicts the fabricated mechanical antenna composed of the DC motor, rotating magnet, the bowtie ferrite slabs, and the phototransistor (IR detector) with their plastic holders. The ferrite plates' holder can independently rotate around the rotating magnet. A voltage of 0.48 V was applied to the DC motor. The applied voltage rotated the permanent magnet with the frequency 50 Hz. Because our magnetic sensor has sensitivity of around 1 mG, all the measurements were limited to the very near-field region ($r \leq 30$ cm) for proof of concept. Using a larger magnet, a more powerful DC motor, and higher sensitivity magnetic sensors such as the one reported in [72], one can perform the measurements at further distances (tens of meter). In order to make sure the measured magnetic

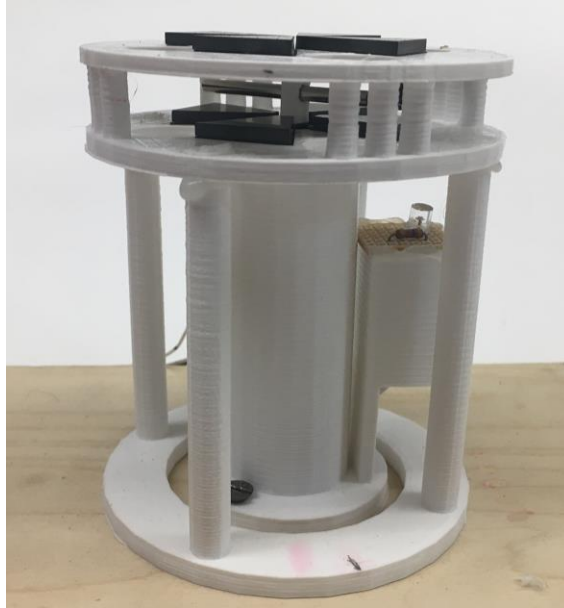


Figure 2.16. Three dimensional view of the fabricated mechanical antenna with phase modulation and frequency multiplication capability. The size of the antenna is 10 cm×8.5 cm. The magnetic plates' plastic holder can independently rotate around the rotating magnet to provide the phase modulation scheme.

field by the magnetometer is just the radiated field by the mechanical antenna and not the motor drive, the motor was first set to rotate only the plastic holder of magnet as a dummy load and no signal was observed. This would guarantee the measured voltages (signals) presented here only comes from the rotating magnet. Figure 2.17(a) illustrates the measured voltage sensed by the magnetic probe for various φ_0 (ferrite posts initial position). The probe was placed along the x -axis (see the previous simulation setup) at $r = 20$ cm with respect to the center of the magnet. For clarification, the voltage is only plotted in one cycle ($T = 20$ ms) as it is periodic. As expected, rotating the magnetic plates will induce a smooth phase variation on the received signal. This measurement setup was also tried to be simulated numerically. Using ANSYS Maxwell, by placing a small circular loop (with the same radius as the probe) perpendicular to the x -axis, the flux passing through it was calculated numerically and then we found its derivative to obtain the corresponding induced voltage, the result of which is shown in Figure 2.17(b). Fairly close

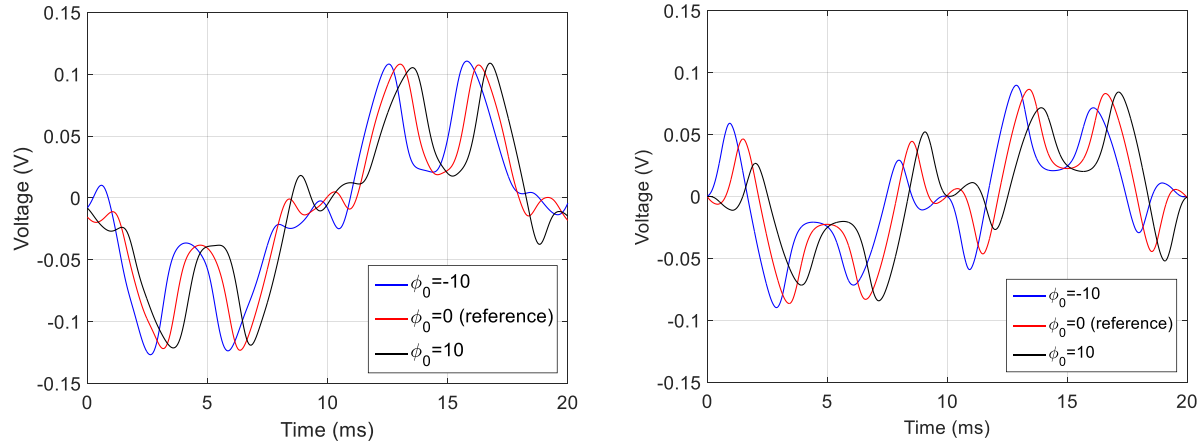


Figure 2.17. (a): Measured voltage using the magnetic probe for various ϕ_0 . (b): Numerically simulated received voltage by the probe. Pretty good agreement is observed.

agreement was achieved between the measurement results and the simulation predictions.

Figure 2.18 also compares the FFT of received voltage in both simulation and measurement setups.

Both datasets are normalized to their corresponding fundamental harmonic amplitude for a better comparison.

As observed, the measurement results also verified the frequency multiplication phenomena very well.

All the odd harmonics were generated and the 5th harmonic had the strongest voltage amplitude after the fundamental tone.

This is because harmonics voltages are proportional

to ω (time-derivative of \mathbf{H}) while the intensity of magnetic field at 3rd and fifth harmonics are

equal (see Figure 2.7). Compared to the simulations, the 3rd harmonic was not detected properly

in the measurements which can be because of uncertainties existing in the real setup including the

optimum distance between the magnet and the ferrite plates ($h= 3$ mm), ripples in the motor

rotational speed and more importantly the sensitivity of the magnetic probe. Compared to the other

odd harmonics, the voltage associated with the 3rd harmonic has smaller amplitude and therefore,

there is possibility of improper detection for this harmonic due to the sensitivity of the probe. The

output of the probe was then connected to the designed op-amp based integrator to find the time-

domain profile of the B_r for various ϕ_0 as shown in Figure 2.19. The phase modulation cannot be

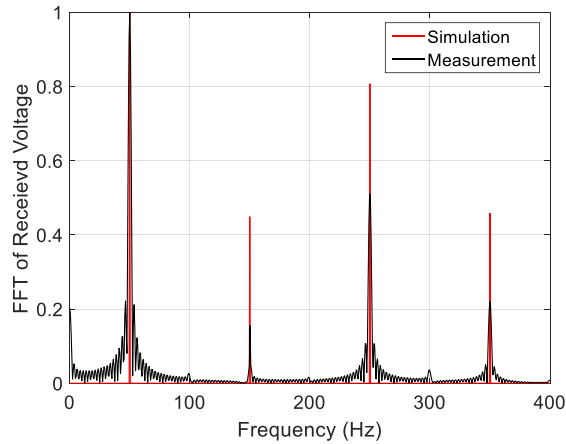


Figure 2.18. Frequency spectrum of the received voltage by the magnetic probe. The frequency multiplication capability can be readily captured from this figure.

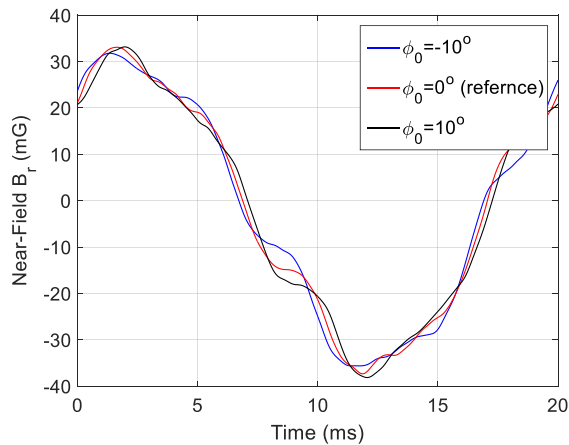


Figure 2.19. The measured time-domain profile of radial magnetic-field (B_r) at $r=20$ cm for various ϕ_0 indicating phase modulation feature.

captured easily from this figure. In order to clarify more this concept, FFT of the measured time-domain magnetic field was calculated through post-processing and the corresponding phase and amplitude of all harmonics are reported in the Table 2.3. A good agreement was obtained between the simulation predictions and the measurements for the phase variation values. However, based on the same argument explained before, magnitude of the 1st and 5th harmonics are in better agreement with the simulations. The fundamental harmonic has no phase variation through rotating

Table 2.3. Comparison between measured and simulated phase variation ($\Delta\varphi$) of the rotation frequency harmonics in the near-field region for different values of φ_0 (with respect to $\varphi_0 = 0$). The given values in parenthesis are the magnitude of \mathbf{B} -fields at frequency harmonics.

Ferrite initial position (φ_0)	1 st Harmonic	3 rd Harmonic	5 th Harmonic	7 th Harmonic
-10° (measurement)	0° (28.55 mG)	52° (1 mG)	42.5° (3.5 mG)	78.6° (1.1 mG)
-10° (simulation)	0.17° (31.46 mG)	39° (4.92 mG)	40° (5.17 mG)	77.6° (2.14 mG)
10° (measurement)	0° (28.44 mG)	-41° (1 mG)	-39.7° (3.6 mG)	-75.2° (0.8 mG)
10° (simulation)	-0.1° (31.56 mG)	-51° (4.25 mG)	-41° (4.94 mG)	-81.3° (1.95 mG)

the magnetic plates. On the other hand, the 3rd, 5th, and 7th harmonics underwent a phase variation of -40°, -40°, -80°, for each 10° rotation of the plates (φ_0), respectively. Although there was a discrepancy between the measured and simulated harmonics amplitudes, the phase modulation phenomena was captured perfectly in the measurements. Figure 2.21 also shows the voltage profile obtained from the phototransistor circuit and used as trigger signal of the oscilloscope. The nulls in the voltage profile correspond to the time slots at which the black tape blocks the laser illumination on the phototransistor. As expected, the trigger signal is independent of φ_0 variation. As the last step in measurements, to study the variation of the magnetic field with distance, the radial component of the magnetic field (B_r) was measured and compared with the simulation predictions shown in Figure 2.20. As can be concluded, the higher harmonics relative to the fundamental harmonic decay slower in the near-field region. This feature in fact emphasizes on the importance of achieved frequency multiplication phenomena again. Additionally, the fields are proportional to $1/r^3$. The measured magnetic field corresponding to the third harmonic is smaller than the simulation predictions because of probably the same reasons explained for the sensor voltage measurement. Finally, it should be stated that such modulation scheme and frequency

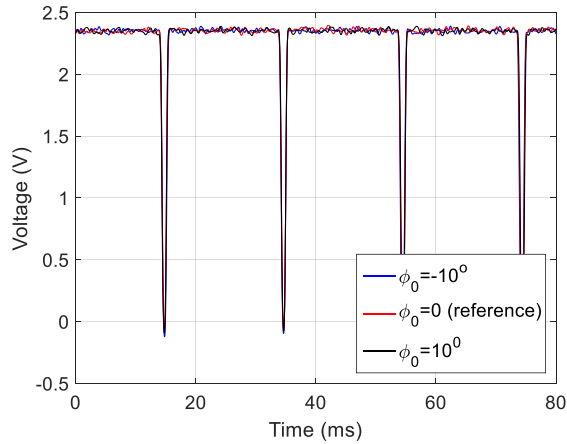


Figure 2.21. The measured voltage from the phototransistor circuit for various φ_0 (in four cycles). This signal is generated to trig the oscilloscope displaying signal sensed by the magnetic probe.

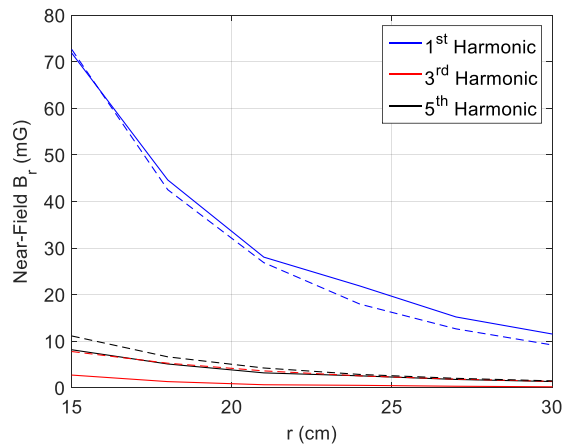


Figure 2.20. The measured (solid line) and simulated (dashed line) near-field B_r as a function of distance (r). Higher harmonics have smaller decay rate compared to the fundamental frequency.

multiplier is readily extendable to higher frequencies (ULF/VLF bands) provided that a more stable mechanical system could rotate a magnet at higher frequencies. For example, by rotating the magnet with frequency of 1 kHz, one can get the radiation at 5 kHz (5th harmonic). It is mechanically impossible with the state-of-the-art tools to rotate a single permanent magnet (which is typically heavy) with frequency of 5 kHz (300000 rpm) to get EM signal at this frequency.

Finally, in order to address the efficiency of proposed mechanical antenna, assuming frictionless shaft for the motor, the only loss term which should be taken into account is the core loss in the ferrite plates. The core loss is composed of two parts namely, eddy current loss and hysteresis loss. As ceramic ferrites (insulators) are used here, there will be no eddy currents and only the hysteresis loss exists. The core loss can be typically estimated using the Steinmetz's equation [24]. However, the Steinmetz's coefficients for the ferrites used here are not provided by its manufacture. An alternative is to use the quality factor. Considering this approach, the maximum power loss in ferrite plates caused by an AC magnetic field with frequency f is,

$$P_{loss} = \frac{2\pi}{Q} \left(\frac{B_s^2}{2\mu_r\mu_0} \right) fV \quad (2.12)$$

where V is the volume of ferrite plates, Q (quality factor) is the inverse of loss factor provided in ferrite data-sheet and B_s is the saturation magnetic flux in ferrites. For the design here, $V = 13.52 \text{ cm}^3$, $B_s = 0.28 \text{ T}$, and $\mu_r \sim 600$. As the reported quality factor for frequencies below 1 kHz is large ($Q > 50$), we expect hysteresis loss is negligible ($< 4 \text{ mW}$) in our proposed mechanical antenna. Then, the system efficiency could be potentially high.

2.5. Conclusion

In this chapter, a novel phase modulation scheme and frequency multiplier for mechanical antennas operating at the very-low frequency bands (kHz frequencies) is proposed. The concept of mechanical antenna (rotating permanent magnet) is first investigated analytically and numerically. Then, idea of frequency multiplication and phase modulation is presented using high- μ materials as a movable stator. It is shown that the phase of transmitting signal from the mechanical antenna changes smoothly with slowly moving the magnetic (high- μ) stators. This

configuration, in addition to the modulation, offers a frequency multiplication where as the magnet is rotated with constant frequency f_0 , the EM signal generated contains all the odd harmonics (f_0 , $3f_0$, $5f_0$, $7f_0$, ...). This feature is really important from the functional point of view as it keeps the rotation speed much lower than the desired radiated frequency. One prototype of a 50Hz-mechanical antenna integrated with the magnetic plates is fabricated and its performance is characterized experimentally. The measurement results indicate that the proposed configuration generates all odd harmonics of the rotation frequency. Also, moving the magnetic plates back and forth will impose phase variation to higher harmonics of the rotation frequency (but, not to the fundamental tone) and thus providing the means for phase modulation.

CHAPTER 3

Fragmented Antennas

3.1. Introduction

Establishing reliable and short range communication with low power in complex environments such as urban, indoor settings and through caves is a challenging task. This is mainly because of the fact that in such complex environments, the presence of large number of scatterers, multipath and shadowing lead to excessive signal attenuation and fast fading at microwave frequencies [92], [93]. These propagation phenomena severely affect the quality of the received signal and impose stringent conditions on the required transmit power and signal processing [22], [94], [95]. In order to enhance the quality and reliability of a communication link in multipath-rich environments, different approaches such as cooperative routing with multiple radios and repeaters [96], [97], multiple-input and multiple-output (MIMO) systems [98], [99], or other diversity schemes [100] have been developed. In addition to the complexity and the cost, such systems typically require significant power which is a major concern for most ad hoc networks. To mitigate some of these adverse effects, operation at low frequencies (VHF and lower) is usually preferred especially for military applications [101], [102], [103]. The main reason is the fact that the wavelength is large or comparable to the size of most scatterers and thus, signals can penetrate significantly through the manmade and natural obstacles and produce far less reflection, scattering, and diffraction compared to what is observed at higher frequencies. Penetration through the soil and building materials at low frequencies allows for direct communication through multi-layer

walls and provides long distance coverage [104], [105]. Recent experimental studies are carried out to show communication between nodes inside and outside of buildings with many walls in between. Such studies prove that low-power and low-frequency radios can establish highly reliable communication links compare to for example a ZigBee radio operating at 2.4 GHz [22], [94].

Despite these advantages at low RF bands, the realization of compact systems is challenged by physically large antennas. This impediment makes the application of such systems limited to large vehicular or stationary nodes. In order to realize mobile communication systems, there is an essential need for extremely small antennas. Major drawbacks of miniaturized antennas are their narrow bandwidth and poor radiation efficiency. Of course, such narrow bandwidth limits the data rate significantly. Hence, the design of reasonably efficient, wideband, and miniaturized antennas is a critical task to enable compact, low-power and low frequency communication with high data rate. Although different types of miniaturization techniques providing better efficiency and bandwidth have been reported in the literature [68], [69], [106], these are not sufficient for the application at hand. For small robotic platforms with relatively small form factors and constrained by their load capacity and available power, an alternative method must be considered for efficient radiation over wider bandwidth.

In recent years, several approaches have been introduced to design antennas for such platforms. Characteristic mode (CM) theory is applied to design antennas for mobile metallic platforms [107], [108] basically by exploiting the metallic body as a large radiating aperture. However, this technique suffers from really narrow bandwidth ($\leq 2.5\%$), unspecified polarization, and radiation pattern. References [109], [110] utilize the wings of the robotic flyer to print and/or install antennas on them. The proposed printed dipole antenna in [109] has a relatively narrow bandwidth ($\leq \sim 4\%$) which may not be appropriate for certain applications requiring high data-

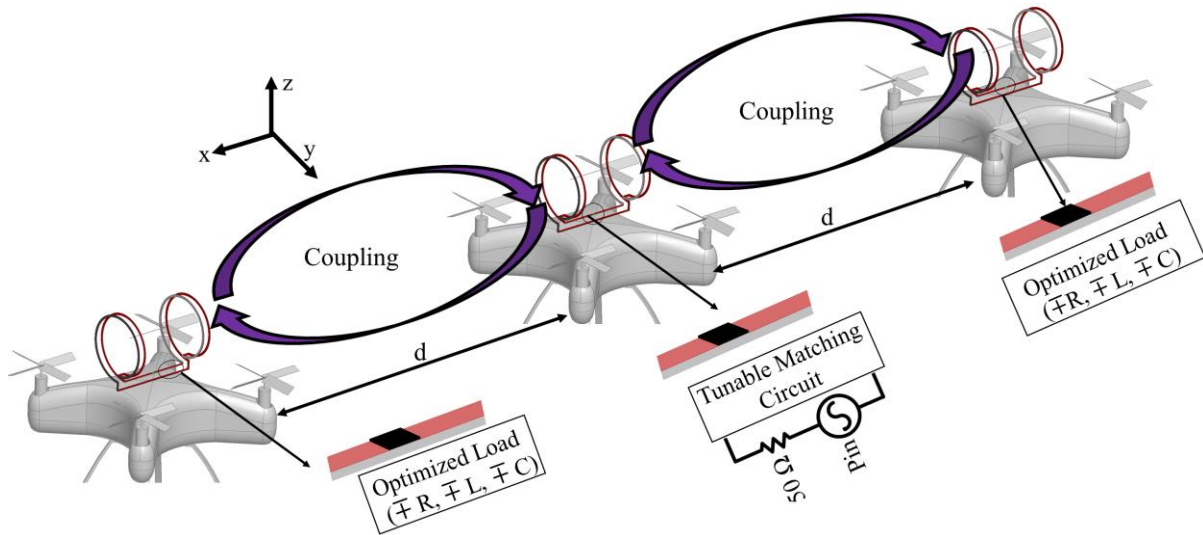


Figure 3.1. The proposed fragmented antenna concept for bandwidth enhancement of miniaturized antenna elements mounted on robotic flyers.

rate. Various types of planar antennas are also proposed for microwave bands [111], [112], intended to be directly attached to the body of the platform. Dimensions of these antennas are comparable to the wavelength and they show wide impedance bandwidth ($\sim 20\%$). Such antennas are, of course, not compatible with the size of small robotic platforms at VHF bands. Thus, a new approach must be considered to design small antennas which can operate at VHF band and if needed can provide wider bandwidth with acceptable high radiation efficiency values. In this chapter, the concept of near-field electromagnetic coupling (electric coupling + magnetic coupling) is applied to a cluster of three detached inductively end-loaded folded dipole antennas mounted on three separate mobile platforms in order to effectively realize a larger antenna and thus, provide wider bandwidth than that of a single element [31]. This concept is shown in Figure 3.1. It is obvious that an antenna with large volume encompassing the cluster of coupled antennas provides a lower quality factor (Q) for the radiation and can effectively radiate electromagnetic waves over a wider bandwidth. For antenna excitation, different approaches have

been used. In one approach, all the antennas are excited simultaneously. This method has the advantage of increasing the total radiated power; however, it is faced with the problem of source synchronization and lower efficiency which is due to the fact that the coupled powers will be dissipated in the other elements source impedances. Another technique is to excite only the middle antenna, while the two adjacent antennas are loaded with lumped elements as shown in Figure 3.1. Application of several simple active and passive load configurations (short circuit, open circuit, $\pm R$, $\pm L$, $\pm C$, and combination) are investigated and an optimization approach is carried out to maximize a cost-function that accounts for the improved fractional bandwidth and the average radiation efficiency ($\bar{\eta}$) over the band of operation. It is shown that the input impedance of the coupled antenna array is highly sensitive to their separation distance with each other requiring a tunable matching circuit. A tunable matching circuit is also proposed to overcome the problems associated with the flight formation fluctuations of the mobile platforms. The proposed fragmented antenna configuration, its design methodology, principle of operation, and measurement results are discussed in the followings.

3.2. Proof of Concept and Design Approach

3.2.1. Single Antenna Design Considerations

Figure 3.1 illustrates the proposed concept for bandwidth and radiation efficiency enhancement where a cluster of three equally-separated miniaturized antennas implemented on three separate robotic flyers radiate and couple to each other electromagnetically in their near-field region. The components of the fragmented antenna are designed so that each piece can operate individually and be able to radiate signals albeit with lower bandwidth. The single radiating element, shown in Figure 3.2, is an inductively end-loaded folded dipole antenna. For simulations

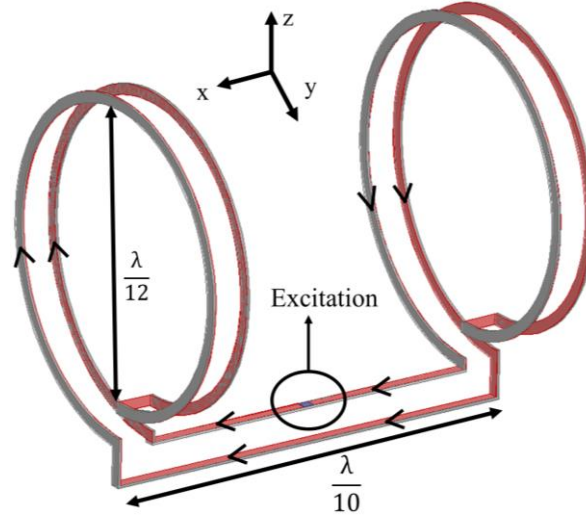


Figure 3.2. The configuration of an inductively end-loaded folded dipole antenna element on a thin printed circuit board.

and analysis, we have assumed that antennas are printed on Rogers RO4003C substrate ($\epsilon_r = 3.55$, $\tan \delta = 0.0027$). Wire antenna configuration is preferred for achieving low-mass and ease of fabrication. There are also two reasons for using these end-loads. The first reason, which will be discussed in details in the following section, is that such inductive end-loads can be used for near-field electromagnetic (electric + magnetic) coupling between adjacent antennas and in effect, provide a large antenna electrical dimension for improved electromagnetic radiation over a wider bandwidth. It should be noted that by making the physical dimensions of the end-loops larger, their near-field coupling range can be increased. The second reason is that the end-loads are used to considerably reduce the linear dimension of the antennas [68], [69]. Using the inductive end-loads, the length of the elements can be reduced to any desired level. In this study, dimensions are reduced to have antennas to be confined within $12 \times 10 \times 10$ cm ($0.096\lambda_0 \times 0.08\lambda_0 \times 0.08\lambda_0$ at 240 MHz) to be able to implement each of them on very small mobile platforms as small as having maximum dimension of 15 cm. As mentioned earlier, miniaturizing antennas will lead to lower radiation resistance and make impedance matching more difficult. It is well-known that folded dipole presents an input impedance four times that of the ordinary dipole. This is the reason a folded

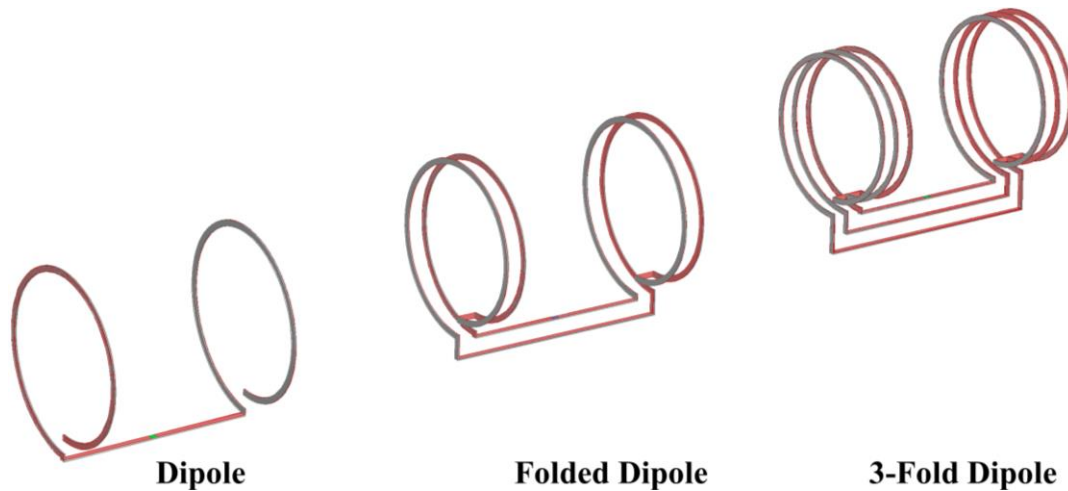


Figure 3.3. The configuration of an inductively end-loaded folded dipole antenna element on a thin printed circuit board.

structure is considered here. We also considered 3-fold and 4-fold dipole structures that are appropriate for smaller size elements for fragmented antenna applications (see Figure 3.3). It is expected that the impedance of smaller elements can be matched using 3- or 4-fold elements. This is because of the fact that an n -fold dipole antenna has effectively n^2 times higher input impedance compared to the ordinary dipole antenna [113]. Full-wave simulations, carried out by HFSS software, show that the input impedance of the ordinary dipole antenna (with dimensions mentioned above) and its folded and 3-fold versions at the resonant frequency are 5.5Ω , 25Ω and 55Ω , respectively. Investigations are also carried out for coupling improvement. Such study is important because higher coupling between the separate antennas allows realization of the proposed fragmented antenna over longer distances for bandwidth enhancement. In addition to having inherently larger bandwidth, we expect that the n -fold dipole antenna can increase the extent of the near-field electromagnetic coupling. To prove this point, Figure 3.4 illustrates the simulated electric and magnetic field intensities normal to the end-loads along their axis for the three versions of the dipole antenna. The end-load diameter can also be increased to enhance the extent of the near-field range. But, in general, the optimal design is subject to the required

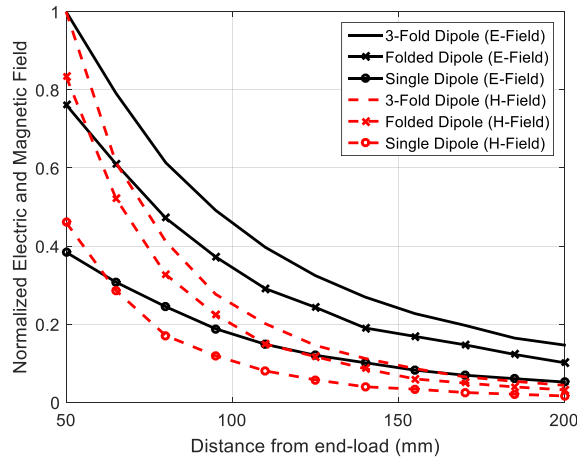


Figure 3.4. The normal magnetic and electric field intensities (along the axis of end-loads, x-axis) associated with the dipole, folded dipole, and 3-fold dipole antennas (all the fields are normalized to the maximum field value which is for the 3-fold dipole antenna).

miniaturization factor that determines the size and the number of the loops (number of folding for the dipole elements). Here, for the ease of fabrication and simple verification of the concept, we have just considered folded dipole antennas as the radiating elements. Another important factor is the direction of rotation of the end-loops with respect to each other and that of their neighbor. Basically, for the two end-loads of each antenna, it is important to figure out whether loops should be in the same direction. It was determined that if the directions are the same, the radiation associated with equivalent magnetic dipole of the end-loops cancel out each other and do not affect the radiation associated with the dipole arms. This is important for achieving maximum polarization purity.

3.2.2. Coupling Mechanisms in Fragmented Coupled Antenna

Based on the proposed configuration for the fragmented coupled antenna, shown in Figure 3.1, three coupling mechanisms between adjacent antennas can be identified as depicted in Figure 3.5. The first one is a magnetic (inductive) coupling between the end-loops of the adjacent antennas via their normal magnetic fields (x-component). The second mechanism is an electric

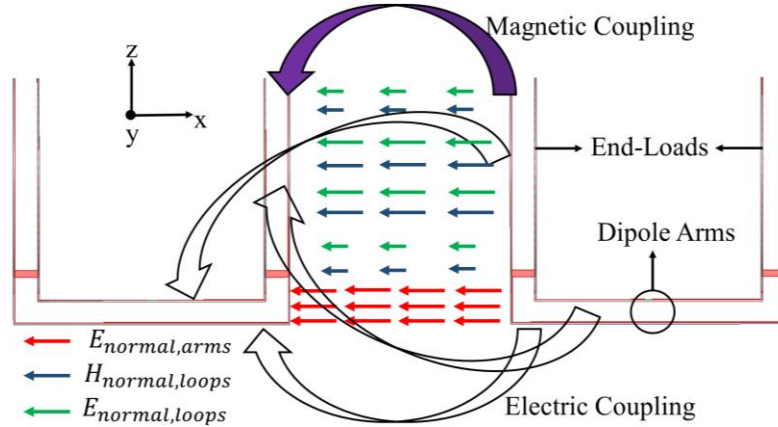


Figure 3.5. The different coupling mechanisms between the adjacent antennas in the fragmented antenna configuration (The end-loops are in the y-z plane and the x-axis is along the axis of the loops).

(capacitive) coupling between the dipole arms. As shown in the Figure 3.5, in the near-field region, the dipole arms of the inductively end-loaded folded dipole antenna have a very strong radial component that can couple to the dipole arms of the adjacent antennas efficiently. The third coupling mechanism is the capacitive coupling between the end-loops and dipole arms. It is well-known that loop antenna with non-uniform current distribution can have very strong electric field along its normal axis [114]. Thus, we expect that the inductive end-loads, which resemble loop antenna with non-uniform current distribution, have strong normal electric field in their near-field region and thus can couple to the dipole arms of the adjacent antennas efficiently. To quantify these couplings and investigate their effects accurately, CAD FEKO software (Method of Moment solver) is used for this section. In a software like FEKO, after performing full-wave simulation on a single inductively end-loaded folded dipole antenna, radiation from its different parts (end-loads and dipole arms) can be analyzed separately. Figure 3.6 illustrates the electric field and magnetic field profiles (normal to the end-loads) of the two dipole arms and the four end-loads associated with each of the single element antennas as a function of distance from the end-load (d). Observation lines are at $z=0$ (along the dipole arms) and $z=50$ mm (along the normal axis of the end-loads) according to the given geometry for the single element antenna (see Figure 3.2). All

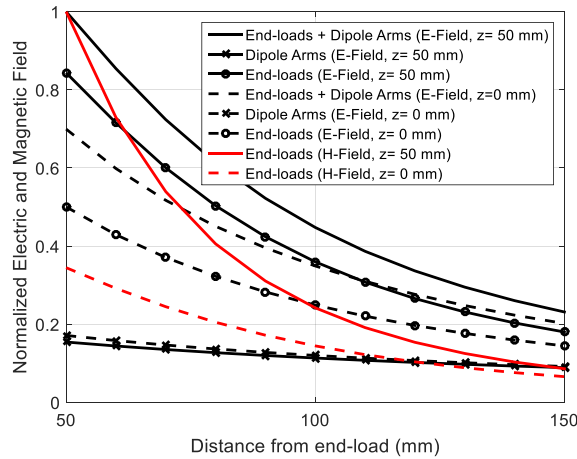


Figure 3.6. The normal magnetic and electric field intensities (along the axis of end-loads) associated with the dipole arms and end-loads of single element antenna shown in Figure 3.2.

the electric and magnetic field profiles are normalized to their corresponding maximum total field ($d=50$ mm, $z= 50$ mm). As shown in Figure 3.6, the electromagnetic radiation in the near-field region is basically dominant by the end-loads rather than the dipole arms. This is because of the fact that the dipole arms are electrically small ($\lambda/10$), whereas the end-loops have the total length of approximately $4\lambda/10$. Next, the magnetic field profile associated with the end-loops decays faster compared to its electric field and consequently, magnetic coupling is more sensitive to the distance between the adjacent antennas. It should be noted that the dipole arms have no normal magnetic field (x -component). That is why only the normal magnetic field associated with the end-loads is plotted in Figure 3.6. Another important point is that in our region of interest (100 mm to 150 mm), the electric coupling between the end-loads and dipole arms is stronger than the electric coupling between the dipole arms. In summary, the antennas in the proposed configuration are coupled to each other electromagnetically (combination of both electric and magnetic coupling).

3.2.3. Fragmented Antenna Design Methodology

So far, we have considered the single antenna design challenges and investigated the

coupling mechanisms between the antennas. Now, the design approach of the proposed antenna geometry for bandwidth enhancement is explained. In this study, we only consider excitation of the middle antenna as the driver while the two adjacent antennas are to be terminated with appropriate lumped-element loads as shown in Figure 3.1. When the current flows on the excited antenna's arms, this antenna not only radiates into the free space, but also couples to the adjacent antennas. The coupled signal will be received and reflected back by the terminals of the adjacent elements and results in a current flow on their arms. Therefore, these elements assist the excited antenna to better radiate into the free space. Hereafter, we refer to the two adjacent antennas as "assistive antennas" and the middle antenna as "driver antenna". It is apparent that the larger the reflection coefficient of the loads is, the higher the radiation efficiency can be if all radiations are in-phase. However, this condition may not necessarily provide a reasonable return loss for the driver antenna noting that the assistive antennas are coupling back to the driver antenna. For this reason, variation of several loads including short circuit, open circuit, purely resistive loads, inductive loads, capacitive loads, and combination of the passive and active loads are considered to examine whether efficient radiation over wider bandwidth can be achieved. It is expected that the application of resistive loads will result in considerable bandwidth enhancement, but this enhancement is mainly due to the dissipation of coupled power in the resistive loads. In this case, the radiation efficiency becomes really poor. On the other hand, the application of purely reactive loads (capacitive or inductive) will not adversely affect the radiation efficiency but can still improve the bandwidth due to the radiation resistance of the assistive elements. It should be noted that the reactive loads can reflect a portion of the power which is partially radiated and partially coupled back to the driver antenna port which in turn adversely affect the return loss. Thus, for any arbitrary load configuration, there is a trade-off between bandwidth enhancement and the radiation

efficiency. An optimization must be carried out for various load configurations to maximize a cost-function defined as

$$C(\text{load}) = \alpha \frac{\Delta f}{f_0} + \beta \bar{\eta} \quad (3.1)$$

Here α and β are two constants normalizing the influence of the fractional bandwidth and the average (over the operating band) efficiency. The proposed cost-function accounts for both bandwidth enhancement and average radiation efficiency over the -10 dB S_{11} bandwidth. The two constants can be chosen to emphasize the bandwidth or the average radiation efficiency or give them equal weight. Noting that the radiation efficiency can attain a maximum value of 100% and the desired fractional bandwidth is 10%, we set $\alpha = 10$ and $\beta = 1$ to give equal weight to average efficiency and the fractional bandwidth. In the analysis that follows, it is assumed that both assistive antennas are terminated with identical loads to ensure symmetry in the radiation pattern of the combined antenna configuration. The optimized load is calculated initially assuming that the separation distance (d) between the adjacent antennas is fixed and equal to one single element's length which is 12 cm. Full-wave simulations are carried out for various aforementioned load configurations to maximize $C(\text{load})$. Simulation results demonstrate that for $d = 12$ cm, the optimized load is a purely capacitive load with capacitance value of $C = 4.4$ pF. Figure 3.7(a) and Figure 3.7(b) compare the fragmented antenna reflection coefficient (S_{11}) and radiation efficiency over its S_{11} bandwidth using the optimized capacitive load with the antenna configuration with a purely resistive load ($R = 36 \Omega$), a purely inductive load ($L = 15$ nH), and also with that of the single radiating element. Full-wave simulations illustrate that the proposed single-element miniaturized antenna provides 25Ω input impedance and bandwidth of 2.4 MHz (1%). As can be concluded from these two figures, the application of resistive load shows considerable bandwidth enhancement; however, its radiation efficiency, as expected, is very low. Moreover, based on these

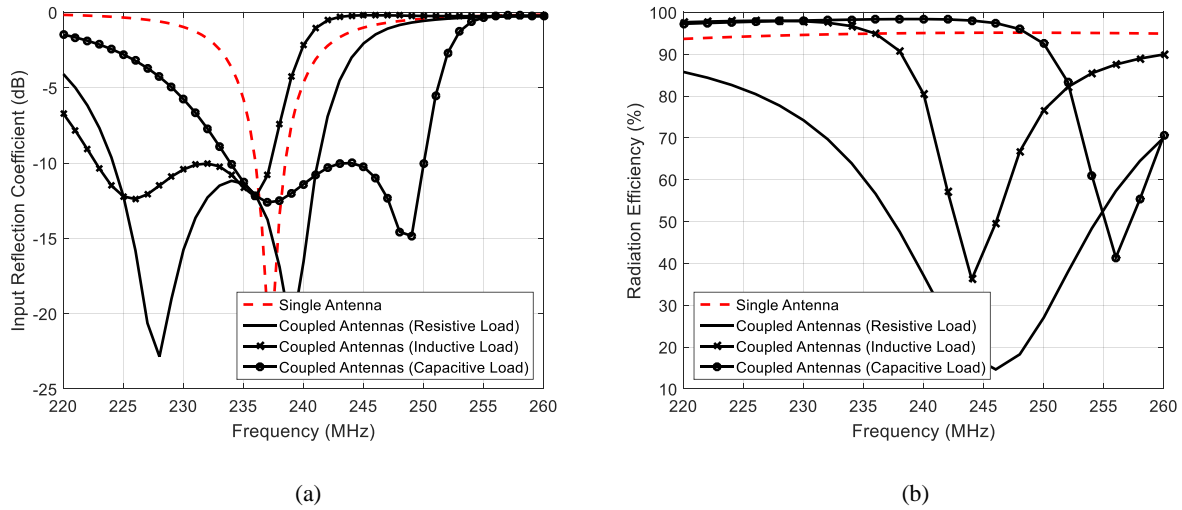


Figure 3.7. The performance analysis of the coupled antennas with optimized load and other possible load configurations in terms of (a): bandwidth, and (b): radiation efficiency. (The radiation efficiency is important only over the -10 dB return loss bandwidth).

simulation results, loading the assistive antennas with the optimized capacitive load results in 16 MHz (6.7%) bandwidth while the optimized inductive load provides 14.5 MHz (6.04%) bandwidth. Loading the assistive antennas with capacitors actually shifts the center frequency to the higher frequencies (>240 MHz), whereas for the inductive loads, this shift is toward lower frequencies (< 240 MHz). As a result, the overall electrical length of the fragmented coupled antenna with capacitive loads is larger than that for the inductive loads. Hence, more bandwidth is expected to be achieved for the capacitive load. In Figure 3.7(b), It is shown that the average radiation efficiency using reactive loads is 97% over the respective S_{11} bandwidths. It is also interesting to note that the fragmented antenna configuration shows one additional resonance due to the electromagnetic coupling of the assistive antennas with the driver antenna. This phenomenon can be explained as follows. The resonant frequency of the assistive antennas will shift due to the capacitive loading. Since these antennas couple to each other, the fragmented coupled antenna should include both the original resonance of the driver antenna and the new resonance of the assistive antennas. In fact, the enhanced bandwidth of the proposed approach is basically the result

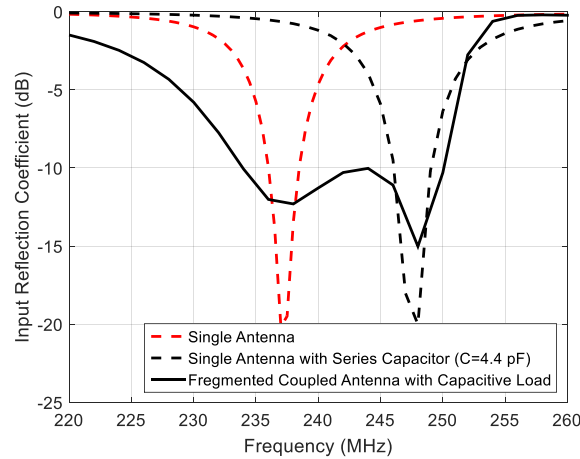


Figure 3.8. The formation of double resonances in the fragmented antenna configuration.

of combining different resonances together via the electromagnetic coupling between the inductive end-loads and dipole arms. Figure 3.8 illustrates this phenomenon clearly for the capacitive load ($C = 4.4 \text{ pF}$) in which the achieved bandwidth is shown to contain the resonant frequency of the driver antenna and the resonant frequency of the assistive antennas loaded with the optimized series capacitor.

3.2.4. Sensitivity Analysis

As mentioned earlier, individual antennas are intended to be placed on very small mobile platforms such as robotic flyers. These platforms typically have small form factor and are highly prone to fluctuations during the flights. For example, the separation distance (d) between the platforms may fluctuate during the flight. In addition, the antennas on the platforms may not be exactly aligned to achieve maximum coupling. To examine such uncertainties, full-wave simulations are carried out to determine bandwidth degradation as a result of such fluctuations. The separation distance (d) between the antennas is varied between 12 cm, and 16 cm while maintaining the alignment of the axes of the end-loops. Figure 3.9 illustrates the coupled signal

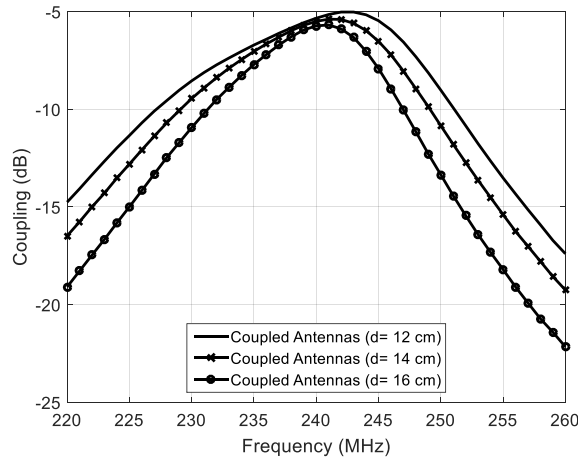


Figure 3.9. The coupling (S_{21} or S_{31}) between the driver antenna and each of the two assistive antennas.

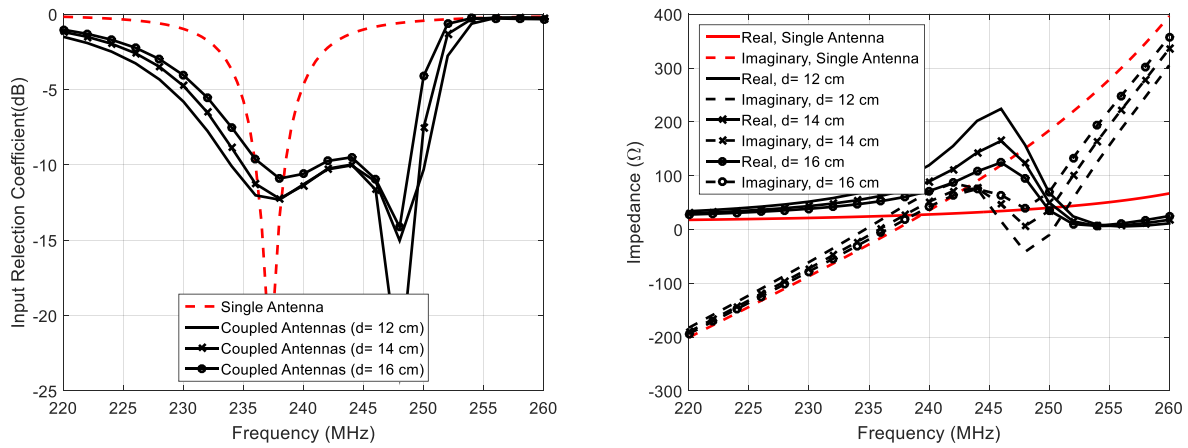


Figure 3.10. (a): The separation distance effect on the bandwidth of the proposed coupled array configuration. (b): The variation of the real and the imaginary parts of the input impedance for different separation distances.

(S_{21} or S_{31}) from the middle (driver) antenna to each of the two assistive antennas. As expected, the longer is the separation distance, the lower is the antennas mutual coupling. This is primarily due to the fact that electromagnetic fields generated by the inductive end-loads decay rapidly away from the center [113] as shown in Figure 3.4. The return-loss and input impedance associated with the fragmented antenna configuration for three separation distances are obtained through full-wave simulations and shown in Figure 3.10(a) and Figure 3.10(b), respectively. As the separation

Table 3.1. Coupled Antennas Characteristics for Different Separation Distances.

Antenna Configuration	$Z_{in}(\Omega)$	BW (MHz)	$\bar{\eta}$ (%)
Single Antenna	25	2.4	95
Coupled Antennas ($d= 12\text{cm}$)	126	16	97
Coupled Antennas ($d= 14\text{cm}$)	110	15	97
Coupled Antennas ($d= 16\text{cm}$)	100	13.5	97

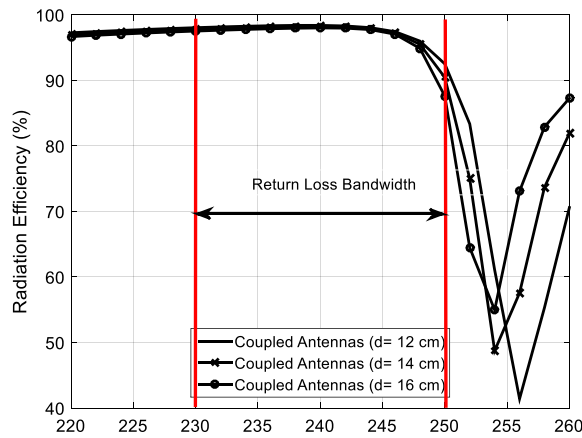


Figure 3.11. The simulated radiation efficiency for different separation distances.

distance between the elements increases, the input impedance and bandwidth enhancement decrease gradually mainly because of the weaker electromagnetic coupling between the antennas. Figure 3.11 also depicts the simulated radiation efficiency for the mentioned separation distances. It is apparent that the radiation efficiency is not sensitive to the distance between the antennas. The calculated average radiation efficiency over the input return loss bandwidth is approximately 97% for all the separation distances (d) and higher than that for the single antenna (95%). The simulation for the radiation efficiency does not consider the effect of Q -factor associated with the capacitive loads because capacitors typically have very large values for their Q (100-1000) at low

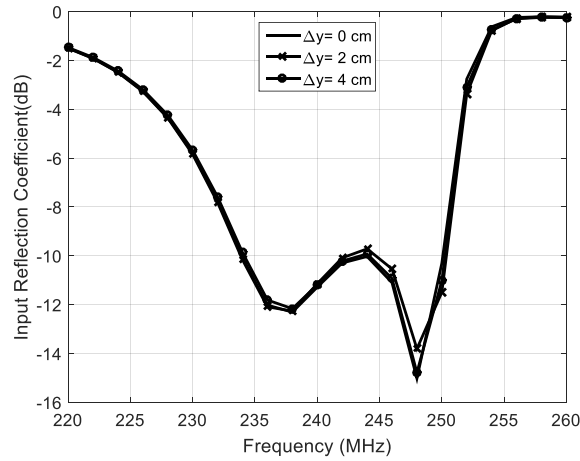


Figure 3.12. The effect of misalignment of the inductive end-loads along the y-direction on the bandwidth of the proposed antenna configuration.

frequencies (VHF band). Table 3.1 reports the input impedance (Z_{in}) of the antenna configuration. In all return-loss and radiation efficiency simulations, it is assumed that the source impedance connected to the driver antenna is equal to Z_{in} . Next, the sensitivity of the coupled antenna bandwidth to misalignment in horizontal plane (the y-axis) is examined. The two assistive antennas are located at a fixed separation distance ($d = 12 \text{ cm}$) from the driven antenna and both of them are shifted along the y-axis by Δy cm (see Figure 3.1). Figure 3.12 illustrates the simulated reflection coefficient for this configuration for two displacement values. It is obvious that the fragmented coupled antennas bandwidth is not highly sensitive to misalignment of the assistive antennas in lateral directions. Not much bandwidth degradation is observed for lateral displacement as high as the end-loop radius. The reason for such observation is that the dipole arms and end-loops have relatively wide electromagnetic field profiles in their near-field region in the y-z plane which maintain the coupling constant. In practice, UAVs are typically equipped with IR range sensors that give them an ability to have accurate estimation of their position relative to other UAVs during the flight in order to maintain a desired flight formation.

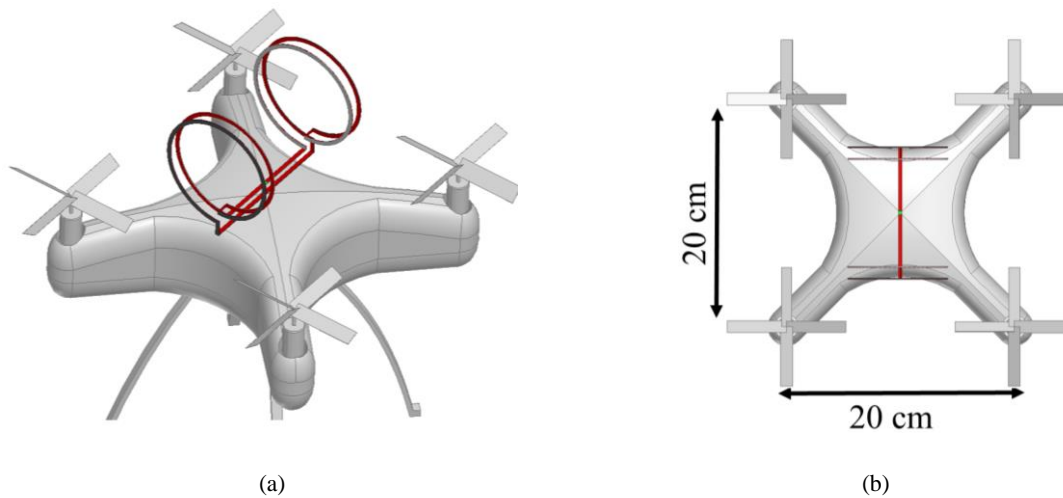


Figure 3.13. The single inductively end-loaded folded dipole antenna mounted on a small dielectric-made ($\epsilon_r = 4$) quadcopter, (a): 3-D view, (b): top view.

3.2.5. Platform Effects on Fragmented Antenna's Performance

Another challenge associated with the placement of the fragmented antenna on the mobile platforms is the presence of the platform itself as a scatterer around the antenna system. Small UAV structures are usually made with composite materials (non-metallic). This is mainly due to the fact that composite materials are much lighter, low-cost, and are much easier to fabricate. It is then expected that the presences of platform itself would not significantly affect the performance of the antenna system. To demonstrate this, an individual inductively end-loaded folded dipole antenna is placed over a dielectric UAV model as shown in Figure 3.13. A composite material with dielectric constant of $\epsilon_r = 4$ is chosen for the body of the UAV. The same full-wave simulations with the same values for the capacitance and port's input impedances as the previous sections are carried out in this investigation. Figure 3.14 illustrates the results for these simulations. It is shown that the presence of the dielectric platform can only cause a very small shift in the center frequency of the operating band which can be accounted for at the design stage. This is because of the fact that the platforms are still much smaller than the operating wavelength ($\sim\lambda/6$)

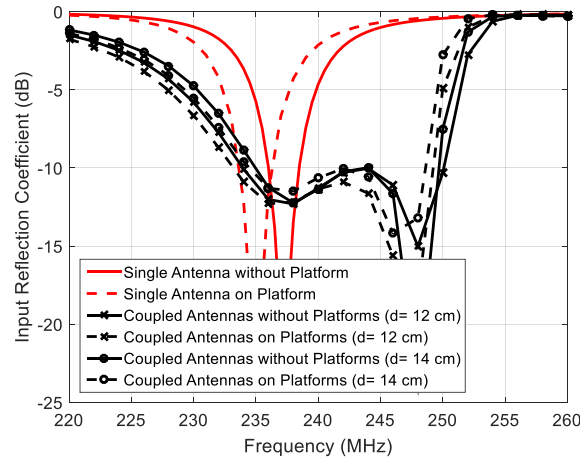


Figure 3.14. The simulation results for comparison between the performance of coupled antennas in the presence and absence of the platform.

and occupy a small fractional volume around the antenna. Therefore, their perturbation effects on the radiating electromagnetic field is negligible. Finally, it should be emphasized that if the antennas are intended for metallic platforms, the platform and antenna should be co-designed to account for platform-antenna interactions.

3.2.6. Tunable Matching Circuit

As observed in the previous sections, deviation from desired flight formation can change the input impedance of the driver antenna. Also, it was mentioned that the antenna on the UAV is expected to operate individually (single element) in the absence of the assistive elements. As indicated in Table 3.1, the range of the input impedance varies from 25Ω for the isolated antenna to 126Ω for perfectly coupled antennas at a set minimum distance $d = 12$ cm. On the other hand, common radios operate with source impedance of 50Ω . This requires a tunable matching circuit to ensure maximum power transfer to the antenna configuration for all possible cases. A simple tunable matching network is proposed based on an L-section LC circuit [115] consisting of one fixed capacitor ($C_1 = 1.5$ nF), one fixed inductor ($L = 68$ nH), one variable capacitor varactor

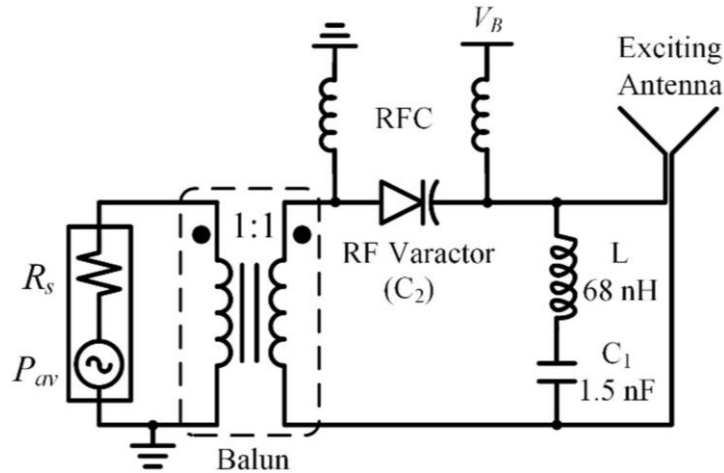
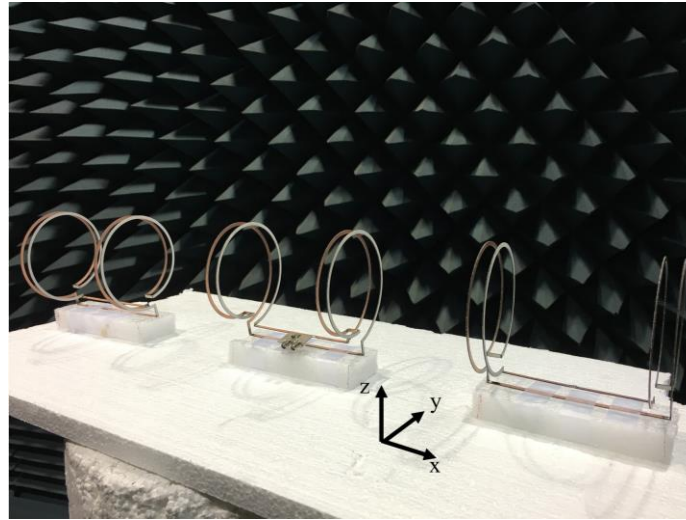


Figure 3.15. The proposed tunable matching circuit containing a tuning diode (varactor).

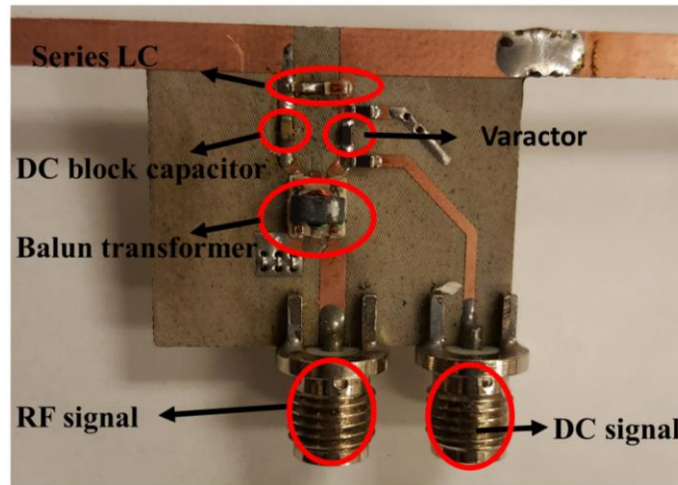
(controlled by a DC voltage V_B), and one Balun transformer shown in Figure 3.15. Two large inductors ($L_{RFC} = 3.3 \mu\text{H}$) are also used as RF chokes in the biasing network of the varactor. The required capacitor (C_2) for $d = 12, 14, 16$ cm are calculated to be 6.8 pF , 8.8 pF , and 8.94 pF , respectively. Based on the required range of the variable capacitor (C_2), a varactor diode from the Infineon Technology (BBY53-02L) is chosen. According to the C-V curve of this varactor diode, the required reverse voltage (V_B) at each separation distance is 2.06 V , 1.88 V , and 1.86 V , respectively. It should be noted that all the simulations associated with the matching circuit are performed using ADS. This circuit is fabricated and integrated with driver antenna. The simulation results are compared with measurement results and reported in the next section.

3.3. Fabrication and Measurement Results

The array of three coupled inductively end-loaded folded dipole antennas described in the previous sections are fabricated for measurement and comparison with the simulation results. The fabricated antennas and the tunable matching circuit are illustrated in Figure 3.16(a) and Figure 3.16(b), respectively. The dipole arms and inductive end-loads are fabricated separately



(a)



(b)

Figure 3.16. (a): Fabricated antennas inside anechoic chamber. (b): Fabricated tunable matching circuit integrated with the driver antenna.

and then soldered together to construct a 3-D antenna geometry. All the components are fabricated with low cost substrate (RO4003C). In practice however, the antennas are to be fabricated with thin copper-coated steel wires to make sure that they are structurally stable. As can be seen from Figure 3.16(a), the assistive antennas end-loops are wound in the opposite direction of the corresponding end-loops of the driver antenna. This way, the magnetic field associated with the adjacent loops of all three antennas will amplify each other and result in a stronger coupling. Figure 3.17 depicts both the measured and simulated reflection coefficient (S_{11}) of the proposed

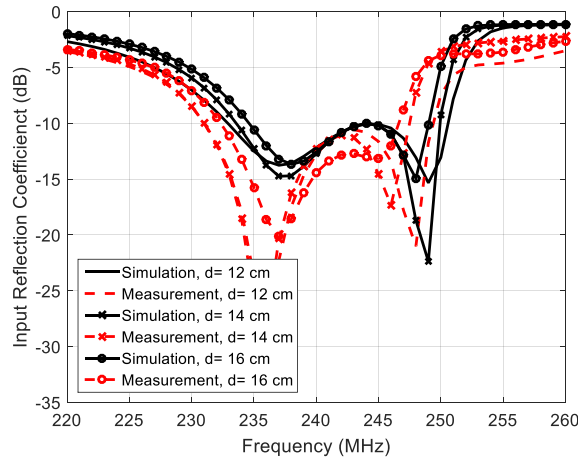


Figure 3.17. The measured and simulated return loss for the different separation distances.

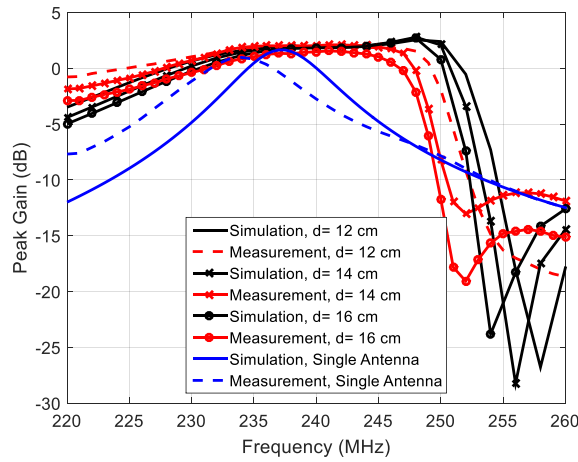


Figure 3.18. The measured and simulated peak-gain (in the boresight direction) over band for the different separation distances.

coupled antenna array for the aforementioned separation distances. It should be noted that in the simulation results, the effect of the matching circuit has been considered. The measured -10 dB return loss bandwidth is given in Table 3.2. It is shown that for $d=12$ cm, the fragmented coupled antenna can provide 18.4 MHz bandwidth (7.7%) which is 7.7 times improvement over the isolated antenna bandwidth. In addition, as the separation distance (d) increases, the bandwidth enhancement decreases. A very good agreement between simulation and measurement results can

Table 3.2. Simulated and Measured Impedance Bandwidth.

Antenna Configuration	Simulated -10 dB Bandwidth	Measured -10 dB Bandwidth
Single Antenna	236 MHz- 238.4 MHz	232.9 MHz- 235.3 MHz
Coupled Antennas ($d= 12\text{cm}$)	232.9 MHz- 250.7 MHz	231 MHz- 249.4 MHz
Coupled Antennas ($d= 14\text{cm}$)	233.6 MHz- 249.9 MHz	231 MHz- 247.4 MHz
Coupled Antennas ($d= 16\text{cm}$)	234.9 MHz- 249 MHz	232.4 MHz- 246.8 MHz

be also seen. For the radiation pattern and peak gain measurements, one wideband log-periodic dipole array (LPDA) antenna operating from 200 MHz to 2 GHz (model 3148B) is used. A calibrated vector network analyzer (VNA) is used to measure the S_{21} between the log-periodic antenna and the proposed coupled antennas inside the anechoic chamber of the University of Michigan. Figure 3.18 illustrates the measured and simulated peak-gain (boresight direction) over the entire bandwidth. It should be noted that the discrepancy between the simulations and measurements for the peak-gain is mainly due to the loss associated with the Balun transformer. Based on its data sheet, the Balun transformer has approximately 0.7 dB of insertion loss. As expected, the peak-gain variation is not highly sensitive to the separation distance between the antennas. Figure 3.17 and the Figure 3.18 show a very small frequency shift in the measurement results compared to the simulations. This is mainly because of the imperfections in the fabrication process and also the tolerance of the lumped-element loads used in the assistive antennas and matching network of the driver antenna. The information regarding variation of the peak-gain over the S_{11} bandwidth associated with each separation distance is given in Table 3.3. It is important to mention that the proposed fragmented coupled antenna not only enhances the bandwidth but also provides a higher peak-gain (around 1 dB) compared to the single-element antenna. The measured radiation efficiencies for $d = 12, 14, 16 \text{ cm}$ are also found to be 86.4%, 88.2%, and 80.4%,

Table 3.3. Simulated and Measured Peak-Gain Variations in Impedance Bandwidth.

Antenna Configuration	Simulation Results	Measurement Results
Single Antenna	1.26 dB -1.64 dB	0.56 dB- 0.97 dB
Coupled Antennas ($d= 12\text{cm}$)	1.36 dB- 2.54 dB	0.1 dB- 1.94 dB
Coupled Antennas ($d= 14\text{cm}$)	1.34 dB- 2.78 dB	0.8 dB- 2.1 dB
Coupled Antennas ($d= 16\text{cm}$)	1.34 dB- 2.69 dB	0.2 dB- 1.8 dB

respectively. These smaller values for the measured radiation efficiencies compared to the simulated ones (97%) can be attributed to the insertion loss of the Balun transformer. Finally, the radiation pattern in the E-plane ($x-y$ plane) and the H-plane ($y-z$ plane) are measured for all the separation distances at the beginning, middle and the end of the achieved frequency band (234 MHz, 240 MHz, 246 MHz) shown in Figure 3.19. The radiation patterns resemble that of a dipole antenna with higher directivity.

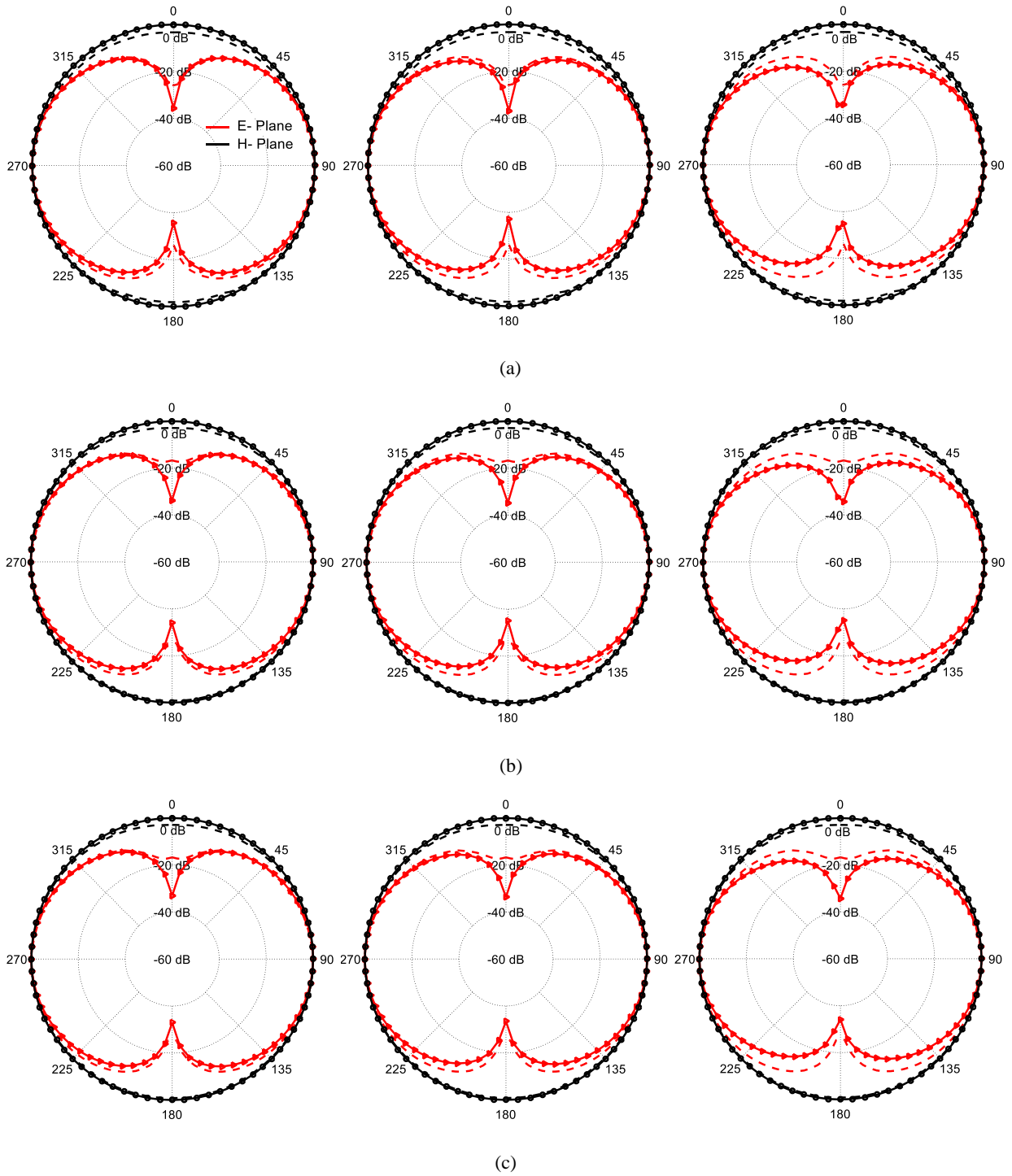


Figure 3.19. Measured and simulated radiation pattern in E-plane (red) and H-plane (black) for three different frequencies (from left to right: 234 MHz, 240 MHz, 246 MHz) over the achieved frequency bandwidth (a): $d=12$ cm, (b): $d=14$ cm, (c): $d=16$ cm. The solid lines are simulations and the dashed lines are measurements.

3.4. Conclusion

In this chapter, the concept of fragmented coupled antenna for achieving high bandwidth and high gain radiating structure from an ensemble of very small elements on small moving platforms is presented. To enable isolated platform operating, a miniaturized folded dipole antenna with inductive end-loads is designed. The provision of the inductive end-loads is to enable electromagnetic coupling of three or more of such antennas carried out by separate flyers. To achieve high radiation efficiency, the middle antenna (driver antenna) is excited and the two adjacent antennas (assistive) are terminated with lumped-element load. An optimization is carried on the load configuration to achieve considerable bandwidth enhancement and high radiation efficiency. Measurement results demonstrate that for a separation distance between three of such antennas, equal to the length of each antenna (12 cm), the proposed configuration provides 7.7 times larger bandwidth (7.7%) than the bandwidth of the isolated antenna and results in an average radiation efficiency of above 86.4%. The coupled triple antenna configuration also shows 1 dB improvement in the peak-gain compared to the single element antenna. As the separation distance between the antennas increases, the bandwidth enhancement decreases. Effect of flight instabilities on the coupled array antennas is also investigated and a tunable matching circuit using varactor diode is proposed so that the source can deliver maximum power to the antenna in all conditions.

CHAPTER 4

Electromagnetic-based Communication among Biological Cells

4.1. Introduction

For a long time, there has been a hypothesis saying that biological organisms ranging from bacteria and microbes to birds take the advantage of electromagnetic signals to communicate with each other and their surrounding environment [2]. There are experimental evidences as well indicating interaction of electromagnetic waves with bacteria and microbes [116]. Electromagnetic signaling within bacterial communities (biofilms) may take place at the speed of light and hence can be very fast. Such communication should be more efficient than quorum sensing at which bacteria release chemical molecules or autoinducers to diffuse to the adjacent cells. This is because of the fact that diffusion of molecules within biofilm (composed of water) is too slow. To unravel the role of possible electromagnetic signaling and examine what kind of information is transferred between bacteria within a biofilm sample, the first step is to find the mechanism of this signaling and understand what the actual built-in antennas are within a biofilm sample. An electromagnetic-based model that would predict such communication must be postulated to find the frequency and power level of signal generated by cells. Once these quantities (amplitude and frequency) are certainly known after the modeling and measurements, biologists can further investigate to see what actual information is transferred between the cells through such signaling and then try to control physiological activities of biofilms to treat related diseases efficiently.

To date, a few number of theoretical and experimental studies show some bacterial DNA sequences, microtubules, and protein chains induce electromagnetic (EM) waves at $\sim kHz$, $\sim GHz$, and $\sim THz$ frequency ranges, respectively [45]-[50]. Based on these observations, there is a growing interest to investigate a possibility that bacteria in biofilms can also transmit/receive EM waves as a means of communication [2], [3], [51]. Profound investigation and multiphysics modeling are initially required to unravel this phenomena and understand how community of biological cells in a biofilm can communicate through EM waves. Then, as there is no compelling experimental evidence for this conjecture, as a theoretical context for this field, we need to develop comparisons between the EM signaling and QS to unravel why and how EM signaling could be potentially advantageous.

Figure 4.1(a) illustrates scanning electron micrograph of a biofilm sample associated with the *Staphylococcus aureus* (*S. aureus*). Cells in a biofilm live in an extracellular matrix of hydrated polymeric substances (EPS) [57]. The major matrix components are polysaccharides, lipids, DNA segments and proteins some of which can form amyloid fibers. The EPS matrix provides mechanical stability for biofilms, mediates their adhesion to surfaces and interconnects biofilm cells through formation of a three-dimensional polymer network. In addition, the biofilm matrix acts as an external digestive system by keeping extracellular enzymes close to the cells, enabling them to metabolize dissolved, colloidal and solid biopolymers [117]. Within the EPS matrix of specific types of bacterial biofilms (e.g., *S. aureus*, and *Bacillus subtilis*), there are biological elements called amyloid fibrils which are basically characterized as elastic helical fibers with permanent dipole charges at their ends [118]-[120] (Figure 4.1(b)). The amyloid fibrils are in fact different conformational states of peptides and proteins [121], [122]. For instance, in *S. aureus* biofilms, their amyloid fibrils are basically aggregation of phenol-soluble modulins peptides

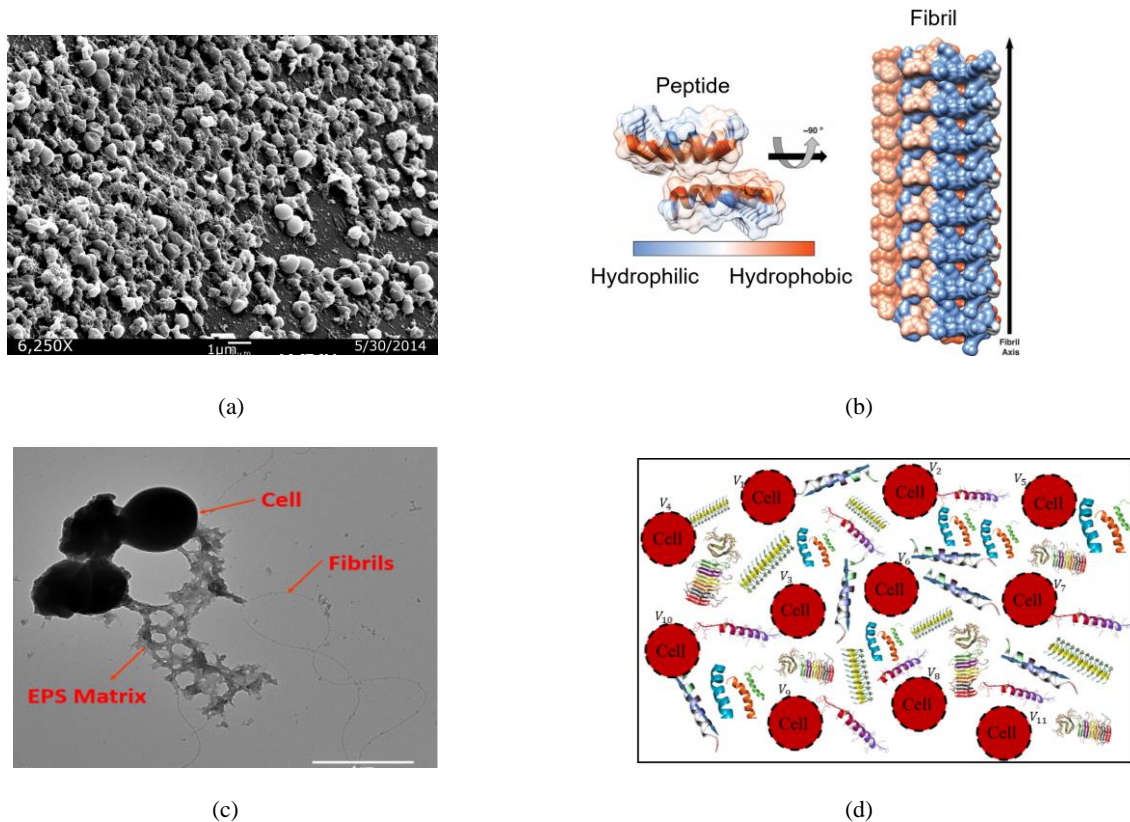


Figure 4.1. (a) SEM image of *Staphylococcus aureus* biofilm [126]. (b) Formation of amyloid fibrils as a result of charged peptides aggregation through hydrophobic and hydrophilic forces. The amyloid fibril will have a net dipole moment [127]. (c) Amyloid fibrils in composition with the extracellular matrix attached to the cell membrane (TEM image) [125]. The scale bar is 1 μm . (d) A 2D illustration of a biofilm with elastic amyloid fibrils (helical strings) playing the role of natural built-in antennas. The cells are represented by circles.

(PSM α , PSM β , etc.) [123]. The self-assembly process of PSMs into amyloid-like fibers involves backbone hydrogen bonding and side-chain interaction (e.g., hydrophobic interaction, π -stacking, and van der Waals attraction) [124], [125]. As can be observed from Figure 4.1(c) and also illustrated in Figure 4.1(d), the fibrils are all either suspended within the water background of the biofilm or attached to a cell membrane. The fibrils can vibrate due to internal metabolic processes, or undergoing external stresses to radiate EM waves (the concept of Mechanical Antennas). Thus, charged amyloid fibrils might play the role of mechanical antennas for their corresponding cells within biofilms. The frequency of communication is then governed by the mechanical properties of cells and the amyloid fibrils (modulus of elasticity, mass density, surface charge density, etc).

In this chapter, different vibrational modes for charged amyloid fibrils, called spring mode and cantilever mode, are explored. Fundamentally, accelerating charges can radiate electromagnetic fields, hence vibrating charged fibrils will act as the source and the antenna for cells in biofilms. A model based on electromagnetically-coupled system of mechanical oscillators is developed to evaluate the characteristics of this EM signal generated among the cells in a biofilm. Different mechanisms that lead to EM signal emission within kHz-GHz frequency range is demonstrated. For purposeful EM communication among cells, such vibration must be initiated by the cell itself. Using COMSOL Multiphysics simulation tool, it is shown that cell's sudden deformation caused by the release of accumulated stress or metabolic energy, can excite internal resonant vibration which in-turn couple to its attached amyloid fibrils. Such motions and the generated EM waves that can exert force on the charges of adjacent amyloid fibrils or other charges within the adjacent cells can be considered as purposeful signaling.

4.2. Source of EM Signal Emission in Biofilms

Amyloid fibrils in some specific biofilms such as *S. aureus* biofilm contain permanent dipole moment mainly oriented along their formation axis [119]. Amyloid fibrils are also characterized as elastic helical strings or beams [120]. The amyloid fibrils are either suspended within the liquid medium of the biofilm or hinged to the cells (see Figure 4.1(c)). These elastic charged strings can be then set in vibration by either the EPS matrix itself or cell through a sudden motion generated from metabolic processes or accumulated stress. Any vibrating (accelerating) charge radiates electromagnetic waves at frequencies related to the charge's motion which relates to the natural mechanical resonances of the structure. Therefore, charged amyloid fibrils play the

Table 4.1. Structural Mechanics Properties of the Cells and Amyloid Fibrils.

Component/Parameter	Mass density (ρ)	Young Modulus (E)	Bending Rigidity (EI)
Cell	1000 kg/m ³ [131]	200 MPa [129]	N.A
Amyloid Fibril	46.2 kDa/nm [132]	5-50 GPa [120]	$EI = 0.8 \times 10^{-26} N.m^2$ [120]

role of mechanical antennas within biofilms [22]. Due to the small dimensions of cells and amyloids, the fields generated by such motions are expected to fall within radio frequencies.

4.2.1. Structural Mechanics Analysis of Single Amyloid Fibril and Cells.

In order to conceptually understand how motion of amyloid fibrils looks like and find possible natural resonant frequencies, we first performed a solid mechanics modal analysis on amyloid fibrils that are attached to a cell. In this analysis COMSOL Multiphysics simulation tool is used and the results are shown in Figure 4.2. Here, the cell is modeled as a solid sphere ($R = 440 \text{ nm}$) with Young modulus $E = 200 \text{ Mpa}$, and mass density $\rho_{cell} = 1000 \text{ kg/m}^3$ [128]-[131]. The fibril is modeled as a solid beam with bending rigidity $EI = 0.8 \times 10^{-26} \text{ N.m}^2$ [120], and linear mass density $\rho' = 46.2 \text{ kDa/nm}$ [132]. These parameters are all summarized in Table 4.1. The amyloid fibril is $1 \mu\text{m}$ in length (l) and 10 nm in width. In general, the fibril length can vary from $0.1 \mu\text{m}$ to $6 \mu\text{m}$ [133]. Simulation results show that due to the flexibility of fibrils compared with the cell, at low frequencies, while the cell is stationary, they mainly undergo cantilever beam vibrational modes with multiple nodes depending on the mode of vibration. But, at higher frequencies, the higher order modes of cantilever beam couples to the cell's vibrational modes and a complex (combined) mode of vibration will form from the cell plus its amyloid fibril (see Figure 4.2(b)). We will discuss these complex modes in more details later when purposeful

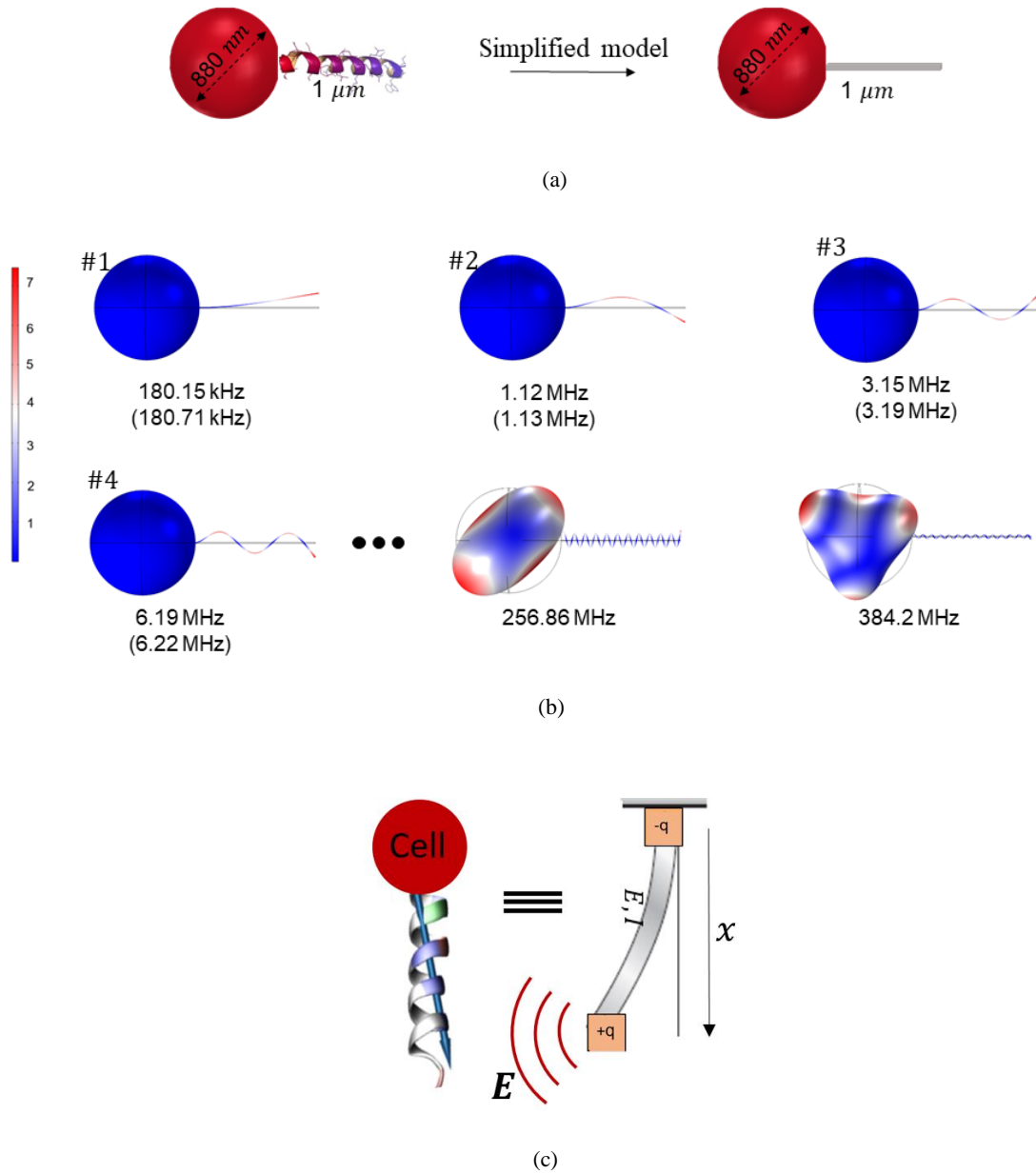


Figure 4.2. (a): A bacterial cell and its attached amyloid fibril are modeled as a solid sphere and a beam for modal analysis. (b): Structural mechanics modal analysis on the amyloid fibril and cell. At low-frequencies, cantilever beam vibrational modes are observed for the fibrils within the kHz-MHz range. At higher frequencies, the cell's vibrational modes will combine with the higher order modes of the cantilever beam associated with the fibril and then complex mode configurations appear. The given resonant frequencies in the parenthesis are the ones obtained from the analytical solution which are in agreement with COMSOL FEM simulation. (c): Attached amyloid fibril to a cell can be treated as a cantilever beam having dipole charges at its ends.

communication is discussed. For a fibril with the above mentioned physical and mechanical properties, the natural resonant frequencies of its cantilever beam modes are [134],

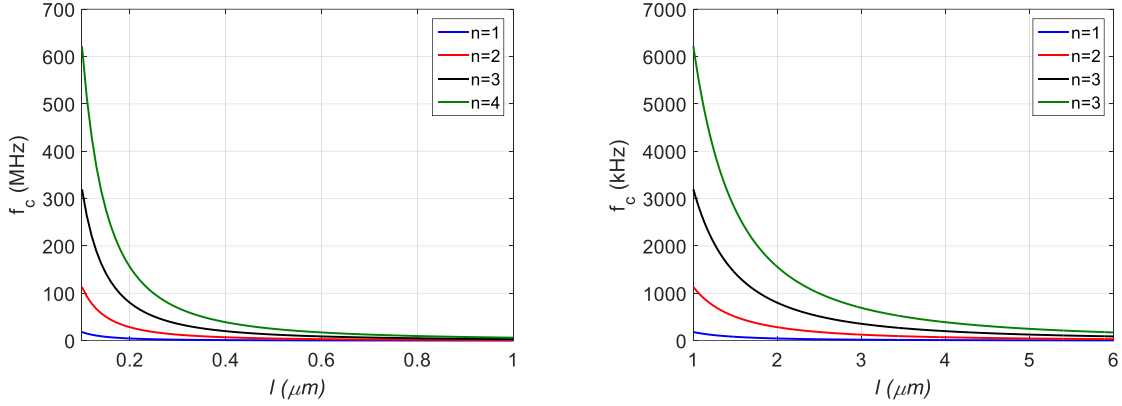


Figure 4.3. Resonant frequency of amyloid fibril cantilever beam mode as a function of length for its first four modes. To have better understanding of resonant frequency values, the plot is divided into two separate plots with different length ranges.

$$f_{c_n} = \alpha_n^2 \sqrt{\frac{EI}{\rho' l^4}} \quad (4.1)$$

where $\alpha_n = 1.875, 4.694, 7.885, 11$ are constants associated with the first four modes. As indicated in Eq. (4.1), the resonant frequencies are inversely proportional to the square of length. Figure 4.3 depicts the resonant frequency of an amyloid fibril versus its length for its first four modes. In very close agreement with these theoretical values, simulations also predict that the resonant frequencies fall within the $kHz - MHz$ range. Therefore, such amyloid fibrils can be treated as low-frequency charged cantilever beams (Figure 4.2(c)). It should be noted that the vibration frequencies are in fact, the possible frequency of EM signaling within the biofilm. Whenever charged amyloid fibrils are set in motion (vibration) by means of either the cell or the EPS matrix, their dipole charges radiate EM waves according to one the fundamental theories in electromagnetics.

For those elastic amyloid fibrils which are floating and not attached to any cells, they act as mechanical distributed spring-mass oscillators with permanent dipole charges as shown in Figure 4.4. Since the dipole moment is not necessarily along the fibril axis, two spring modes can

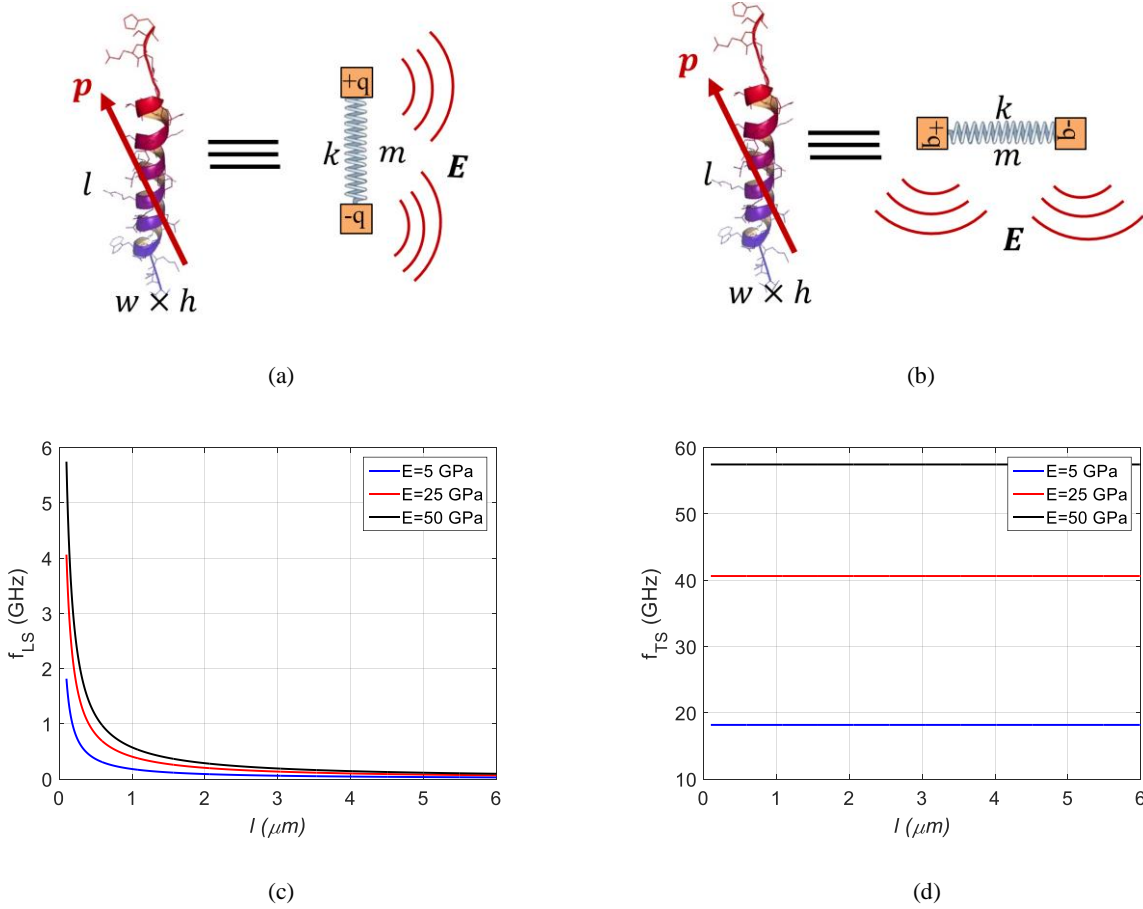


Figure 4.4. (a): An elastic amyloid fibril connected to the EPS matrix and not attached to any cells can be modeled as a charged spring (longitudinal mode). (b): Transverse spring mode for the floating fibrils. (c): Amyloid fibril natural resonant frequency for spring vibrational mode (longitudinal vibration) as a function of length. (d): Amyloid resonant frequency for transverse spring vibration.

be considered namely, longitudinal spring mode and transverse spring mode as illustrated in Figure 4.4(a) and Figure 4.4(b), respectively. Considering an elastic amyloid fibril (modulus of elasticity, $E \sim 5-50$ Gpa [120], [135]) with length l , cross-section A (width (w) ~ 10 nm, height (h) ~ 2 nm) [136] and distributed mass $m (= \rho'l)$, its resonant frequency can be calculated approximately as,

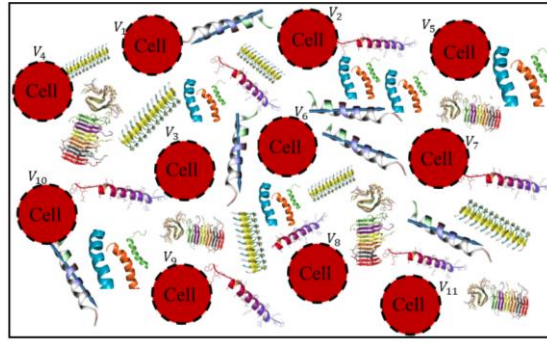
$$f_{LS} \sim \frac{1}{2\pi} \sqrt{\frac{K}{m}} = \frac{1}{2\pi} \sqrt{\frac{EA}{ml}} = \frac{1}{2\pi} \sqrt{\frac{E \times (w \times h)}{\rho'l^2}}, \quad f_{TS} \sim \frac{1}{2\pi} \sqrt{\frac{K}{m}} = \frac{1}{2\pi} \sqrt{\frac{E \times (l \times h)}{\rho'l \times w}} \quad (4.2)$$

Here, f_{LS} and f_{TS} are the natural resonant frequencies of longitudinal and transverse spring modes,

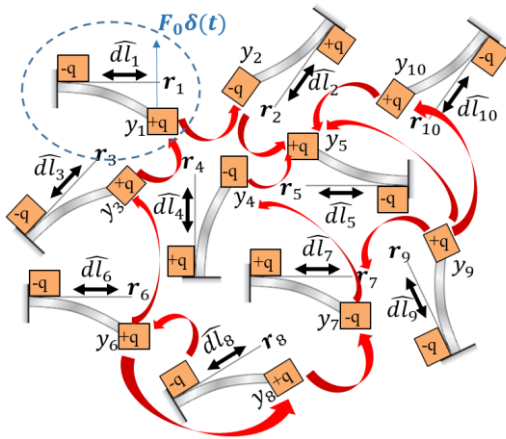
respectively. K is the effective spring constant of fibrils for each mode. Figure 4.4(c) and Figure 4.4(d) show the resonant frequency of spring vibration mode as a function of amyloid length assuming the above mentioned mechanical properties. From this figure, one can readily conclude that such mode of vibration can potentially induce EM fields mainly within gigahertz frequency range (0.1-50 GHz). It should be noted that for this mode of vibration, the motion of opposite charges associated with each fibril are out of phase and thus their emitting EM fields would be in-phase.

4.2.2. Amyloid Fibrils Community as EM-Coupled Mechanical Oscillators.

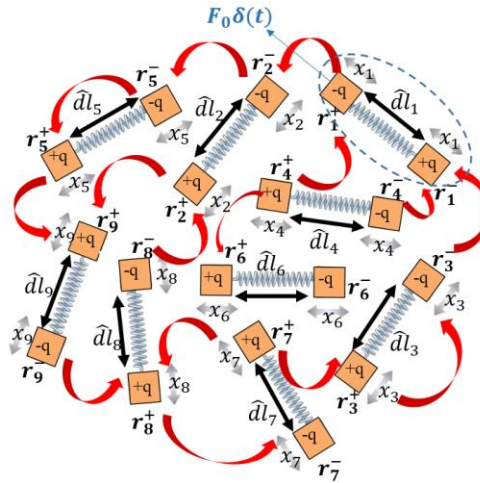
Within a small volume of biofilms, there may be up to millions of amyloid fibrils with various lengths. Based on what explained and also illustrated in Figure 4.5, this would create a system of electromagnetically-coupled mechanical oscillators. In fact, the vibrating charges provide EM coupling between adjacent elastic fibrils treated as mechanical oscillators. Since strong EM coupling can potentially exist between fibrils, the vibration frequencies of individual fibrils are not necessarily the vibration frequencies of the isolated fibrils due to the frequency bifurcation phenomena observed in coupled resonator systems. The following subsection provides the detailed analysis of electromechanical coupled system and describes the method for the calculation of the resonant frequencies. In summary, this analysis indicates that for the spring mode, EM interactions relative to the stiffness of fibrils are not strong enough to provide coupling and synchronization between the adjacent fibrils. Therefore, the vibration frequencies of coupled fibrils will be mainly the same as the individual's frequencies. However, for the cantilever beam mode, strong coupling exists relative to the equivalent stiffness for this mode and the natural vibration frequencies of fibrils community mainly occurs in the kHz-MHz frequency range with



(a)



(b)



(c)

Figure 4.5. (a): Illustration of a biofilm including cells and amyloid fibrils. (b): EM-coupled system of mechanical oscillators representing interacting amyloid fibrils in a biofilm (cantilever beam mode). (c): Coupled spring vibrational mode for fibrils in biofilms. The arrows indicate the electromagnetic coupling existing between the charges of fibrils.

strong synchronization. It should also be stated that as the frequency of spring mode (GHz) and cantilever beam mode (kHz-MHz) are far apart from each other, these vibrational modes are decoupled.

4.2.3. Mathematical Analysis of EM-coupled Mechanical Oscillators

In order to clarify the role of EM coupling among fibrils and understand how vibration of one fibril gets affected by the adjacent fibrils, according to Figure 4.5(b) or Figure 4.5(c), one of the fibrils is assumed to be initially disturbed from its resting positions, due to some metabolic

changes or activities in a cell, and go into motion. Then, due to EM coupling other fibrils can also potentially go to motion and transfer the message in the medium. To examine this scenario, the Lagrangian technique which is the resultant of Hamilton's principle is applied to the constituents in the medium. For a single cantilever beam with length l the equation of motion can be calculated analytically. Considering its first mode of vibration, the vibration amplitude distribution along the beam is,

$$w(x, t) = \left(1 - \cos\left(\frac{\pi}{2l}x\right)\right)y(t) \quad (4.3)$$

here, as defined in Figure 4.2(c), x is the representation of coordinate system along the beam and $y(t)$ takes into account the temporal behavior of transverse vibration which can be for example proportional to $\cos(\omega t)$ for an oscillatory case. The stored kinetic energy (T) and the stored strain energy (U) in the cantilever beam can be obtained from [137],

$$T = \frac{1}{2}\rho A \int_0^L \dot{w}^2 dx = \frac{1}{2}\rho' A \left(\frac{3\pi - 8}{2\pi}\right) l \dot{y}^2 \quad (4.4)$$

$$U = \frac{1}{2}EI \int_0^L w''^2 dx = \frac{1}{2}EI \left(\frac{\pi}{2L}\right)^4 Ly^2 \quad (4.5)$$

where EI is the bending rigidity of the beam (fibril), l is the length, ρ is the volumetric mass density ($\rho' = \rho A$) and A is the beam's cross section. \dot{w} is the time-derivative of $w(x, t)$ and w'' is the second derivative of $w(x, t)$ with respect to x .

Now, back to our original problem with many anchored fibrils (Figure 4.5(b)), defining the orientation of each fibril at its rest as $\hat{d}l_i$, and the amplitude of transverse oscillation of its open end as y_i , and considering the first mode of cantilever beam for each fibril, the Lagrangian of the system (N fibrils) can be written as [138],

$$L = T - U - U_{EM}$$

$$= c_{hdy} \times \frac{1}{2} \sum_{i=1}^N \rho_i A_i \left(\frac{3\pi - 8}{2\pi} \right) l_i \dot{y}_i^2 - \frac{1}{4} \sum_{i=1}^N E_i I_i \left(\frac{\pi}{2l_i} \right)^4 l_i y_i^2 - \sum_{i=1}^N \sum_{\substack{j=1 \\ j \neq i}}^N \kappa_{ij} y_i y_j \quad (4.6)$$

where, the first term accounts for the stored kinetic energy of the system, the second term includes the stored potential energy in the system and the third term which is the key element in describing electromagnetic-based communication, represents the dipole-dipole interaction of adjacent fibrils (electromagnetic potential energy, U_{EM}). As the induced EM signal wavelength ($kHz - GHz$) is considerably longer than typical dimensions within a biofilm ($nm - \mu m$), κ_{ij} can be found using quasi-static approximations [79],

$$\kappa_{ij} \triangleq \frac{1}{2} \frac{q_i q_j}{4\pi\epsilon_0} \frac{1}{|\mathbf{r}_i - \mathbf{r}_j|^3} \left\{ \hat{d}l_i^\perp \cdot \hat{d}l_j^\perp - \frac{3(\mathbf{r}_i - \mathbf{r}_j) \cdot \hat{d}l_j^\perp}{|\mathbf{r}_i - \mathbf{r}_j|^2} (\mathbf{r}_i - \mathbf{r}_j) \cdot \hat{d}l_i^\perp \right\} \quad (4.7)$$

q_i is the charge of the dipole associated with each fibril, \mathbf{r}_i is the stationary position of the i^{th} fibril's open end and $\hat{d}l_i^\perp$ is a unit vector perpendicular to $\hat{d}l_i$. The correction coefficient c_{hdy} behind the first term of Eq. (4.6) takes into account the hydrodynamic loading of water around the beam and is simply given as [139],

$$c_{hdy} = 1 + \frac{\pi \rho_{water}}{4 \rho_{beam}} \quad (4.8)$$

Applying the Lagrange equation [138],

$$\frac{d}{dt} \left(\frac{\partial L}{\partial \dot{y}_i} \right) - \frac{\partial L}{\partial y_i} = F_i^d + F_i^e \quad i = 1, 2, 3, \dots, N \quad (4.9)$$

We will end up having N independent equations. Here, F_i^d , and F_i^e account for the damping force (cantilever beam vibration in water as a viscous medium) and other external non-conservative

forces, respectively. By solving the abovementioned N equations for the steady state condition, one can obtain all the possible resonant frequencies and amplitudes of oscillation of the fibrils in the medium. These equations in the frequency domain can be re-arranged in the form of a generalized eigenvalue-eigenfunction problem,

$$\left(-\omega^2 \overline{\overline{M}} + i\omega \overline{\overline{F}}_d + \overline{\overline{K}}\right) \overline{Y} = F_0 \begin{pmatrix} 0 \\ 0 \\ \vdots \\ 1 \\ 0 \\ 0 \end{pmatrix} \quad (4.10)$$

where ω is the natural resonant frequency of the system, and Y is an $N \times 1$ vector representing the amplitude of oscillation of the fibrils at that frequency. The index 1 on the right-hand side (excitation vector) corresponds to one initially-disturbed fibril. Defining Q_i as the quality factor for the vibration of the i^{th} fibril in water, and s_i and m_i as,

$$s_i = \frac{1}{2} E_i I_i \left(\frac{\pi}{2L_i}\right)^4 L_i, \quad m_i = c_{hdy} \times \rho_i A_i \left(\frac{3\pi - 8}{2\pi}\right) L_i \quad (4.11)$$

The $N \times N$ matrices $\overline{\overline{K}}$ (equivalent spring constant), $\overline{\overline{M}}$ (equivalent mass), and $\overline{\overline{F}}_d$ (equivalent damping) [140] in Eq. (4.10), can be written as,

$$\begin{aligned} K_{ii} &= s_i, \quad K_{ij} = 2\kappa_{ij} \quad (i \neq j) \\ M_{ii} &= m_i, \quad M_{ij} = 0 \quad (i \neq j) \\ F_{dii} &= \frac{\sqrt{s_i m_i}}{Q_i}, \quad F_{dij} = 0 \quad (i \neq j) \end{aligned} \quad (4.12)$$

As can be seen, the non-diagonal elements of the matrix $\overline{\overline{K}}$ represent the electromagnetic coupling between the fibrils. Mathematically speaking, these non-diagonal elements are in fact representing the communication among adjacent fibrils. As will be discussed later, the ratio of non-diagonal elements to the diagonal elements (κ_{ij}/s_i) is critical in establishing synchronized vibration among

fibrils. By synchronization, we just mean that the amplitude level of fibrils displacement are a noticeable fraction of the oscillation amplitude of that initially disturbed fibril.

All the possible resonant frequencies of the system (frequencies of EM-based communication) are the solution of following equation,

$$\left| \bar{K} - \omega_i^2 \bar{M} + i\omega_i \bar{F}_d \right| = 0 \quad (4.13)$$

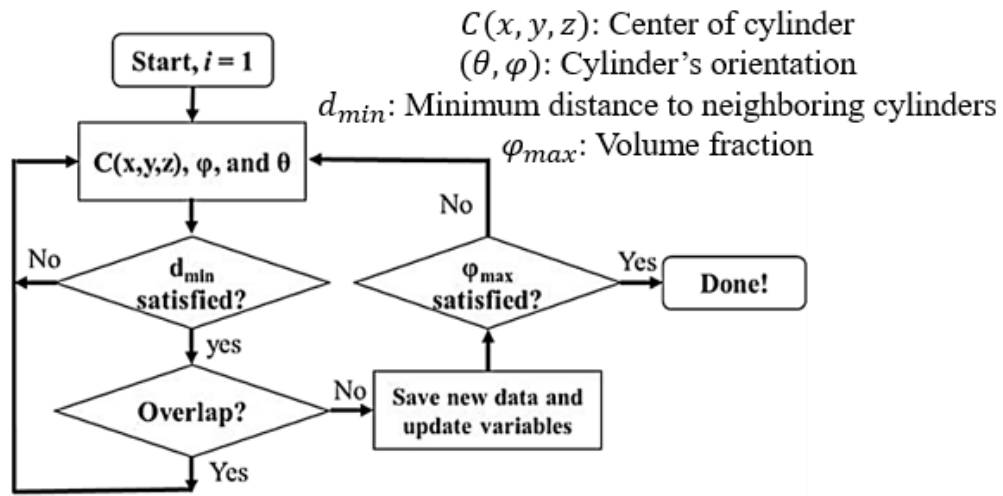
The corresponding amplitude of oscillation for all the fibrils associated at each eigenfrequency ($\omega_{ri} = Re\{\omega_i\}$) is also given by,

$$\bar{Y}_i = (\bar{K} - \omega_{ri}^2 \bar{M} + i\omega_{ri} \bar{F}_d)^{-1} \begin{pmatrix} 0 \\ 0 \\ \vdots \\ 1 \\ 0 \\ 0 \end{pmatrix} F_0 \quad (4.14)$$

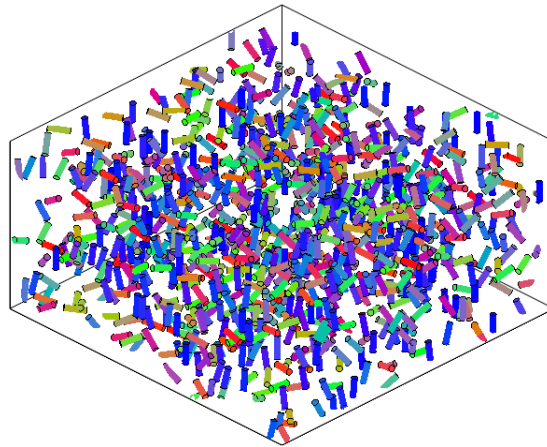
The more non-zero elements the vector \bar{Y}_i contains, the stronger is synchronization among the cells at that frequency which is determined by the strength of κ_{ij}/S_i .

4.2.4. Possible EM-based Communication Frequencies and Synchronization Level.

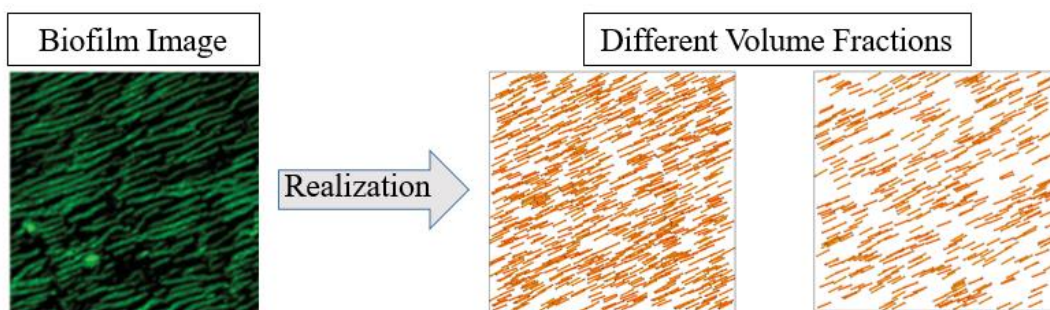
For simple demonstration of the concept and capability of our proposed approach, we have first used a packing algorithm illustrated in Figure 4.6 [141]. At every iteration, the algorithm generates a cylinder with prescribed cross section, random location, and random length (within the limits defined for its length and bounding box) and evaluate to find if it intersects with other previously generated cylinders or not. If it intersects, the algorithm removes this cylinder and generates a new one. If not, it continues and generate other cylinders until the whole volume of all cylinders reaches the desired volume fraction (φ_{max}). For our problem here, we have generated 2000 non-intersecting fibril. The fibrils are generated such that they are all confined within a box



(a)



(b)



(c)

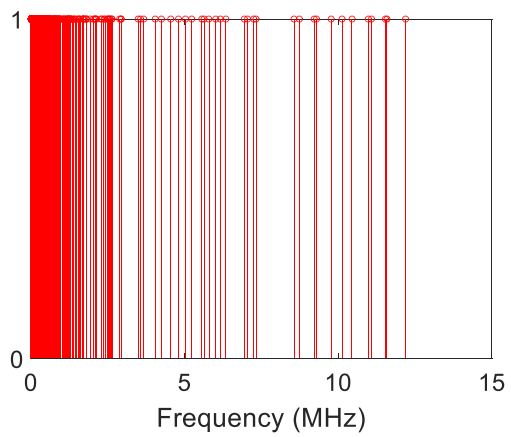
Figure 4.6. (a): The developed flowchart for generating non-intersecting fibrils (cylinders) inside a box. (b): One 3D realization for the developed algorithm. (c): Realization of a biofilm image with different volume fractions (φ_{max}).

with dimensions $8 \times 8 \times 4 \mu m$ ($\sim 0.3\%$ volume fraction) to represent a biofilm sample. Fibrils length

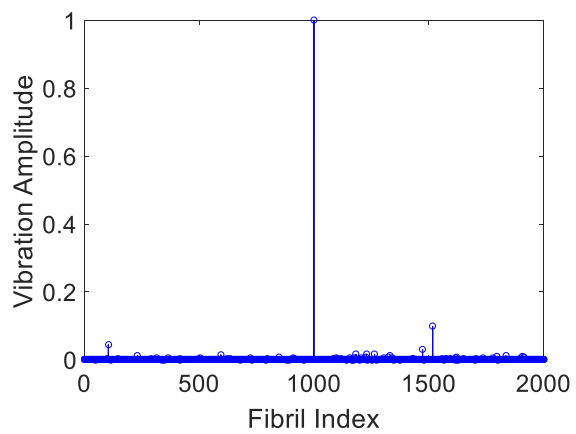
distribution is considered to be uniform, $L \sim U(0.1, 6) \mu m$. Using those previously used values of the mass density (ρ), cross section (A) and bending rigidity (EI), and setting fibrils dipole charges $q = \pm 3e^-$ (e^- is the electron charge value) [119], Eq. (4.13) and Eq. (4.14) are solved for the resonant frequency (communication frequency) as well as the vibration amplitude of all fibrils in response to one initially-disturbed fibril. The quality factor for a cantilever beam vibrating in water (biofilm background medium) is set to be $Q \sim 4$ (see Appendix B). Figure 4.7(a) illustrates the resulted frequency spectrum. As can be seen, based on the cantilever beam vibrational mode, staphylococcus aureus cells that are used in this simulation can potentially use electromagnetic signals within the $kHz - MHz$ range. This potential spectrum depends on the modeling parameters and is not unique. As there are many uncertainties in experimental values for these parameters, the spectrum can slightly shift up or down. Also it is noted that in this simulation, we have only considered the fundamental mode. Considering higher order modes of cantilever beam, frequency spectrum also shifts upward. The relative amplitude of oscillation of fibrils at two of the fundamental mode's resonant frequencies 13.6 kHz , and 3.3 kHz is calculated and shown in Figure 4.7(b) and Figure 4.7(c), respectively. Here, all the amplitudes are normalized to the amplitude of the fibril having maximum oscillation level. It is obvious that in response to the initial vibration of one fibril, other fibrils start vibrating by the transferred electromagnetic signal. The synchronized motion with large amplitudes happens only at subset of all possible resonant frequencies. It should be noted that the level of synchronization decreases as the resonant frequency increases. This is due to the fact that the cantilever beams vibrating at higher frequencies are stiffer and the EM field is not strong enough to exert force on the fibrils. Since there are uncertainties on the reported values for the fibrils dipole moment (charges), another simulation considering stronger dipole charges ($q = \pm 15e^-$) is carried out and the result is shown in

Figure 4.8(a), Figure 4.8(b) and Figure 4.8(c) depict the relative amplitudes of vibration at 8 *kHz* and 27.6 *kHz*, respectively. It is shown that stronger dipole moment enhances the electromagnetic coupling which in turn will increase the synchronization level between the fibrils. Additionally, as the electromagnetic force becomes stronger, the resonant frequencies with high synchronization level potentially shift upward. The impact of quality factor on the synchronization and frequency spectrum was also investigated by considering, for instance a lower quality factor value ($Q = 2$) for the fibrils' vibration. It can be observed from Figure 4.9 that the frequency spectrum slightly changes and synchronization level becomes smaller when the loss increases. This is somehow expected because oscillation amplitude of transmitting fibril gets attenuated quickly and then electromagnetic coupling strength reduces.

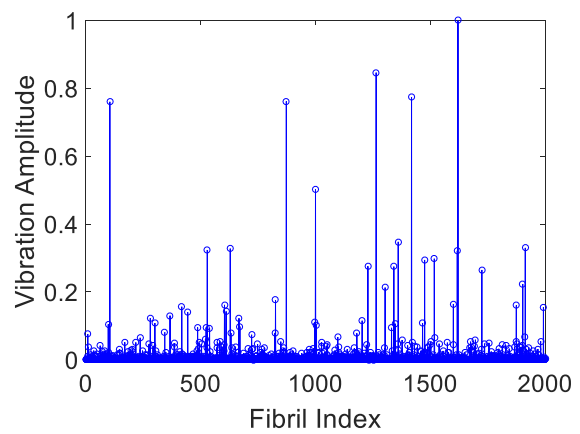
The same procedure was applied to study the spring vibrational mode [142]. The Young modulus for the spring mode is set to be 25 *GPa* [120]. Considering spring modes, the spectrum shifts to the gigahertz frequencies as shown in Figure 4.10(a), mainly because of larger stiffness compared to the cantilever mode. Because of this stiffness, fibrils cannot excite each other to have synchronization (Figure 4.10(b), and Figure 4.10(c)). In other words, the EM field does produce not enough energy to cause the amyloid fibrils move longitudinally at GHz frequencies. This is evident mathematically by examining the ratio of the non-diagonal to the diagonal elements of matrix $\bar{\bar{K}}$ (κ_{ij}/s_i). For the spring mode, this ratio is about 10^{-14} - 10^{-12} meaning that the matrix $\bar{\bar{K}}$ is almost diagonal prohibiting interaction between the elements of vector \bar{Y}_l (see Eq. (4.10)). However, for the cantilever beam mode, this ratio falls within the range 10^{-4} - 10^{-2} and the interaction between fibrils is possible.



(a)

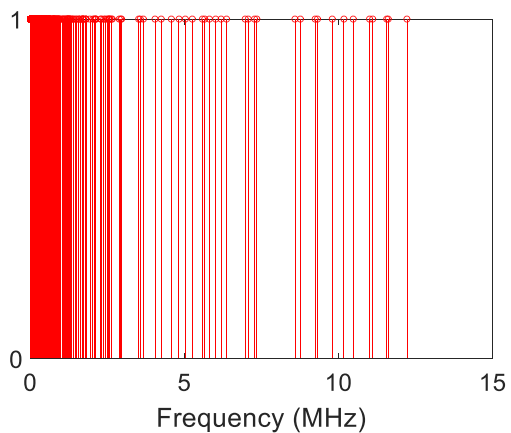


(b)

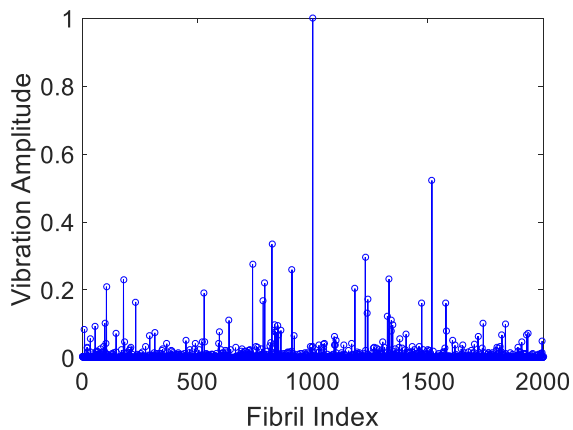


(c)

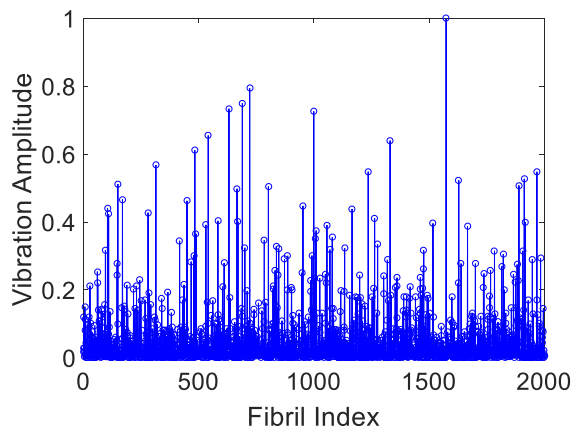
Figure 4.7. (a): Possible resonant frequencies of electromagnetically-coupled amyloid fibrils (cantilever beam mode, $q = \pm 3e^-$, $Q = 4$). (b): Relative amplitude of vibration of fibrils at one of those eignefrequencies (13.6 kHz). (c): Relative amplitude of oscillation of fibrils at 3.3 kHz .



(a)

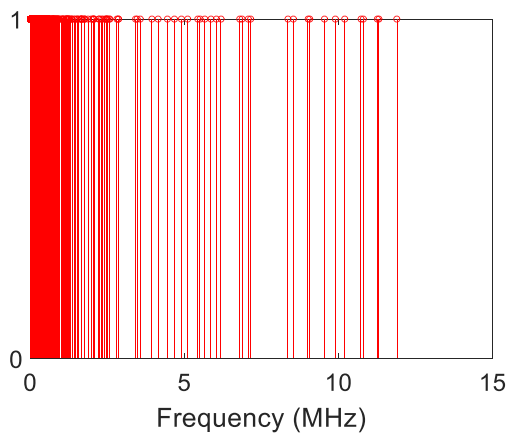


(b)

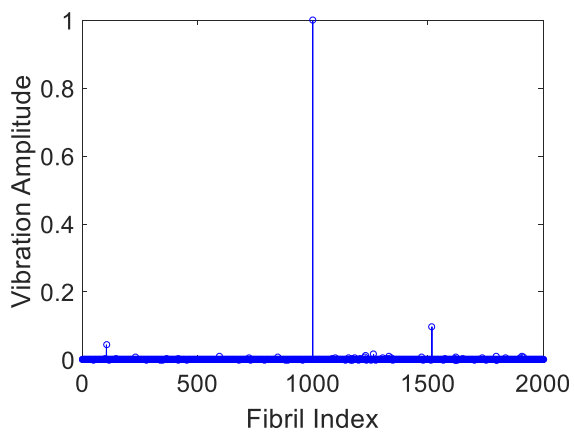


(c)

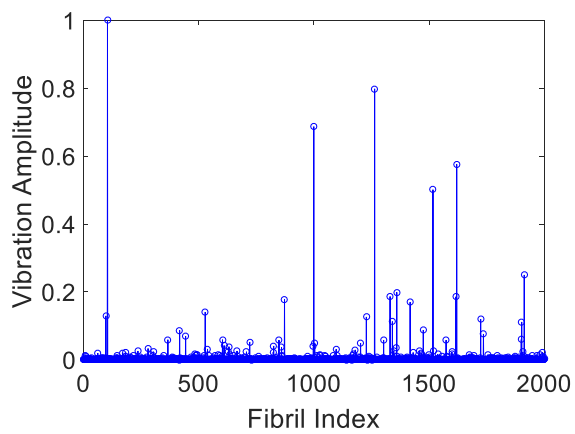
Figure 4.8. Impact of stronger dipole moment ($q = \pm 15e^-$, $Q = 4$) on the synchronization and natural resonant frequencies. (a): Frequency spectrum. (b): The relative amplitude of fibrils' vibration is plotted at 8 kHz. (c): The relative amplitude of fibrils' vibration at 27.6 kHz.



(a)

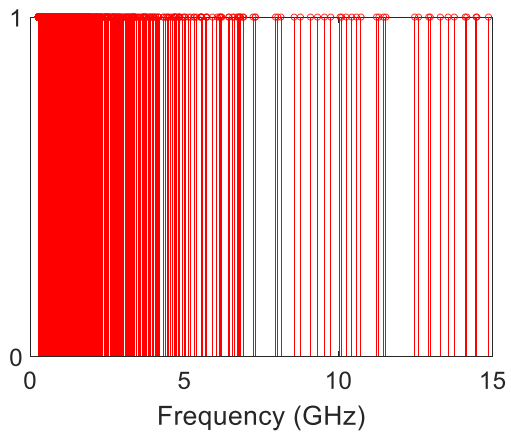


(b)

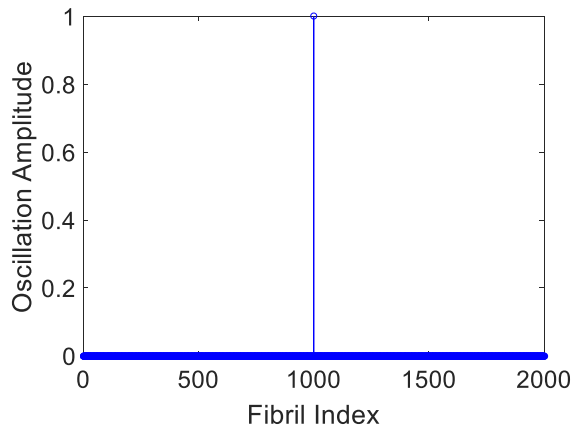


(c)

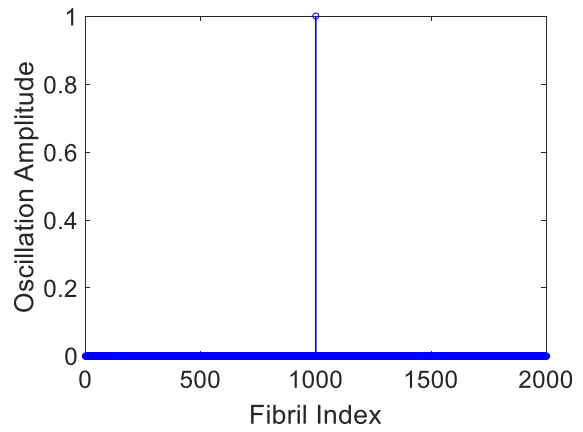
Figure 4.9. Impact of lower quality factor ($q = \pm 3e^-$, $Q = 2$) on the synchronization and natural resonant frequencies. (a): Frequency spectrum. The relative amplitude of fibrils' vibration are shown at (b): 3.4 kHz, and (c): 13.7 kHz.



(a)



(b)



(c)

Figure 4.10. (a): Possible resonant frequencies for the spring mode. (b): Relative amplitude of fibrils' oscillation for spring mode at 0.9 GHz. (c): Relative amplitude of fibrils oscillation for spring mode at 8.13 GHz. Only the initially-excited fibril vibrates and cannot couple to other fibrils.

4.3. Multiphysics Model of EM Communication within Biofilms

4.3.1. Purposeful EM Communication Hypothesis.

So far, our modeling has been only focused on the vibration of charged fibrils as the origination of EM waves in biofilm samples. For purposeful communication; however, this vibration must be initiated from the cell itself. Based on our hypothesis summarized in Figure 4.11, it is expected that once a transmitting cell sets an amyloid fibril to motion through resonant vibration, it provides EM signal transmission from that cell to its environment as well as its adjacent cells. For receiving mode, according to the reciprocity theorem, the transmitted signal will transfer the wave energy to mechanical energy by exerting force on the permanent dipole charges of other amyloid fibrils attached to the adjacent cells. In other words, the signal reception is accomplished in the reverse order, that is, the time-varying electric fields generated by cells exert force on the permanent charges on amyloid fibers connected to a receiving cell which is then sensed by the receiving cell. Through the Mechanotransduction process [143], [144], the cell senses this mechanical stimulus and will convert it into a biochemical, intracellular response.

As the cell-fibril modal analysis predicted before, the cell can also undergo a mechanical deformation along with its attached fibrils at higher frequencies. Shown in Figure 4.2, this deformation couples to the higher order cantilever modes of the amyloid fibril causing a high frequency oscillation. As a result of this, EM signal will be created at the frequency and harmonics of cell's resonant vibration frequencies. To find these possible resonant frequencies of the cell itself, a solid mechanics modal analysis is performed on an individual cell. As illustrated in Figure 4.12, the cell is modeled as a sphere ($R = 440 \text{ nm}$) with Young modulus $E = 200 \text{ Mpa}$, Poisson's ratio $\nu = 0.4$, and mass density $\rho_{cell} = 1000 \text{ kg/m}^3$ [128]-[131]. The natural spheroidal

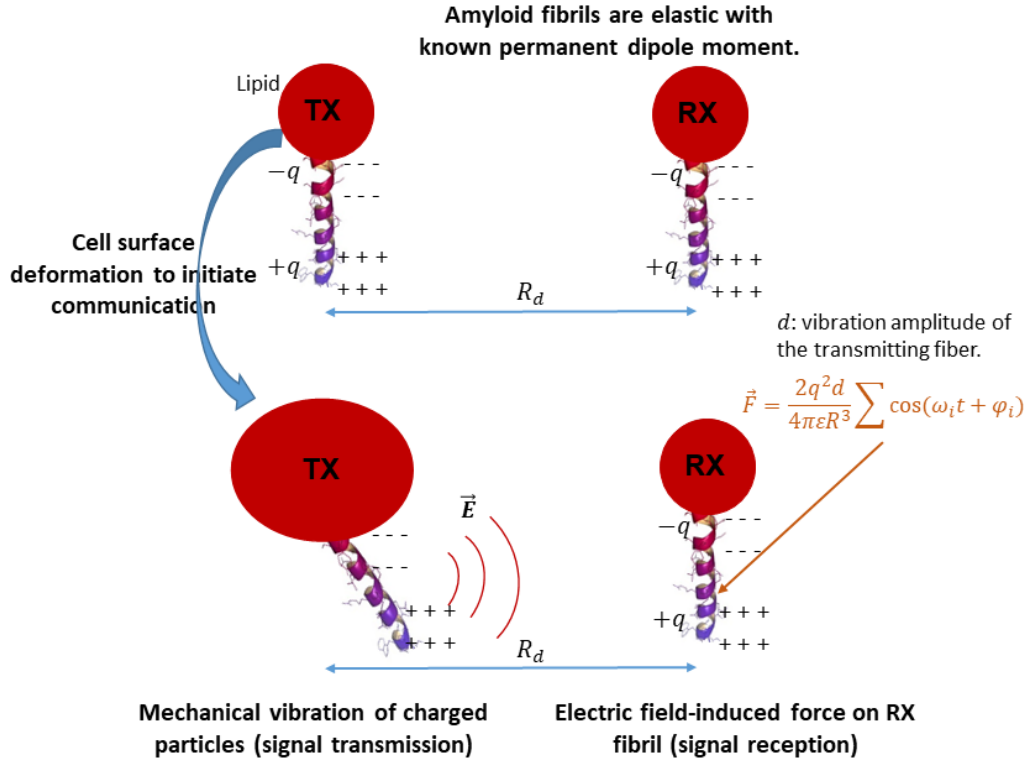


Figure 4.11. Our hypothesis for electromagnetic-based communication between two transmitting (TX) and receiving (RX) biological cells. The vibration of charged amyloid fibrils caused by the cell will induce EM radiation.

modes of the cell and corresponding resonant frequencies can be obtained through solving the Navier's wave equation [145],

$$(\lambda + 2\mu)\nabla(\nabla \cdot \vec{u}) - \mu\nabla \times (\nabla \times \vec{u}) = -\omega^2 \rho \vec{u} \quad (4.15)$$

here $u(r)$ is the radial displacement of every point within the cell, ω is the natural resonant frequency of the allowable mode, and λ and μ are the shear modulus and Lamé's first parameter, respectively, given as [145],

$$\mu = \frac{E}{2(1 + \nu)}, \quad \lambda = \frac{E\nu}{(1 + \nu)(1 - 2\nu)} \quad (4.16)$$

Similar to the TE and TM waves problems in electromagnetics [6], the spheroidal modes can be classified into two separate groups called, longitudinal (L) and transverse (T) vibration

modes. Hence the total displacement $u(r)$ can be written as [146],

$$\vec{u}(r) = \vec{u}_L + \vec{u}_T = \nabla\varphi + \nabla \times (\nabla \times (A\hat{r})) \quad (4.17)$$

where φ and $A\hat{r}$ are scalar and vector potential, each of which satisfies the wave equation as,

$$\nabla^2\varphi + k_L^2\varphi = 0 \quad (4.18)$$

$$\nabla^2(A\hat{r}) + k_T^2(A\hat{r}) = 0 \quad (4.19)$$

with

$$k_L = \frac{\omega}{c_L}, \quad c_L = \sqrt{\frac{\lambda + 2\mu}{\rho}} \quad (4.20)$$

$$k_T = \frac{\omega}{c_T}, \quad c_T = \sqrt{\frac{\mu}{\rho}} \quad (4.21)$$

Assuming a solid sphere model for the cell, its radial displacement can be then written as [146],

$$\vec{u}(r) = \vec{u}_L + \vec{u}_T = B\nabla(\hat{r}j_l(k_L r)p_l(\cos\theta)) + C\nabla \times \nabla \times (\hat{r}j_l(k_T r)p_l(\cos\theta)) \quad (4.22)$$

here, B and C are two constants. j_l and p_l are the spherical Bessel function of the order l and Legendre polynomial function of the order l , respectively. To find the natural resonant frequencies associated with each spheroidal mode, we have to first define the stress tensor (σ_{ij}) as,

$$\sigma_{ij} = \lambda\nabla \cdot \vec{u}\delta_{ij} + 2\mu\epsilon_{ij} \quad (4.23)$$

where δ_{ij} is the Kronecker Delta, and

$$\epsilon_{ij} = \frac{1}{2}\left(\frac{\partial u_i}{\partial x_j} + \frac{\partial u_j}{\partial x_i}\right) \quad (4.24)$$

By applying the stress-free boundary condition on the cell's membrane [146],

$$\sigma_{rr} = \sigma_{r\theta} = 0 \text{ (@ } r = R = 440 \text{ nm)} \quad (4.25)$$

After several algebraic steps, it can be shown that the natural resonant frequencies of vibration (ω) for $l > 0$ can be obtained from the following equation,

$$\Delta_l = \begin{vmatrix} T_{11} & T_{13} \\ T_{41} & T_{43} \end{vmatrix} = 0 \quad (4.26)$$

where,

$$\begin{cases} T_{11} = \left(l^2 - l - \frac{\eta^2}{2} \right) j_l(\xi) + 2 \xi j_{l+1}(\xi) \\ T_{13} = l(l+1) \{ (l-1) j_l(\eta) - \eta j_{l+1}(\eta) \} \\ T_{41} = (l-1) j_l(\xi) - \xi j_{l+1}(\xi) \\ T_{43} = \left(l^2 - 1 - \frac{\eta^2}{2} \right) j_l(\eta) + \eta j_{l+1}(\eta) \end{cases} \quad (4.27)$$

In the above equation $\eta = K_T R$ and $\xi = K_L R$.

Figure 4.12 depicts the first four spheroidal modes of the cell ($l = 1, 2, 3, 4$) given the above mentioned properties and size. As can be seen, the natural vibrational frequencies for a single cell are in the range of 200 MHz-1 GHz in agreement with recent experimental observations in the literature [131]. Additionally, the ellipsoidal mode (second mode) has the lowest possible frequency while the breathing mode (first mode) occurs at higher frequencies. Through numerical simulations using COMSOL Multiphysics, the modal analysis results are also verified and close agreements are observed. Additionally, the natural resonant frequencies of the combined modes for the cell-fibril configuration in Figure 4.2(b), are mainly governed by the natural resonant frequencies of the cell and not of the fibril.

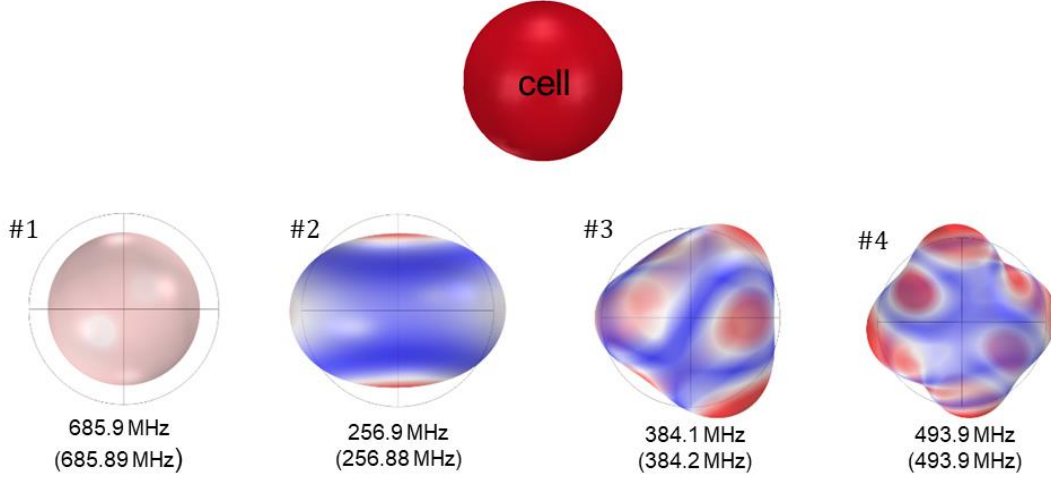


Figure 4.12. Structural mechanics modal analysis on an individual bacterial cell (analytical and numerical simulation). The natural resonant frequencies of the first four modes are in the sub-GHz range. Close agreement between the analytical frequencies and COMSOL eignefrequencies is achieved. The given values in the parenthesis are for the COMSOL simulation results.

4.3.2. COMSOL Simulation for Purposeful Communication

To elaborate more on the high frequency combined modes of vibration and visualize the concept of purposeful communication, COMSOL Multiphysics is utilized in this subsection. As a simple example, illustrated in Figure 4.13(a), two cells with their attached amyloid fibrils are considered with intercellular distance $R_d = 1 \mu m$. The cells and fibrils are modeled as solid spheres, and solid beams with the aforementioned mechanical properties. The amyloid fibrils are $1 \mu m$ in length (along the x -axis) and are attached to the cells' membrane with cross-section $2 \mu m \times 10 \mu m$. The transmitting cell (TX) is assumed to experience a sudden strain along z -axis given as,

$$\epsilon_z = \left(\frac{\Delta R}{R} \right)_z = 0.025 \times g(t) \quad (4.28)$$

where $g(t)$ is the time-domain representation of applied strain (see Figure 4.13(b)). With the applied strain, the cell is stretched along the z -axis by approximately 20 nm with a pulse having full width at half max (FWHM) of $\sim 2 \text{ ns}$. The applied sudden strain stress excites different modes of oscillation and initiates the communication. Consequently, the cell starts vibrating and in-turn

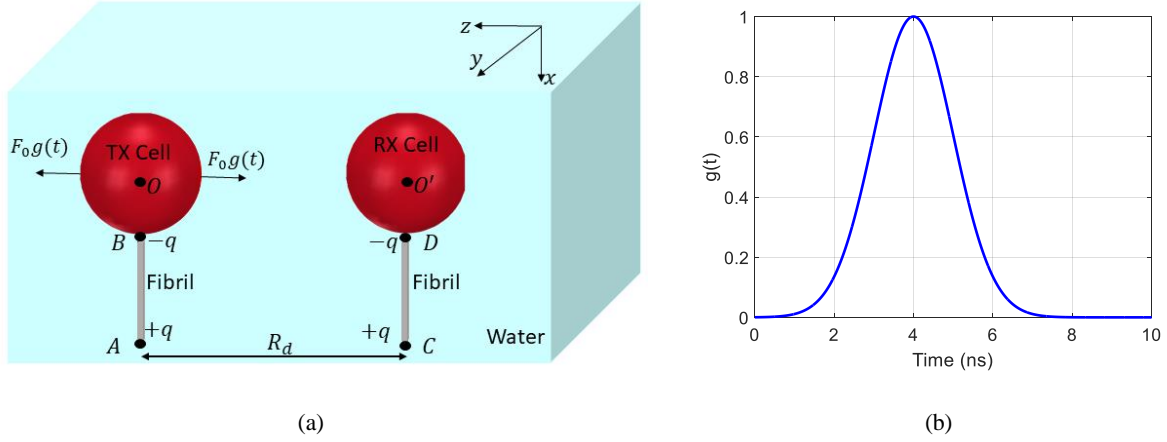


Figure 4.13. (a): 3D view of a bacterial cell with its attached amyloid fibril surrounded by water. The cell is experiencing an initial strain along the z -axis which in turn start vibrating and moving the amyloid fibril. The center of the TX and RX cells are located at $O(0,0,0)$ and $O'(0,0,-1)$ μm , respectively. (b): Time-domain profile of the applied strain to the cell.

transfers the vibration to the attached amyloid fibril. Given the fact that fibrils have opposite charges on their both ends, there would be two contributing electric fields in transmission mode ($\mathbf{E}_{total} = \mathbf{E}_{+q} + \mathbf{E}_{-q}$). Figure 4.14(a) and Figure 4.14(b) show the vibration amplitude of the transmitting amyloid fibril ends (point A and point B defined in Figure 4.13(a)), denoted as $d_A(t)$ and $d_B(t)$, respectively. It can be readily concluded that due to viscosity of water background of the biofilm, the vibration of fibrils and cells get damped quickly. Knowing the time-domain profile of each of the end's vibration, $d(t)$, the generated electric field by each of the fibril dipole charges can be calculated from [51],

$$\mathbf{E} = \frac{q}{4\pi\epsilon_r\epsilon_0} \left\{ \left[3 \frac{\dot{d}(t)}{u_p r^2} + 3 \frac{d(t)}{r^3} + \frac{\ddot{d}(t)}{u_p^2 r} \right] (\hat{r} \cdot \hat{d}) \hat{r} - \left[\frac{\dot{d}(t)}{u_p r^2} + \frac{d(t)}{r^3} + \frac{\ddot{d}(t)}{u_p^2 r} \right] \hat{d} \right\} \quad (4.29)$$

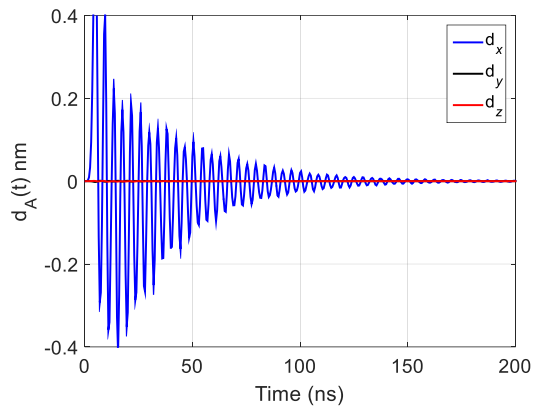
Here, q is the dipole charge of fibril, \hat{r} is the observation point measured from the location of each of the dipole charges at rest and \hat{d} is the vibration amplitude vector. u_p also represents the phase velocity. Keeping only those terms proportional to $\frac{1}{r^3}$ as we are dealing with the near-field

components (dimensions within a biofilm sample are in the order of $nm-\mu m$ and the frequency is within $kHz - GHz$ range), the expression for the electric field are simplified as,

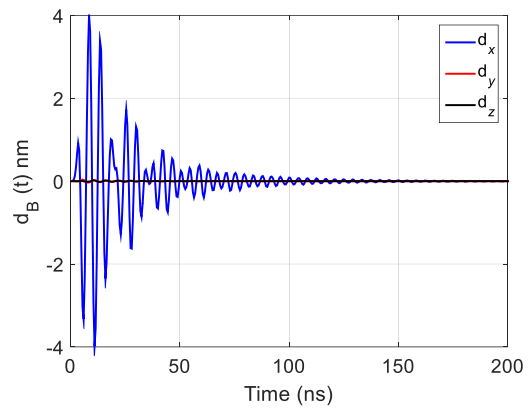
$$\mathbf{E} = \frac{q}{4\pi\epsilon_r\epsilon_0} \left\{ \frac{3}{r^3} (\hat{r} \cdot \hat{d}) \hat{r} - \frac{1}{r^3} \hat{d} \right\} d(t) \quad (4.30)$$

This indicates that the profile of induced electric field is proportional to the vibration amplitude of fibril. Setting fibrils dipole charges [23] $q = \pm 3e^-$ (e^- is the electron charge value), Figure 4.14(c) and Figure 4.14(d) show the received electric-field by the RX cell at point D and point O' (see Figure 4.13(a)), respectively. For signal reception, the induced electric field can either exert force on charges of receiving fibrils to be sensed by the corresponding cell or it can move certain charged messenger protein within the cell. In order to obtain the frequency spectrum of EM signaling among the cells and find the possible communication frequencies, the FFT of the generated electric field is calculated and the result is plotted in Figure 4.14(e) and Figure 4.14(f). It is clearly shown that cells and amyloid can produce an electromagnetic spectrum that includes frequencies up to about 5 GHz. However, as the frequency gets larger, the signal level decreases drastically indicating that based on this model, communication at frequencies below 2-3 GHz is more probable specifically around 500 MHz.

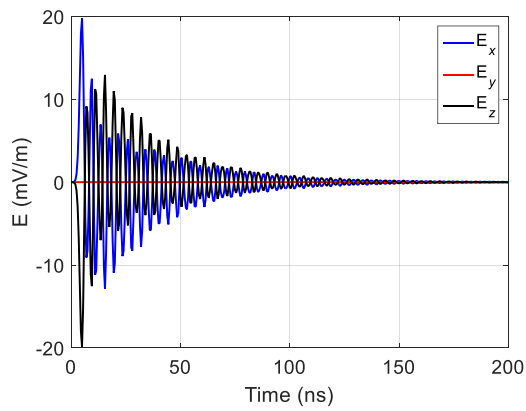
As we proposed several Multiphysics model regarding the EM signaling among biological cells, Table 4.2 provides an overview of all these schemes in terms of possible communication frequencies.



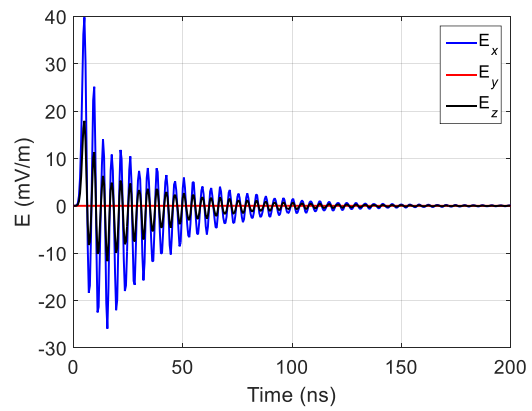
(a)



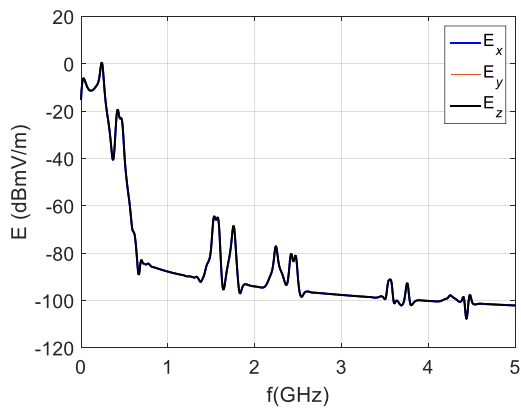
(b)



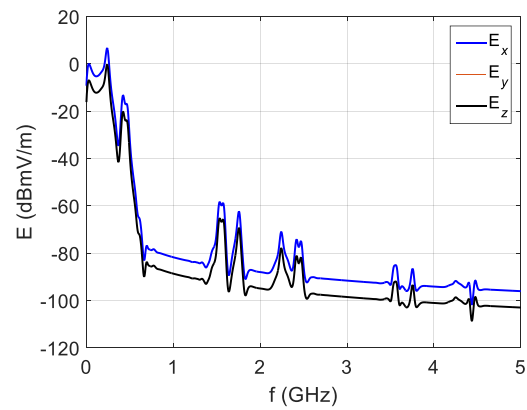
(c)



(d)



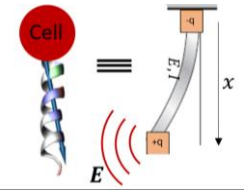
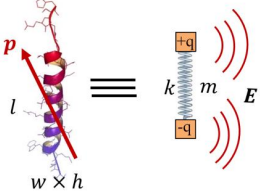
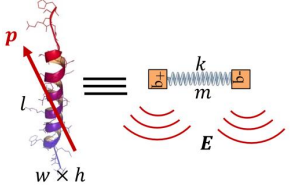
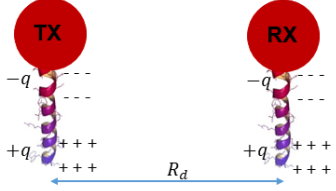
(e)



(f)

Figure 4.14. (a): Vibration amplitude of the transmitting fibril's ends at point A ($d_A(t)$). (b): Vibration amplitude at point B ($d_B(t)$). (c): Received electric by the RX cell at point O' . (d): Received electric field at point D . (e): FFT of the received electric field at point O' . (f): FFT of received E-field at point D . For the definition of points A , B , O' , and D , refer to Figure 4.13(a).

Table 4.2. Summary of Proposed Models for EM Signaling among Biological Cells.

Model	EM Signaling Frequency Range
<p style="text-align: center;">Cantilever Beam</p> 	<p>~20 kHz-600MHz</p>
<p style="text-align: center;">Longitudinal Spring Vibration</p> 	<p>~0.5GHz-6GHz</p>
<p style="text-align: center;">Transverse Spring Vibration</p> 	<p>~10GHz-50GHz</p>
<p style="text-align: center;">Purposeful EM Signaling</p> 	<p>~0.5GHz-3GHz</p>

4.4. Comparative Study between EM Signaling and Quorum Sensing (QS) in Biofilms: Communication Data Rate

So far, we have developed a model that conceptually depicts a theory for EM-based communication between bacteria within biofilms. The next question that needs to be addressed is

why such mechanism may be needed while the cells are capable of communicating with each other through transmitting and intercepting chemical messengers (proteins, and ions). In the QS process, Gram-positive bacteria such as *S. aureus* use an oligopeptides denoted as AIPs, a chemical messenger [147]. For the reception, signaling event in bacteria occurs when the concentration of autoinducers near cell membrane reaches a specific threshold concentration [148].

In this section, a quantitative comparison between these communication pathways is presented. As illustrated in Figure 4.15, the comparison is based on evaluating the schemes' corresponding communication channel and compare their channel capacity (bit rate). The two individual cells are considered as transmitter and receiver (separation distance R_d). The challenging part is to model the communication channel itself and to understand how the message signal propagates within the medium and is captured by the cells.

4.4.1. EM-Based Channel Capacity Estimation

Figure 4.16(a) shows the scenario where two cells communicate through electromagnetic waves by means of their hinged amyloid fibrils. As mentioned, the cell with its hinged fibril can be modeled as a cantilever beam with dipole charges at its both ends. These two charged fibrils under acceleration act as transmitting and receiving antennas, respectively. Therefore, this can be modeled as an antenna system as shown in Figure 4.16(b). The channel capacity (bit/second) in this scenario then can be obtained using the well-known Shannon theorem [149],

$$C = B \log_2 \left(1 + \frac{S}{N} \right) = B \log_2 \left(1 + \frac{\langle E^2 \rangle}{\langle E_n^2 \rangle} \right) \quad (4.31)$$

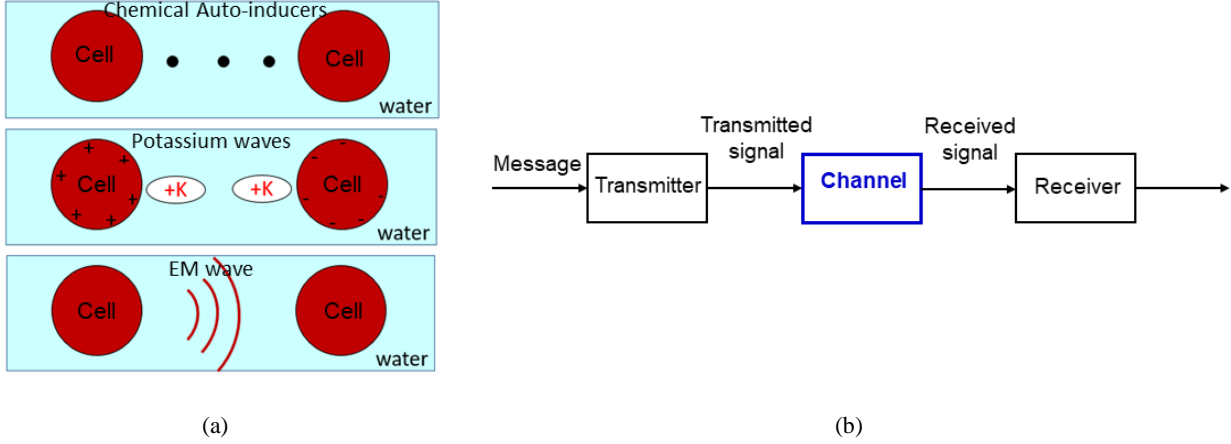


Figure 4.15. (a): Two individual cells are communication through either chemical messengers (autoinducers or ions) or EM waves. (b): Communication channel representation for these schemes. Individual cells are considered as transmitters and receivers.

where B is the bandwidth of communication, $\langle E^2 \rangle$ is the statistical average of power (square of the electric field) captured by the receiving cell from the emitting cell and $\langle E_n^2 \rangle$ is the noise power at the receiving cell. The expression for $\langle E^2 \rangle$ can be written as,

$$\langle E^2 \rangle = \left(\frac{1}{2} |E_{+q}(r = R_d) + E_{-q}(r = R_d)| \right)^2 \quad (4.32)$$

where, $\pm q$ is the dipole charge associated with the fibrils, and R_d is the distance between the two cells (or fibrils). The factor $\frac{1}{2}$ accounts for the average relative orientation of the two fibrils. The expressions for E_{+q} and E_{-q} are the same as what provided in Eq. (4.30). The background medium between the two cells is assumed to be water ($\epsilon_r = 81$). For the noise power estimation, here we have used the blackbody radiation assumption as shown in Figure 4.16(c). Considering Rayleigh-Jean's specific intensity for blackbody radiation noise [149],

$$I_f = \frac{2KT}{\lambda^2} \frac{W}{m^2 Hz sr} \quad (4.33)$$

and assuming a transverse electromagnetic (TEM) approximation for the noise (uniform angular dependency), the noise power density can be obtained as,

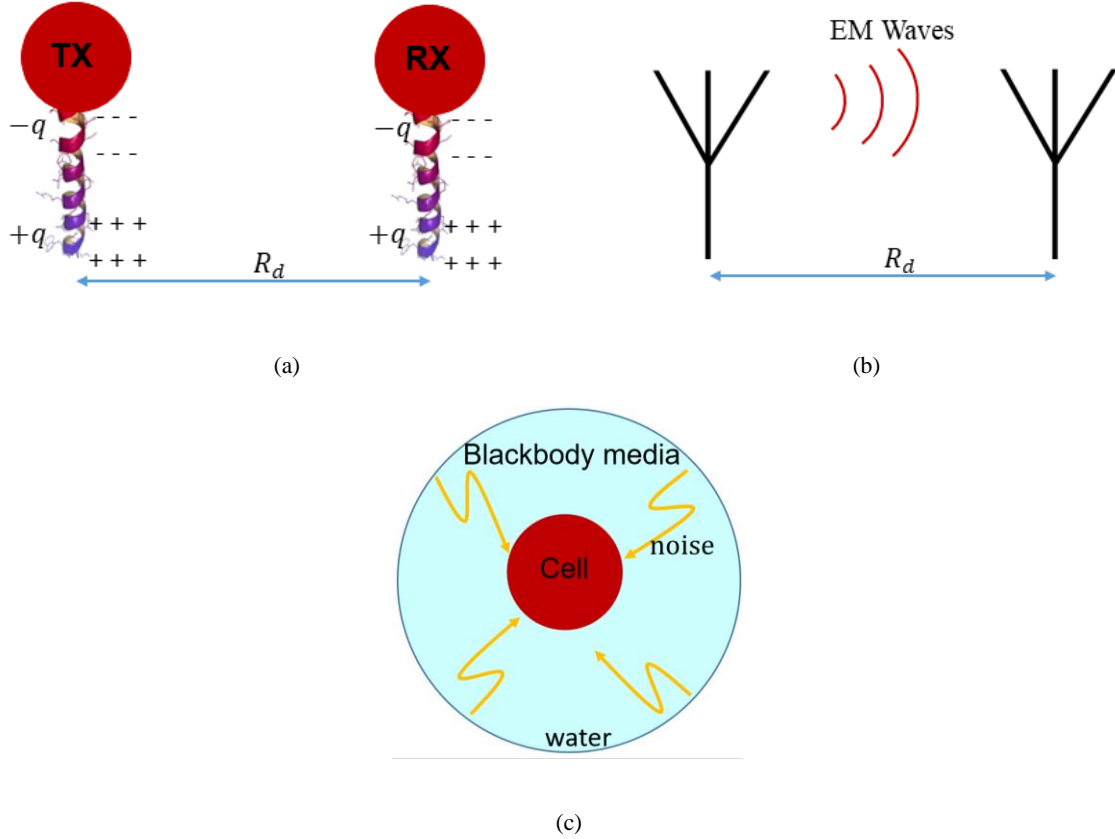


Figure 4.16. (a): Two cells communicate through EM waves by moving their hinged amyloid fibrils. (b): Its equivalent antenna system model as the dipole charges radiate through mechanical vibration of the amyloid fibrils. (c): Blackbody assumption for noise power estimation at the receiving cell.

$$\frac{\langle E_n^2 \rangle}{2\eta} = 4\pi I_f \times B = \frac{8\pi KT}{\lambda^2} \beta \rightarrow \langle E_n^2 \rangle = \frac{16\pi\eta KT}{\lambda^2} \beta \quad (4.34)$$

T is the temperature (298 K), K is the Boltzmann constant, and λ is the communication wavelength related to the fibril vibration frequency (f_0) as $f_0 = c/\lambda$. This is because a vibrating charge with frequency f_0 radiates EM signals at the same frequency. β here is also the communication bandwidth since the vibration of fibrils occurs in water as a viscous background (damped). Using Eq. (4.32) and Eq. (4.34) along with the Eq. (4.31), one can find the corresponding channel capacity as a function of different parameters which will be discussed in the following result section (4.4.3).

4.4.2. QS Channel Modeling

All known QS networks operate as an “on–off” gene expression switch [150]. Until a certain critical autoinducer concentration is reached, the intracellular network must remain in the “off” state with inactive autoinducer production and less than one molecule of transcription factor per cell. Above the threshold, the transcription factor is expected to be found in detectable concentrations sufficient to stably activate (or repress) expression of all target operons [150]. Figure 4.17(a) depicts our model proposed for channel capacity estimation of quorum sensing. The well-known slotted binary channel is considered here (with time slot duration τ) [151]. A cell releases N_1 molecules with probability p to transmit “ $X = 1$ ” and releases N_0 spherical molecules with probability $1 - p$ to transmit “ $X = 0$ ”. All the message molecules are assumed to be released by the cells spontaneously at the beginning of each time slot. The received symbol is “ $Y = 1$ ” if the number of intercepted messengers at the corresponding time slot (k) is greater than or equal to a threshold number (N_{th}), and “ $Y = 0$ ” if $k < N_{th}$. It should be stated that the proposed communication channel in fact provides an upper bound for the channel capacity of QS because in reality, there is no such definite pulse modulation for the number of transmitting particles by the cells. This can in turn drastically reduce the channel capacity. For channel capacity calculations here, we need to find the probability of successful bit transmission, s_n and g_n (Figure 4.17(b)) defined as,

$$s_n = P_r[Y_n = 1|X_n = 1], \quad g_n = P_r[Y_n = 0|X_n = 0] \quad (4.35)$$

Denoting $u_n(k|x)$ as the conditional probability of receiving k message molecules during the time slot n given $x = 0$ or 1 in the same time slot, the expressions for s_n and g_n can be written as,

$$s_n = 1 - \sum_{k=0}^{N_{th}-1} u_n(k|1) \quad (4.36)$$

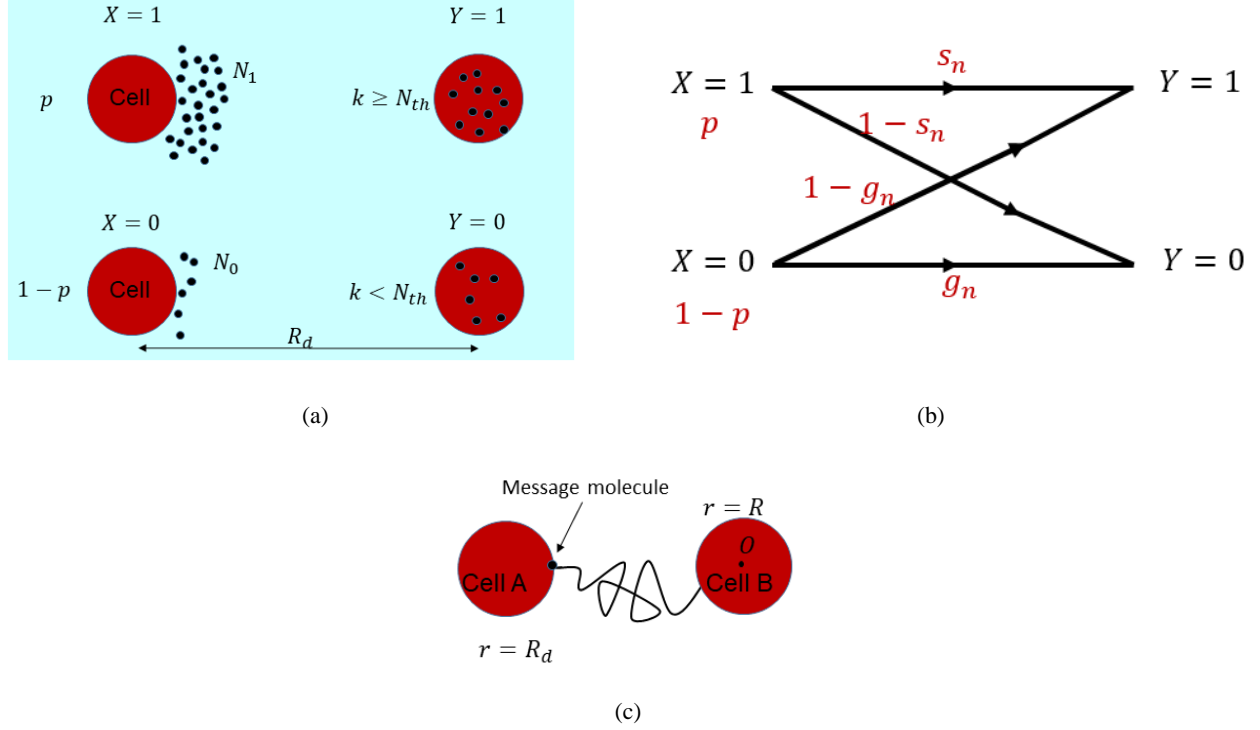


Figure 4.17. (a): Physical model proposed for estimating channel capacity of quorum sensing based on diffusion phenomena. (b): Its binary channel representation. (c): Brownian motion of one autoinducer released by the transmitting cell to be captured by the receiving cell as a purposeful message. The distance between two cells is R_d .

$$g_n = \sum_{k=0}^{N_{th}-1} u_n(k|0) \quad (4.37)$$

For the first time slot ($n = 1$), using a binomial distribution for the number of receiving particles, it can be readily shown that,

$$u_1(k|x) = \begin{cases} \binom{N_x}{k} q_0^k (1 - q_0)^{N_x - k} & k \leq N_x \\ 0 & k > N_x \end{cases} \quad (4.38)$$

For $n \geq 2$, considering a recurrence relation, we have [152],

$$u_n(k|x) = (1 - p) \sum_{j=0}^{\min(k, N_0)} \binom{N_0}{j} q_{n-1}^j (1 - q_{n-1})^{N_0 - j} u_{n-1}(k - j|x)$$

$$+p \sum_{j=0}^{\min(k, N_1)} \binom{N_1}{j} q_{n-1}^j (1 - q_{n-1})^{N_1-j} u_{n-1}(k - j|x) \quad (4.39)$$

In the above two equations for u_n , there is a parameter denoted as q_m ($m = 0, 1, 2, \dots$). q_m is the probability that a single molecule transmitted in slot $i \in \{1, 2, \dots, n\}$ arrives at the receiver in slot n where $m = n - i$. This quantity should be calculated using the Fick's diffusion equation in three dimensions, as it relies on the diffusion of protein molecules (messages) within the water background of the biofilm. Following subsection gives the details of calculating q_m . Knowing the s_n and g_n from Eq. (4.36) to Eq. (4.39), the mutual information achieved in the time slot n can be written as [153],

$$\begin{aligned} I(X_n; Y_n) &= H(Y_n) - H(Y_n|X_n) \\ &= h((1 - p)g_n + p(1 - s_n)) - \{p h(s_n) + (1 - p)h(g_n)\} \end{aligned} \quad (4.40)$$

where

$$h(x) = -x \log_2 x - (1 - x) \log_2 (1 - x) \quad (4.41)$$

After finding the mutual information, the channel capacity can be expressed as [153],

$$C = \lim_{\ell \rightarrow \infty} \max_p \sum_{j=1}^{\ell} \frac{I(X_j; Y_j)}{\tau \ell} \quad (4.42)$$

For the analysis of QS channel capacity in the results section, we have set $N_{th} = 1$, $N_0 = 0$. This means that among N_1 molecules released by the transmitting cell at the beginning of a time slot, only one molecule is required to be captured by the receiving cell to be interpreted as "Y = 1" (Figure 4.17 (a)).

The last step to estimate the channel capacity associated with the QS is to find the expression for q_m . As mentioned, q_m is the probability that a single molecule transmitted in slot $i \in \{1, 2, \dots, n\}$ arrives at the receiver in slot n where $m = n - i$ [152]. To obtain this parameter, we first define a function called the First Passage Time Distribution (FPTD) [154]. The FPTD function, represented by $f(t)$, is in fact the probability distribution function of time of arrival of a particle for a fixed distance through a random walk. Once $f(t)$ is known, the expression for q_m is given as [152],

$$q_m = \int_{m\tau}^{(m+1)\tau} f(t) dt \quad ; \quad m = n - i \quad (4.43)$$

In order to find the function $f(t)$, let us consider a message molecule released by Cell A at a distance of R_d from Cell B (Figure 4.17(c)). Both cells have a radius of R . The molecule size is assumed to be negligible compared to the cell size. The well-known Fick's equation can be used to account for the Brownian motion of this molecule. Defining $w(r, t)$ as the probability density of finding the particle at (r, t) , it follows the Fick's equation [155],

$$\begin{aligned} w_t &= D \left[w_{rr} + \frac{2}{r} w_r \right] \quad r > 0, t > 0 \\ w(r, 0) &= \frac{1}{4\pi R_d^2} \delta(r - R_d) \quad r > a \\ w(a, t) &= 0 \quad t > 0 \end{aligned} \quad (4.44)$$

Here, D is the diffusion coefficient of the particles, and r denotes the radial distance. w_t is the first-order time derivative of w and w_{rr} stands for the second-order derivative of w with respect to r . Assuming spherical symmetry for this problem, and solving Eq. (4.44) for $w(r, t)$, it can be shown that,

$$w(r, t) = \frac{R}{R_d} \frac{1}{\sqrt{4\pi Dt}} \left[\exp\left(-\frac{(r - R_d)^2}{4Dt}\right) - \exp\left(-\frac{(r - (2R - R_d))^2}{4Dt}\right) \right] \quad (4.45)$$

Defining $S(R, t)$ as the probability of finding the particle outside the receiving cell, we have [156],

$$S(R, t) = \int_a^{+\infty} u(r, t) dr = \frac{R}{R_d} \operatorname{erf}\left[\frac{(R_d - R)}{\sqrt{4Dt}}\right] \quad (4.46)$$

where, $\operatorname{erf}(\ast)$ is the well-known error function. Once $S(R, t)$ is obtained, the expression for the FPTD function ($f(t)$) is,

$$f(t) = \frac{d}{dt} (1 - S(R_d, t)) = \frac{D}{R^2} \left(1 - \frac{R}{R_d}\right) \exp\left(-\frac{(R_d - R)^2}{4Dt}\right) \frac{1}{2\sqrt{\pi} \sigma^2}; \quad \sigma = \frac{Dt}{R^2} \quad (4.47)$$

Qualitatively speaking, the FPTD function depends on the protein (message molecule) diffusivity in the water background of the biofilm, the cell radius (a), and the distance between the two cells (R_d). Using Eq. (4.47) along with Eq. (4.36) and Eq. (4.37), we now have the expressions for s_n and g_n .

Considering the scenario illustrated in Figure 4.17(c), the critical time of arrival (τ_c , the most probable arrival time of the message molecule from the transmitting cell to the receiving one) is,

$$\frac{df(t)}{dt} = 0 \rightarrow \tau_c \sim \frac{R_d^2}{6D} \quad (4.48)$$

This quantity is an important parameter as discussed in the following result section.

4.4.3. Results and Comparative Study

Figure 4.18(a) and Figure 4.18(b) show the channel capacity calculated for QS as a function of the number of released particles (N_1) for two different separation distance between the cells (R_d) and for various time slot durations (τ). The time slot durations correspond to the critical

arrival time for $R = 0.5, 1, 2,$ and $5 \mu m$. In our calculations, we have set $D = 10^{-10} \frac{m^2}{s}$ [41] and $N_0 = 0$. Also, the threshold concentration of autoinducers (AIP-I) for gene activation is experimentally found to be $5000 nM$ [157] or equivalently, considering the cell volume (sphere with radius, $R = 350 nm$), $N_{th} = 1$. As can be concluded from these two figures, the longer the distance between the communicating cells is, the lower the channel capacity would be for the same time slot duration τ . Additionally, when τ gets shorter, the channel capacity increases until τ reaches the critical arrival time (τ_c) defined in Eq. (4.48). If the pulse duration becomes smaller than τ_c , the message molecules coming from consecutive time slots will not have enough time to reach the receiving cells and get mixed together. The receiver will then be confused with high probability and the channel capacity will drop drastically.

For EM signaling channel capacity, the same scenario as what described in subsection 4.3.2 and shown in Figure 4.13(a) is considered. The strength of the electric field received by the RX cell (at point O' defined on Figure 4.13(a)), E , is calculated for various intercellular distances (R_d). According to the frequency spectrum of the received E -field in Figure 4.14(e), the channel capacity is examined at its peak frequencies ($f = 0.24$ GHz, 0.42 GHz, and 1.5 GHz). The bandwidth (β) for each of these frequencies is considered to be -3dB bandwidth corresponding to the frequency spectrum of E -field illustrated in Figure 4.14(e). These bandwidth are found to be 33 MHz, 30 MHz, and 6.7 MHz, respectively. Then, Eq. (4.32) and Eq. (4.34) are applied.

As the last and also the most important result, Figure 4.18(c) and Figure 4.18(d) compare the channel capacity for both QS and EM-based communication within biofilms as a function of distance. As is shown, electromagnetic-based communication provides approximately 5-7 orders

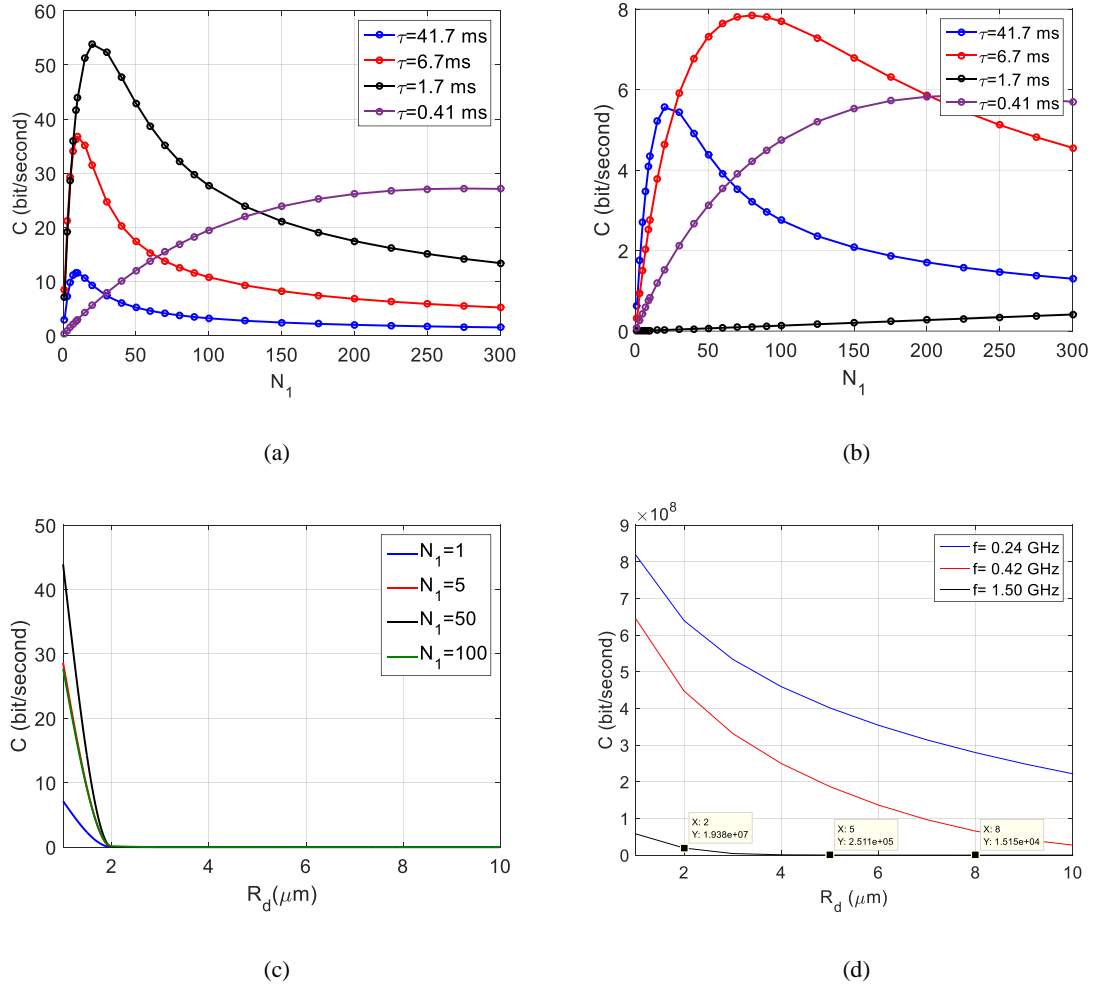
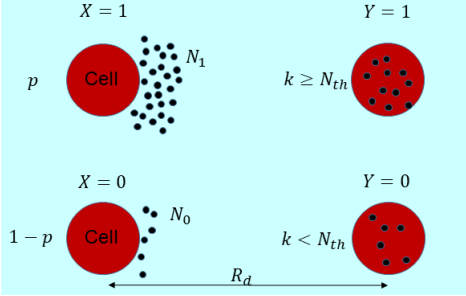
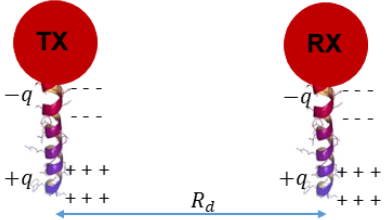


Figure 4.18. The channel capacity estimation for QS as a function of the number of messenger molecules released by the transmitting cell (N_1). (a): $R_d = 1 \mu m$ ($\tau_c = 1.7 ms$). (b): $R_d = 2 \mu m$ ($\tau_c = 6.7 ms$). R_d is the distance between the two communicating cells. The channel capacity estimation as a function of distance between two cells. (c): quorum sensing. (d): EM-based communication.

of magnitude higher channel capacity compared to QS and its coverage range is much longer. These two concluding remarks indicate that EM signaling can significantly outperform its biochemical counterpart. Table 4.3 provides a summary for the channel capacity comparisons between these two schemes.

Table 4.3. Summary of Proposed Multiphysics Models for Channel Capacity Estimations.

	<p style="text-align: center;">Quorum Sensing</p> 	<p style="text-align: center;">EM Signaling</p> 
<p>Model/Quantity</p>	<p>Slotted binary channel + Brownian motion (Fick's diffusion)</p>	<p>Shannon Theorem</p>
<p>Physics</p>	<p>$D = 10^{-10} \frac{m^2}{s}$, $N_{th} = 1$, $N_0 = 0$</p>	<p>$K = 1.38 \times 10^{-23}$, $T = 298K$, $\eta = 120\pi$, E, β, λ: from frequency spectrum in Figure 4.14(e)</p>
<p>Parameters</p>	<p>0-50 bit/second (over 1-10 μm range)</p>	<p>10^4-10^9 bit/second (over 1-10 μm range)</p>
	<p>Channel Capacity</p>	

4.5. Conclusion

This chapter presented a theoretical model explaining how individual cells can transmit and receive electromagnetic waves. The fundamentals of operation of embedded radios within cellular structures is based on mechanical antennas. Permanent charged dipoles within and around biological cells can be accelerated at their natural resonant frequencies through the cell's natural metabolic activities and radiate electromagnetic signals from $KHz - THz$ frequencies. In specific, amyloid fibrils which are long fibers formed by aggregates of peptides with a specific dipole moment, are considered. We postulated that once one of the vibrational modes of amyloid fibrils is excited by the cells, it induces EM fields to communicate with adjacent cells. For the reception, emitted EM fields will exert force on the dipole charges of fibrils or move protein molecules within

the cell. The modeling results show that fibrils having cantilever beam mode of vibration generate EM waves within the $kHz - MHz$ range, and their mechanical spring modes excite GHz signals. While experimental evidence for EM signaling will need to be obtained and undergo scrutiny, the quantified comparisons between EM and QS modes of communication can be useful for future studies, indicating that the EM route provides much higher data rate and also over longer range compared to QS.

CHAPTER 5

Conclusion and Future Directions

5.1. Research Summary and Contributions

In this dissertation, as a major contribution, we have developed couple of multiphysics models that can unravel the concept of electromagnetic-based communication recently hypothesized as a new communication paradigm among biological cells including bacterial communities (biofilms). This study is particularly advantageous, as biologists would further investigate to clarify the purpose of information transferred through such signaling so as to control the physiological activities of infectious bacteria and cancer tumors for instances. For the sake of modeling this EM-based communication and the antennas cells are equipped with, we have utilized our developed antenna design concepts at low frequencies (VLF and VHF bands), namely mechanical antennas and fragmented antennas.

The proposed mechanical antenna system here with its unique phase modulation and frequency multiplication capability would enable reliable and practical wireless underwater, underground, and over-the-horizon communication at the VLF band (3-30 kHz) and lowers. This antenna system readily overcomes the design trade-off between the size (being handheld) and radiation efficiency of antennas operating at such low frequencies ($\lambda > 1$ km). Furthermore, its phase modulation and frequency multiplication potentially enhance the communication bandwidth, and improve the mechanical stability of the antenna system, respectively.

The proposed fragmented antenna which is based on creation of an electrically-large antenna from ensemble of electrically-small antennas, provides significant bandwidth enhancement for small antennas. The design concept is aimed for VHF indoor and urban communication links and is readily applicable to mobile platforms including UAVs which have numerous applications in tactical communication, cargo and medicine transportation, and geographical surveys.

5.2. Recommended Future Works

5.2.1. Mechanical Antennas

The proposed mechanical antenna system as shown in Figure 2.4 is based on a mechanically-rotating magnet sandwiched between two pairs of orthogonal bow-tie shape ferrite plates. The design is followed by sufficient mathematical, and numerical analysis. But the measurements are limited to only short ranges (< 30 cm). For practical applications, it would be highly advantageous if measurements could be extended to longer ranges (> 10 m) through using more sensitive magnetic probes [88] and/or increasing the rotation frequency (DC motor frequency) and magnet size.

Our fabricated antenna is operating at 50 Hz and has maximum dimension of 10 cm (see Figure 2.16). This indicates that the antenna is still extremely-small fraction of the wavelength and new design approaches should be devised for the antenna far-field strength enhancement. This is mainly due to the fact that for efficient radiation, the electrical size of the antenna should be close to $\lambda/2$. One idea which requires further investigations would be to use multi-layer magneto-dielectric spheres in the design as illustrated in Figure 5.1. Intuitively speaking, the proposed design would enhance the electrical size of the antenna by a factor of roughly $\sqrt{\mu_2 \epsilon_2 \mu_3 \epsilon_3}$.

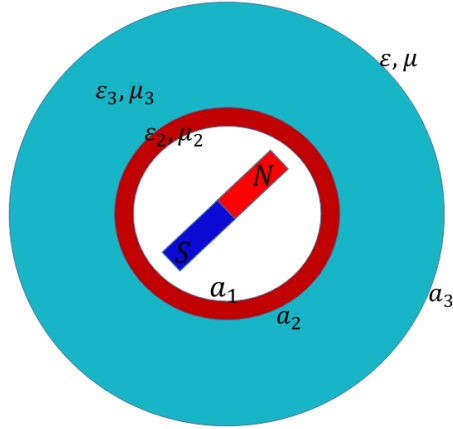


Figure 5.1. The proposed idea for enhancing the far-field strength of mechanical antennas (rotating magnet) through using magneto-dielectric resonance concept.

Appendix C provides some preliminary analysis on the proposed idea and how magneto-dielectric resonance would explain this capability.

5.2.2. Fragmented Antennas

Our proposed fragmented antenna is based on a cluster of detached electromagnetically-coupled folded dipole antennas with inductive end-loads. The design provides 7 times improvement in -10dB bandwidth compared to single element antenna. It also tolerate the variation of separation distance between the antennas (on mobile platforms such as UAVs) through use of a tunable matching circuit. As one recommendation for the future works, while the UAV motivation is very interesting, some preliminary flight test results would further strengthen the idea. In order to enhance the bandwidth of fragmented antenna even more and also over longer ranges, one potential idea is to utilize 3-fold dipole antennas (or higher orders) instead of folded dipole antennas as shown in Figure 5.2. 3-fold dipole antenna has inherently larger impedance compared to fold dipole ($(\frac{3}{2})^2$) and its end-loads induce stronger magnetic field which can enhance the separation distance between adjacent antennas for strong EM coupling. Table 5.1 summarize the

Table 5.1. Comparative Study between Bandwidth and Input Impedance of Two Coupled Antennas.

Antenna Configuration	BW (3-fold)	BW (folded)	Z_{in} (3-fold)	Z_{in} (folded)
Single Antenna	3.4 MHz	2.3 MHz	50 Ω	20 Ω
Two Coupled Antennas ($d= 6\text{cm}$)	22.31 MHz	19.78 MHz	250 Ω	160 Ω
Two Coupled Antennas ($d= 8\text{cm}$)	17.68 MHz	14.52 MHz	180 Ω	110 Ω
Two Coupled Antennas ($d= 10\text{cm}$)	13.00 MHz	10.5 MHz	130 Ω	90 Ω

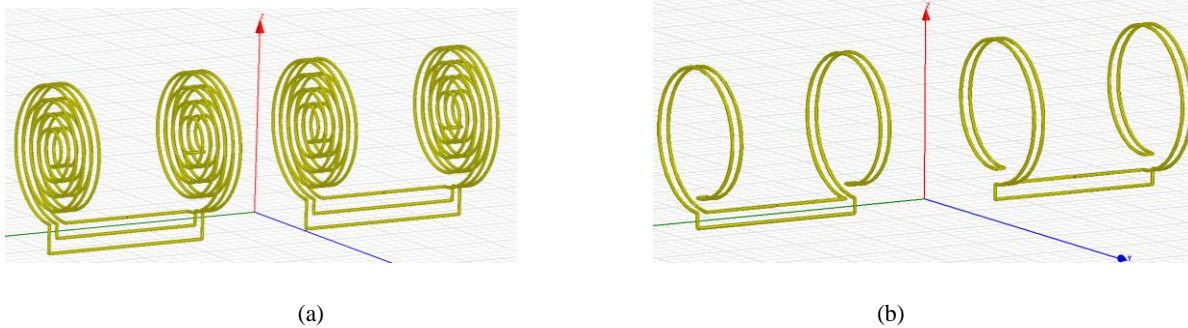


Figure 5.2. Two electromagnetically-coupled antennas with inductive end-loads, (a): 3fold dipole antennas, (b): folded dipole antennas.

input impedance and bandwidth for two-closely-separated folded and 3-fold dipole antennas. It should be noted that in this table, the reported bandwidth and impedances are for the case where the second antenna is terminated to its match-load (not capacitive or inductive loads).

Another suggestion for the future works would be to utilize negative resistance for loading the assistive antennas in a fragmented antenna as depicted in Figure 3.1. In this way the reflection coefficient at assistive antennas' ports would be greater than unity and thus stronger current flows on the adjacent antennas. Consequently, the antenna gain is expected to enhance. Using Ansys Electronics, this has been verified through loading the assistive antennas (Figure 3.1) with a negative resistance ($R = -135 \Omega$) the result of which is provided in Figure 5.3. For the realization

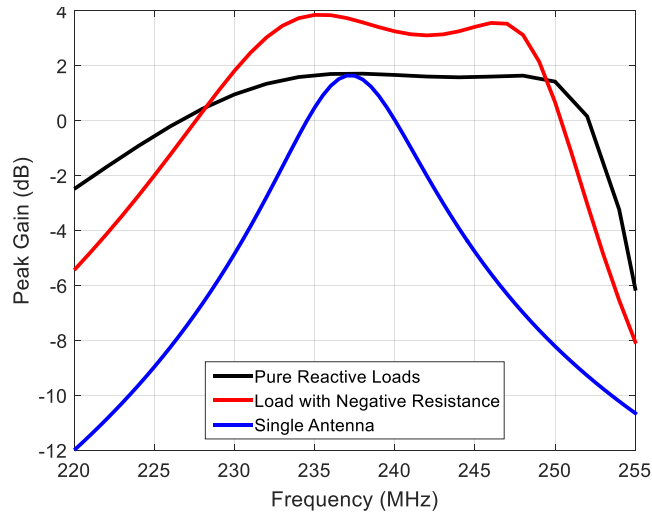


Figure 5.3. Application of negative resistance in fragmented antenna for gain enhancement.

of negative impedance, one simple way is the use the cross-coupled transistor configuration [158], [159].

5.2.3. Multiphysics Modeling of EM Signaling among Biological Cells

Similar to the concept of mechanical antennas, we postulate that vibration of charged amyloid fibrils, as part of the EPX matrix in biofilms, induces electromagnetic (EM) radiation among biological cells. Different vibrational modes associated with the fibrils are considered indicating viable EM frequencies ranging from *kHz* to *THz*. Multiphysics models are also proposed to unravel such communication scheme. After finding compelling evidences through numerous measurements, it is encouraging to return back to the developed models for fine-tuning purposes to achieve excellent agreement between the measurements and the simulation predictions. There are in fact lots of parameters in the modeling with uncertainty in their corresponding actual values.

Another recommended future direction for this modeling would be to envision the role of acoustic waves in biofilms and show that similar to the concept of fragmented antenna, the

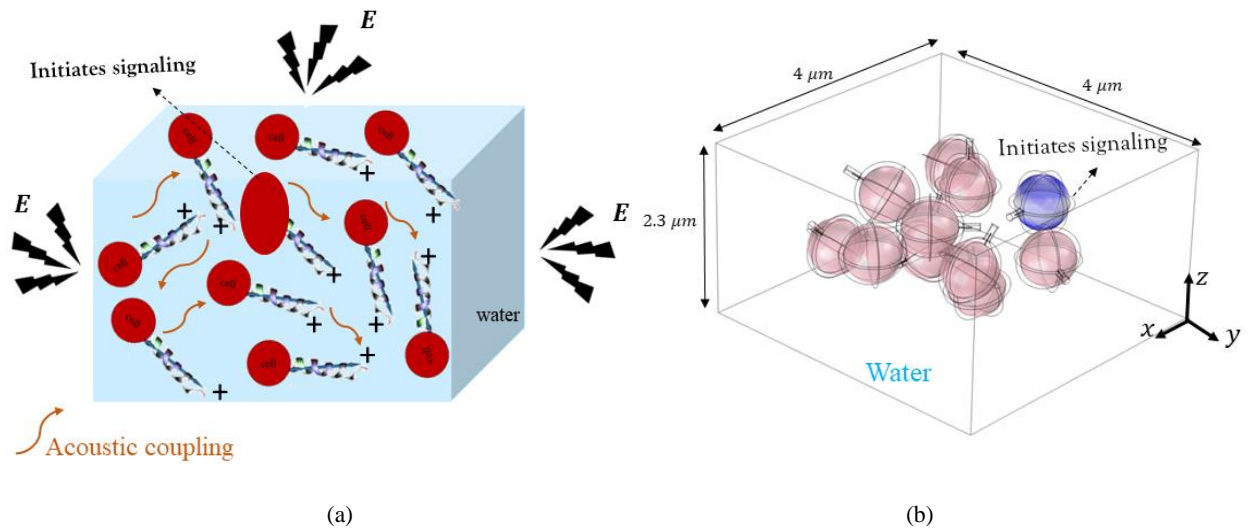


Figure 5.4. (a): Acoustically-coupled biological cells induce stronger electric field compared to an individual cells. (b): Simulated biofilm sample in COMSOL.

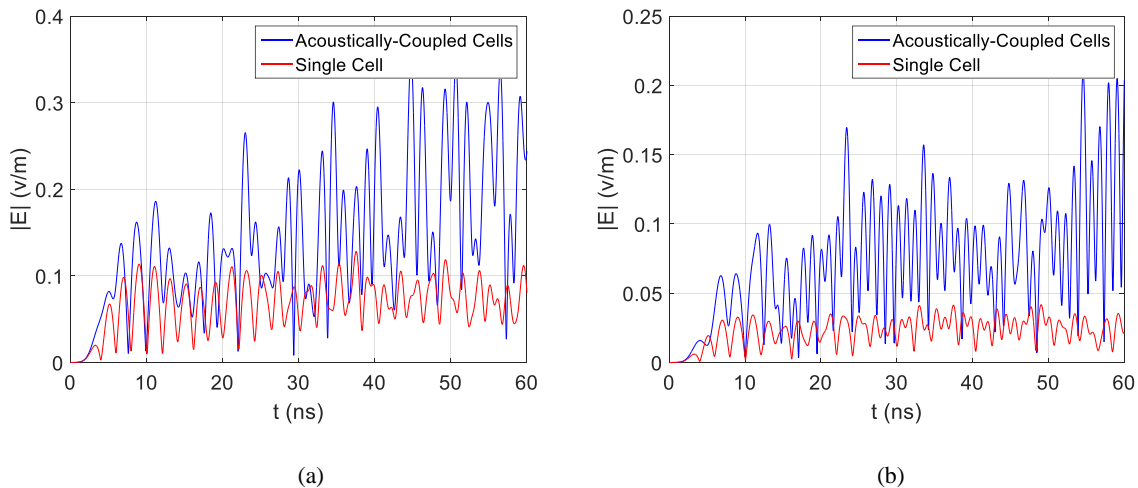


Figure 5.5. Impact of acoustic coupling between the cells on the emitted E-field from the biofilm sample at points (a): $(2,-2,5)\mu\text{m}$, and (b): $(2,-8,1)\mu\text{m}$. The coordinate system for these points is defined on Figure 5.4(b). The origin of the coordinate system is also shown in that figure.

vibration of community of cells and corresponding charged amyloid fibrils can be coupled acoustically so as to have stronger EM emission from a biofilm sample. As a preliminary simulation using COMSOL Multiphysics software, a small community of bacterial cells with their corresponding amyloid fibrils are simulated in water background medium as shown in Figure 5.4. One of the cells gets deformed initially to communicate while coupling to other adjacent cells

through acoustic wave which in turn start vibrating their charged amyloid fibrils. Consequently, it is expected that stronger E-field is generated through such acoustic coupling mechanism compared to the individual cell (without presence of other adjacent cells) as proven in Figure 5.5.

5.3. Closing

$$\nabla \cdot \mathbf{D} = \rho$$

$$\nabla \cdot \mathbf{B} = 0$$

$$\nabla \times \mathbf{E} = -\frac{\partial}{\partial t} \mathbf{B}$$

$$\nabla \times \mathbf{H} = \mathbf{J} + \frac{\partial}{\partial t} \mathbf{D}$$

Appendices

Appendix A: Mathematical Representation of Proposed Phase Modulation (PM) in Mechanical Antennas

In this appendix, the proposed phase modulation scheme for mechanical antennas in the chapter 2 is explained mathematically. Let us assume the magnetic (or electric) field generated by a rotating permanent magnet with angular velocity ω_0 (Figure 2.1(a)) is given as,

$$H(t) = \cos(\omega_0 t) \quad (\text{A.1})$$

Now, consider the bow-tie shape magnetic plates are introduced in the path of the rotating magnet (Figure 2.4). As explained intuitively in the chapter 2, the fields corresponding to the proposed mechanical antenna can be mathematically be expressed as,

$$H_T(t) = H(t) \times x_T(t) \quad (\text{A.2})$$

where $x_T(t)$ is a periodic pulse function with periodicity T , amplitude A , and the pulse width T_p as shown in Figure A.1. The time slots at which the pulse function reaches zero correspond to the times at which the magnet is completely covered by the magnetic posts. Such periodic functions in general can be written in their Fourier series representation as,

$$x_T(t) = \sum_{n=0}^{\infty} a_n \cos(n\omega t) \quad (\text{A.3})$$

with coefficients,

$$a_n = \begin{cases} \frac{AT_p}{T} & n = 0 \\ 2 \frac{A}{n\pi} \sin\left(n\pi \frac{T_p}{T}\right) & n \neq 0 \end{cases} \quad (\text{A.4})$$

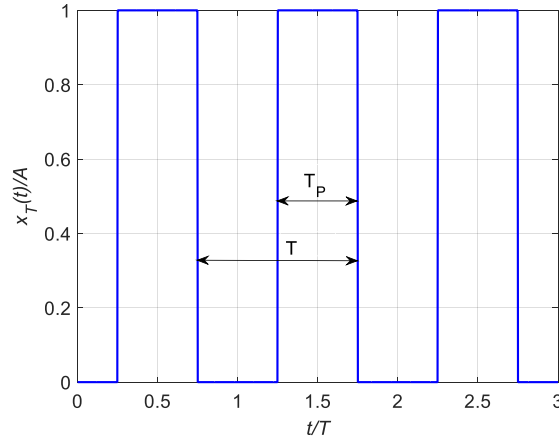


Figure A.1. The periodic pulse function applied to modulate the pure sinusoidal EM signal from the rotating

where $(\omega = \frac{2\pi}{T})$. For the proposed magnetic plates geometry (see Figure 2.4), we have $\omega = 4\omega_0$.

This is because of the fact that this configuration is periodic with angular separation of 90° .

Therefore, the time-domain modulated EM field is,

$$H_T(t) = H(t)x_T(t) = \cos(\omega_0 t) \times \sum_{n=0}^{\infty} a_n \cos(4n\omega_0 t) \quad (\text{A.5})$$

Mathematically speaking, changing the initial position of the magnetic plates is equivalent to a time shift (T_1) in the $x_T(t)$. Thus, the modulated EM fields based on the change in the initial position of posts ($\varphi_0 = \omega_0 T_1$) can be written as,

$$H_T^m(t) = H(t) \times x_T(t - T_1) = \cos(\omega_0 t) \times \sum_{n=0}^{\infty} a_n \cos(4n\omega_0 t - 4n\omega_0 T_1) \quad (\text{A.6})$$

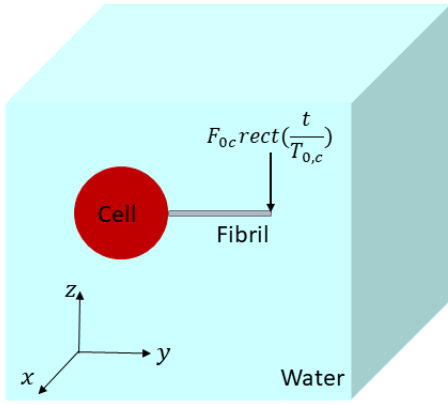
For our problem, by choosing those 45° -wide magnetic plates ($T_p = T/2$), it is expected that $a_n = 0$, for the even values of n ($n \geq 2$). However, since the magnet is volumetric in its nature and is not perfectly identical to magnetic dipole charges, the field suppression does not occur perfectly and then T_p is not equal to $T/2$ (as can be also observed from Figure 2.6). Therefore, $a_n \neq 0$, for

all values of n . Expanding Eq. (A.6), one can easily show that thorough small rotation of magnetic plates from their initial position ($\varphi_0 = \omega_0 T_1$), the fundamental harmonic undergoes no phase variation (because $a_0 \neq 0$). In addition, the 3rd and 5th harmonics will have the same amplitude and phase variation of $-4\varphi_0$. The 7th and 9th harmonics will also undergo a phase variation of $-8\varphi_0$ and so on.

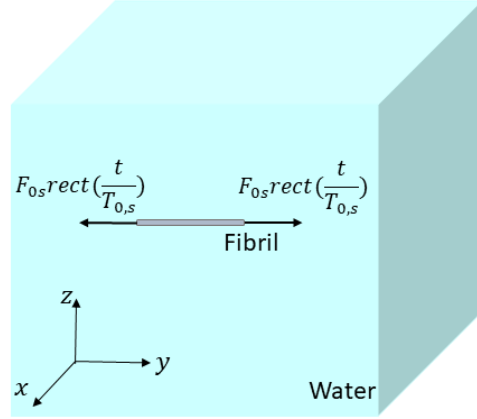
Appendix B: Quality Factor Estimation for Vibration of Amyloid Fibrils in Water as Viscous Medium

From this study, one would be able to unravel the damped behavior of fibrils vibration as they are immersed in water background of biofilm (viscous background) and then find corresponding quality factor, Q . In order to find the Q factor, COMSOL Multiphysics is utilized in this section considering both cantilever beam and spring modes. Figure B.1(a) and Figure B.1(b) illustrate two different scenarios where an amyloid fibril is once attached to a cell membrane (cantilever beam mode) and once is suspended within the biofilm individually (spring mode), respectively. The cell is assumed to be spherical ($r = 440$ nm) and the fibril is modeled as a solid beam with $1 \mu\text{m}$ length having bending rigidity $EI = 0.8 \times 10^{-26} \text{ N.m}^2$ (for the cantilever beam mode) and having Young modulus $E = 25 \text{ GPa}$ (for the spring mode). Water background is assigned to the simulations with dynamic viscosity 1.02 mPa.s . An external force with duration T_0 is applied to the fibril's open-end(s) in time-domain. The motion of the fibril is then monitored. The duration of applied pulse (T_0) is $3 \mu\text{s}$ and 0.5 ns for the cantilever beam mode and the spring mode, respectively. In fact, T_0 is inversely close to the resonant frequency of motion for each mode ($\sim 180 \text{ kHz}$, and $\sim 1 \text{ GHz}$, respectively). Figure B.1(c) and Figure B.1(d) show the time-domain profile of fibril's open-ends vibration. The results are also provided assuming free-space background instead of water. From this figure, the damping effect can be readily captured. The peak of damped vibration can be written as,

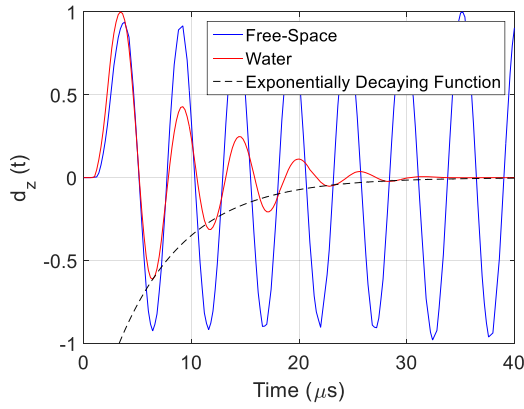
$$d_{peak} = \pm d_0 e^{-\frac{\pi f_0 t}{Q}} \quad (\text{B.1})$$



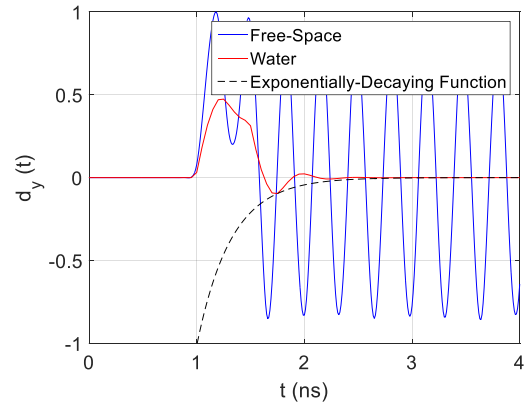
(a)



(b)



(c)



(d)

Figure B.1. The simulation setup for quality factor estimation associated with the fibril vibration. (a): cantilever beam mode (vibration would be mainly along z axis). (b): mechanical spring mode (vibration is mainly along the y axis). Time-domain profile of amyloid fibril's open-end vibration with and without water background. (c): Cantilever beam mode. (d): spring mode. All the amplitudes are normalized to the corresponding one in the free-space.

Where f_0 is the frequency of vibration and Q is the quality factor. Using the information in this figure, the quality factor associated with the cantilever beam mode and the spring mode are found to be 4 and 2.5, respectively.

Appendix C: Radiation Enhancement in Low-Frequency Mechanical Antennas using Magneto-Dielectric Resonance Concept

As we concluded earlier from Eq. (2.7), the EM fields' strength or the amount of power radiated by a mechanical antenna is proportional to the magnet size and its rotation speed. Therefore, to enhance the strength of this radiated field, one can either chose larger magnets or rotate it at a higher speed. Having longer magnet (increasing radius of rotation) increases its moment of inertia and will cause difficulties to create a balanced structure that can withstand the high frequency of rotation. To keep the magnet small, but demanding higher radiated power, additional design considerations are required. The concept for accomplishing the task of increasing radiated power comes from creating an electrically large dipole from a physically-small dipole. This concept can be best explained by considering an electrically small multi-layer magneto-dielectric sphere with a very small time-harmonic dipole (electric or magnetic) at its center as shown in Figure C.1. The fields outside the sphere, at a distance far from it, can be evaluated readily using reciprocity theorem. Basically, the fields (E_1) far away from an electric dipole (J_1) covered by a multi-layer magneto-dielectric sphere is related to the fields at its center (E_2) when illuminated by a short electric dipole (J_2) outside at a distance far from the sphere (which is basically a uniform plane wave) as,

$$\iint \vec{E}_1 \cdot \vec{J}_2 dv = \iint \vec{E}_2 \cdot \vec{J}_1 dv \quad (C.1)$$

In the case of short magnetic dipole, the Eq. (C.1) becomes,

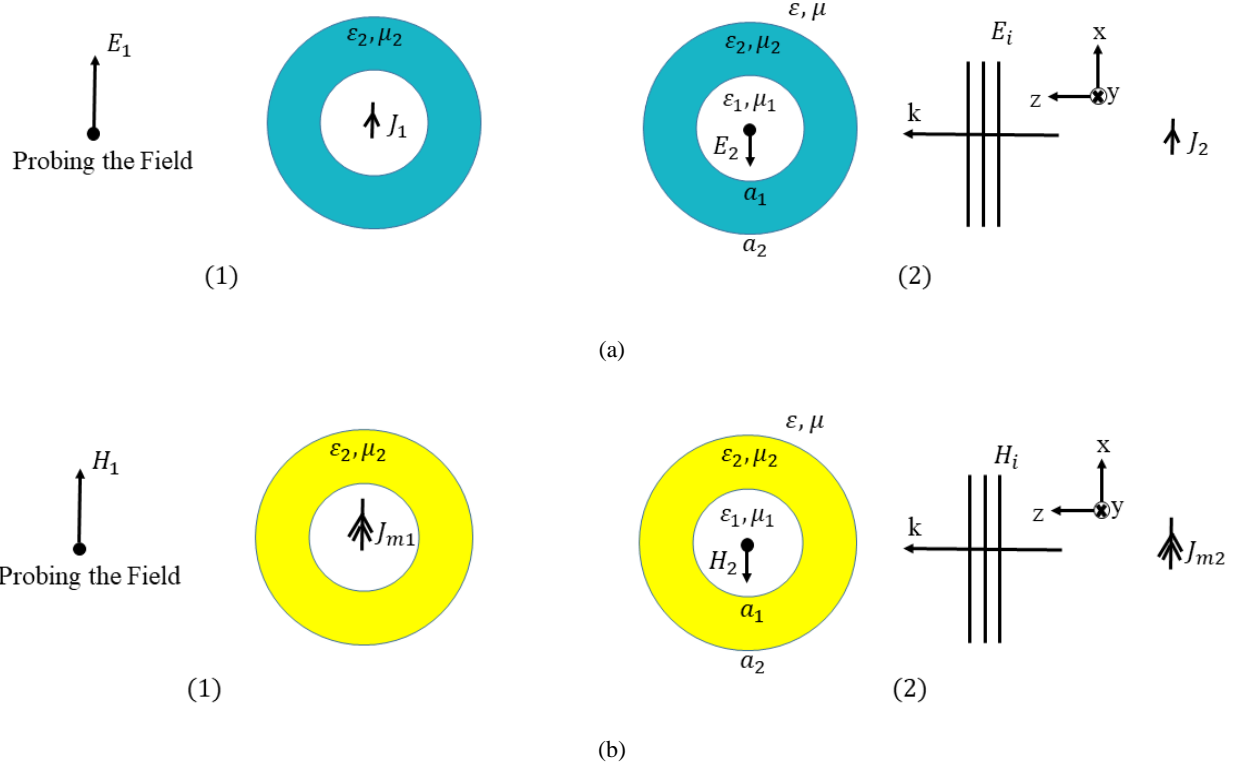


Figure C.1. The short dipole embedded in a multi-layer magneto-dielectric sphere and its dual problem. (a): electric dipole problem. (b): magnetic dipole problem.

$$\iint \vec{H}_1 \cdot \vec{J}_{m2} dv = \iint \vec{H}_2 \cdot \vec{J}_{m1} dv \quad (C.2)$$

In the following, we have developed the analysis for the electric dipole only. One can easily derive the equations for the magnetic dipole using duality relations.

Imagine a magneto-dielectric sphere as shown in Figure C.2 is illuminated by a plane wave. It is well-known that the transmitted electric field at its center has two types of resonances, namely plasmonic resonance and magneto-dielectric resonance [86]. For plasmonic resonance, by considering an electrically small sphere and using quasi-electrostatic approximation, the transmitted electric field at its center is independent of μ_r and is given by [86],

$$E_{center} \approx \frac{3}{\epsilon_r + 2} E_{inc} \quad (C.3)$$

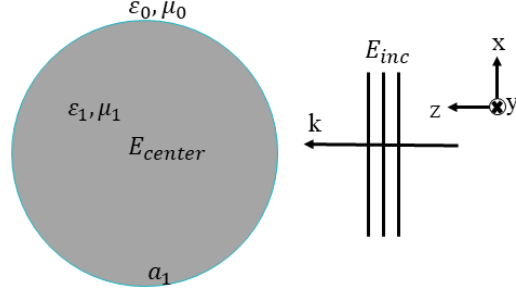


Figure C.2. A magneto-dielectric sphere is illuminated by a plane wave.

where E_{inc} is the field of the incident wave. It is obvious that placement of a dielectric sphere with $\epsilon_r > 1$ will cause reduction of the radiated field. The reason is that the dipole will polarize the dielectric sphere in the opposite direction and cancellation takes place. Field enhancement happens if $\epsilon_r < 1$, this is especially true if the dielectric is negative and $\epsilon_r \sim -2$. This type of resonance is what we call the plasmonic resonance condition. In effect, field of the dipole can be amplified if a negative-epsilon material (NEM) will be realized and placed around our rotating structure which plays the role of a small time-harmonic dipole. NEM has been realized artificially at RF frequencies [160]-[162]. It is well-known that a composite medium made up of periodic arrangement of thin metallic wires acts as a NEM [163]. It is shown that the dielectric constant of the wire medium becomes anisotropic and gets negative values depending on the wire's inductance per unit length (L) and the spacing between (d) them. The spacing between the wires must be in the order of half a wavelength. Since the operating wavelength for the mechanical antennas (VLF band) is around 10 km, it is impossible to take the advantage of plasmonic resonance and realize a NEM at this frequency band. Let us now introduce the magneto-dielectric resonance. For the proof of concept, we have first assumed that the operating frequency is 1 MHz. We will then use the same approach for the VLF band. Consider a plane-wave (fields of a short electric dipole at its far-field) illuminating a 2-layer magneto-dielectric sphere (see Figure C.3(a)) at frequency of 1 MHz. The physical and constitutive parameters of the structure are $\epsilon_1 = \epsilon = \epsilon_0$,

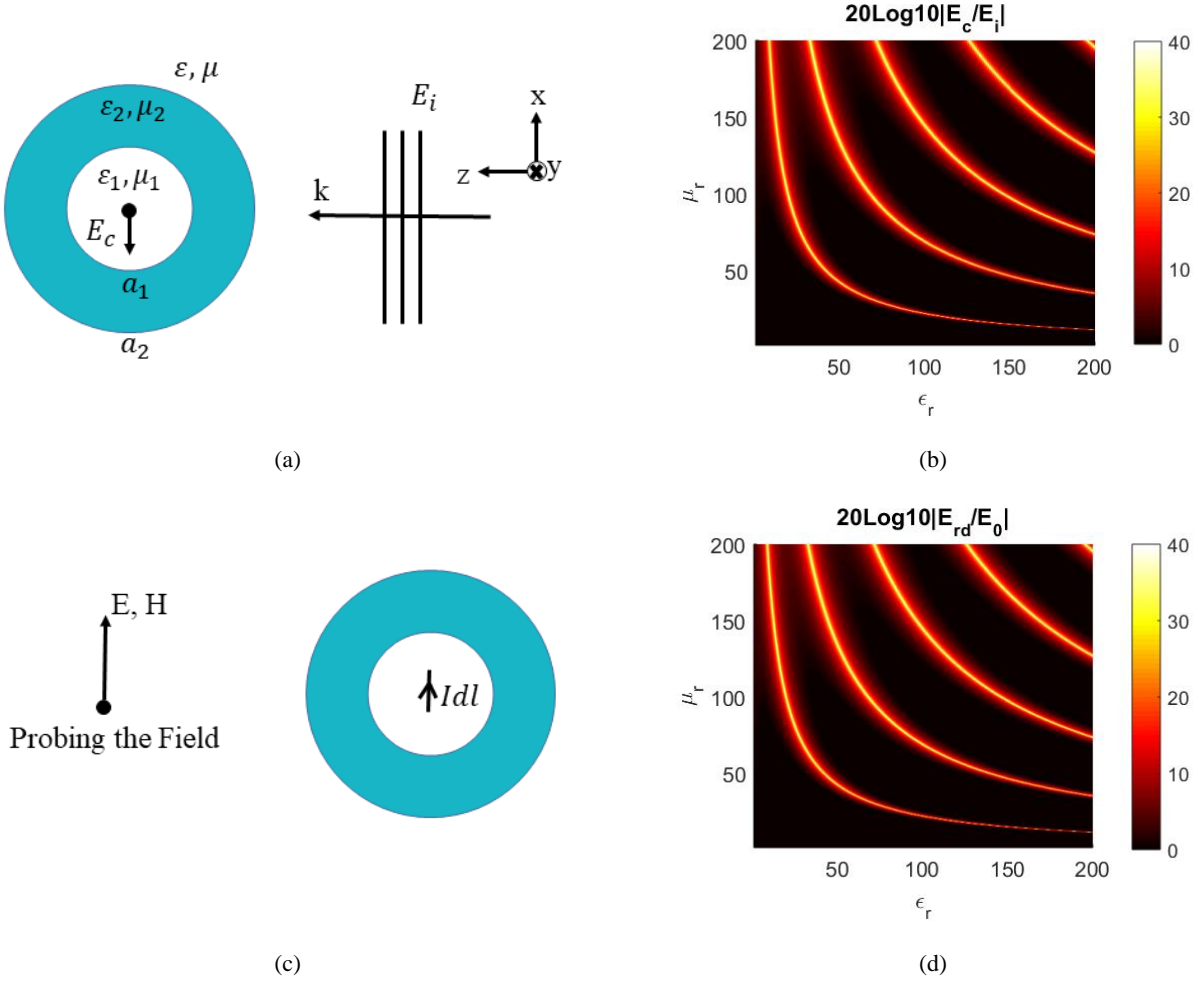
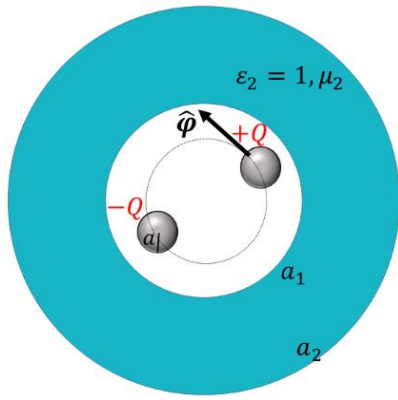


Figure C.3. (a): A 2-layer magneto-dielectric sphere is illuminated by a plane wave. (b): The magneto-dielectric resonance condition for the EM fields at the center of the sphere. (c): A short electric dipole covered by the same multilayer magneto-dielectric sphere. (d): The ratio of far-fields of the dipole with and without the magneto-dielectric material.

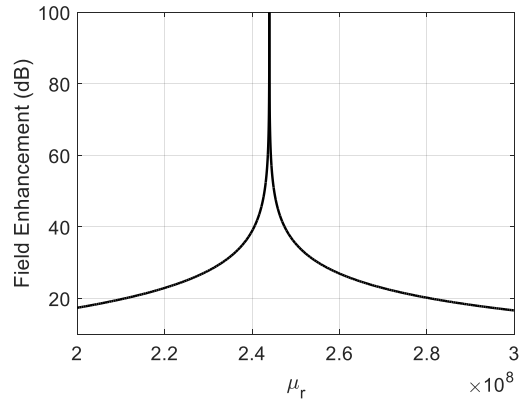
$\mu_1 = \mu = \mu_0$, $\epsilon_2 = \epsilon_r \epsilon_0$, $\mu_2 = \mu_r \mu_0$, and $ka_2 = 0.1$, and $ka_1 = 0.02$ where k is the wavenumber at 1 MHz in the free space. Figure C.3(b) illustrates the ratio of the electric field at the center of the 2-layer sphere to the incident field for various values of ϵ_r and μ_r . As can be concluded from this figure, for specific values of positive ϵ_r and positive μ_r , a resonance happens and approximately 40 dB enhancement for the electric field at the center of the 2-layer sphere could be achieved. In fact, the field enhancement should be infinity if we were to have a material with ϵ_r , and μ_r such that their combination provides a pole for the electric field transmission coefficient [86]. Consequently, it is expected that if a time-harmonic short electric dipole is placed at the

center of a two layer magneto-dielectric sphere with those specified values for ϵ_r and μ_r , as shown in Figure C.3(c), its radiated far-field electric field will enhance approximately by 40 dB. What is physically happening at the resonances is that the overall antenna geometry including the short dipole and the polarized and magnetized dipoles of the sphere resemble a half-wavelength dipole antenna. To verify our analysis and show that how perfectly the reciprocity theorem works, the direct problem itself which is placing a short electric dipole at the center of a 2-layer magneto-dielectric sphere is solved using the same approach as presented in [164], the result of which is depicted in Figure C.3(d). A perfect agreement can be observed between the results from the two approaches.

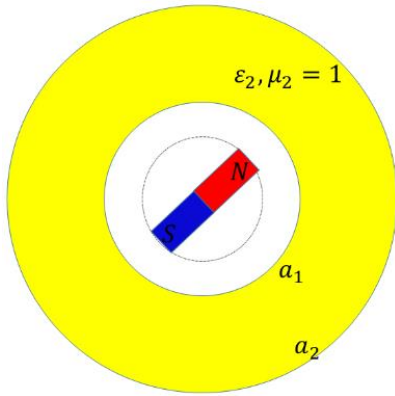
Now, the above approach could be easily exploited to enhance the radiation associated with the rotating electric charges or magnets. It is of course expected to need materials with high permeability, permittivity and/or combination since the radius of rotation in practice is still much smaller than the operating wavelength (30 km). Considering a rotating charged capacitor (or equivalently short electric dipole) at the VLF band ($f=10$ kHz) as shown in Figure C.4(a) with $a_1 = 0.5$ m, and $a_2 = 1$ m, and assuming $\epsilon_r = 1$, its far-field enhancement ratio as a function of μ_r is plotted in Figure C.4(b). It is obvious that by choosing large values for the relative permeability (μ_r), field enhancement of around 100 dB is achieved. Using the duality relations and considering the same magneto-dielectric sphere as above (in terms of dimension), one can also find out that for a rotating magnet, a high permittivity material is required for the field enhancement as shown in Figure C.4(c) and Figure C.4(d).



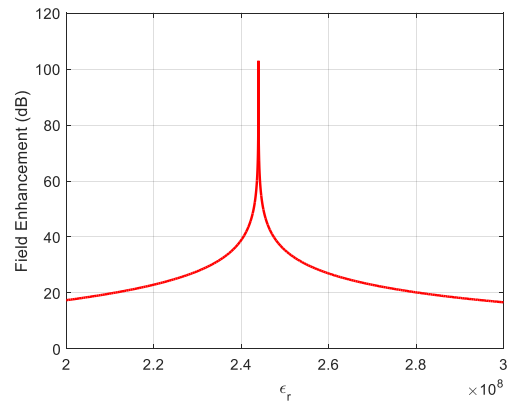
(a)



(b)



(c)



(d)

Figure C.4. (a): The application of magneto-dielectric resonance for enhancing the radiated power from a rotating charged capacitor (electric dipole). (b): The field enhancement as a function of the relative permeability of the material ($\epsilon_r = 1$) covering the rotating capacitor. (c): The application of magneto-dielectric resonance for enhancing the radiated power from a rotating magnet. (d): The field enhancement as a function of the relative permittivity of the material ($\mu_r = 1$).

Bibliography

- [1] W. L. Stutzman, and G. A. Thiele, "Antenna Theory and Design," 3rd ed., Wiley, 2012.
- [2] R. Bansal, "RadioBio," *IEEE Antennas and Propagation Magazine*, vol. 59, no. 3, pp. 117–153, 2017.
- [3] N. Barani, and K. Sarabandi, "Theory of electromagnetic-based communication within bacterial communities," *2019 IEEE International Symposium on Antennas and Propagation and USNC-URSI Radio Science Meeting*, Atlanta, GA, USA, pp. 1-2, 2019.
- [4] Z. Zeng et.al. "A Survey of Underwater Optical Wireless Communications," IEEE Tutorials, 2017.
- [5] J. B. Rhebergen, *et al.*, "Soil moisture distribution around land mines and the effect on relative permittivity," *Proc. SPIE*, vol. 4742, 2002.
- [6] C. A. Balanis, "Advanced Engineering Electromagnetics," 2nd ed., Wiley, 2012.
- [7] A. A. Abdou, *et al.*, "Wireless Sensor Network for underwater communication," *IET Conference on Wireless Sensor Systems (WSS 2012)*, London, pp. 1-6, 2012.
- [8] J. Lioret, S. Sendra, M. Ardid, and J. J. Rodrigues, "Underwater wireless sensor communications in the 2.4 GHz ISM frequency band," *Sensors (Basel)*. vol. 12, no. 4, pp. 4237-4264, 2012.
- [9] https://www.darpa.mil/attachments/AMEBAProposersDay_FINAL.PDF
- [10] N. Barani and K. Sarabandi, "Mechanical Antennas: Emerging Solution for Very-Low Frequency Communication," *2018 IEEE International Symposium on Antennas and Propagation and USNC-URSI Radio Science Meeting*, Boston, MA, USA, 2018.
- [11] M. V. Jamali, J. A. Salehi and F. Akhoundi, "Performance studies of underwater wireless optical communication systems with spatial diversity: MIMO scheme," *IEEE Transactions on Communications*, vol. 65, no. 3, pp. 1176-1192, 2017.
- [12] M. Stojanovic, "Underwater acoustic communications," *Proceedings of Electro/International*, Boston, MA, USA, pp. 435-440, 1995.
- [13] N. Saeed, A. Celik, T. Y. Al-Naffouri, M. S. Alouini, "Underwater Optical Wireless Communications, Networking, and Localization: A Survey," *Arxiv*, 2018.
- [14] J. Zhu, M. A. Antoniades, and G. V. Eleftheriades, "A compact Tri-band monopole antenna with single-cell metamaterial loading," *IEEE Transactions on Antennas and Propagation*, vol. 58, no. 4, pp. 1031-1038, April 2010.
- [15] M. R. Nikkhah, F. T. Dagefu, and N. Behdad, "Electrically-small platform-based antennas for an unmanned ground vehicle," *IEEE Transactions on Antennas and Propagation*, 2020.

- [16] M. A. Kemp, *et al.*, “A high Q piezoelectric resonator as a portable VLF transmitters,” *Nature Communications*, vol. 10, April 2019.
- [17] J. A. Bickford, *et al.*, “Performance of electrically small conventional and mechanical antennas,” *IEEE Transactions on Antennas and Propagation*, vol. 67, no. 4, pp. 2209–2223, 2019.
- [18] W. Hong, K. Baek, Y. Lee, Y. Kim, and S. Ko, “Study and prototyping of practically large-scale mmWave antenna systems for 5G cellular devices,” *IEEE Communications Magazine*, vol. 52, no. 9, pp. 63-69, 2014.
- [19] W. Hong, K. Baek and S. Ko, “Millimeter-wave 5G antennas for smartphones: overview and experimental demonstration,” *IEEE Transactions on Antennas and Propagation*, vol. 65, no. 12, pp. 6250-6261, 2017.
- [20] M. Moosavifar and D. Wentzloff, “A High Gain Lens-Coupled On-Chip Antenna Module for Miniature-Sized Millimeter-Wave Wireless Transceivers,” *2020 International Applied Computational Electromagnetics Society Symposium (ACES)*, Monterey, CA, USA, pp. 1-2, 2020.
- [21] F. T. Dagefu, “Exploitation and mitigation of multipath in complex wave propagation environments for target detection, tracking, and communication,” *Ph.D. Dissertation*, 2012.
- [22] F. T. Dagefu, J. Choi, M. Sheikhsofla, B. M. Sadler and K. Sarabandi, “Performance assessment of lower VHF band for short-range communication and geolocation applications,” *Radio Science*, vol. 50, no. 5, pp. 443-452, 2015.
- [23] J. Choi, F. T. Dagefu, B. M. Sadler, and K. Sarabandi, “Low-power low-VHF Ad-Hoc networking in complex environments,” *IEEE Access*, vol. 5, pp. 24120-24127, 2017.
- [24] C. Pfeiffer, “Fundamental Efficiency Limits for Small Metallic Antennas,” *IEEE Transactions on Antennas and Propagation*, vol. 65, no. 4, pp. 1642-1650, 2017.
- [25] V. Thite, and A. Y. Kazi, “Wideband VHF/UHF antennas for UAV platform with RCS approach,” *2012 1st International Conference on Emerging Technology Trends in Electronics, Communication & Networking*, Gujarat, pp. 1-5, 2012.
- [26] <https://fas.org/irp/agency/army/mipb/1997-2/Pickerin.htm>
- [27] <https://www.cnbc.com/2019/07/26/cargo-drones-could-shape-the-future-of-the-shipping-industry.html>
- [28] H. Rastgoftar, H. G. Kwatny and E. M. Atkins, “Asymptotic tracking and robustness of MAS transitions under a new communication topology,” *IEEE Transactions on Automation Science and Engineering*, vol. 15, no. 1, pp. 16-32, 2018.
- [29] H. Rastgoftar and E. Atkins, “Physics-Based Freely Scalable Continuum Deformation for UAS Traffic Coordination,” *IEEE Transactions on Control of Network Systems*, vol. 7, no. 2, pp. 532-544, 2020.
- [30] <https://futurefive.co.nz/story/mini-drone-swarm-coming-mit-researchers-crack-code-miniaturising-drones>

- [31] N. Barani, and K. Sarabandi, "Antenna bandwidth enhancement using near-field coupled miniaturized elements," *2016 IEEE International Symposium on Antennas and Propagation (APSURSI)*, Fajadro, pp. 1727–1728, 2016.
- [32] N. Barani, J. F. Harvey, and K. Sarabandi, "Fragmented antenna realization using coupled small radiating elements," *IEEE Transactions on Antennas and Propagation*, vol. 66, no. 4, pp. 1725-1735, 2018.
- [33] https://www.cdc.gov/globalhealth/infographics/antibiotic-resistance/antibiotic_resistance_global_threat.htm
- [34] <https://www.who.int/news-room/fact-sheets/detail/antibiotic-resistance>
- [35] B. Perbal, "Communication is the key," *Cell Communication and Signaling*, vol. 1, no. 3, pp. 1-3, 2003.
- [36] J. M. Berg, J. L. Tymoczko, and L. Stryer, "Biochemistry," 5th ed., New York: W H Freeman, 2002.
- [37] B. Alberts, *et al.*, "Molecular biology of the cell," 4th ed., Garland Science, 2002.
- [38] M. B. Miller, and B. L. Bassler, "Quorum sensing in bacteria," *Annu. Rev. Microbiol.*, vol. 55, no. 1, pp. 165-199, 2001.
- [39] L. Zhao, T. Xue, F. Shang, H. Sun, and B. Sun, "Staphylococcus aureus AI-2 quorum sensing associates with the KdpDE two-component system to regulate capsular polysaccharide synthesis and virulence," *Infection and Immunity*, vol. 78, no. 8, pp. 3506-3515, 2010.
- [40] I. A. Khmel, "Quorum-sensing regulation of gene expression: fundamental and applied aspects and the role in bacterial communication," *Microbiology*, vol. 75, pp. 390-397, 2006.
- [41] R. Milo, and R. Phillips, "Cell biology by the numbers," 1st ed., Garland Science, 2015.
- [42] H. K. Diep, E. J. Vigmond, S. S. Segal, and D. G. Welsh, "Defining electrical communication in skeletal muscle resistance arteries: a computational approach," *J. Physiol.*, vol. 3568, no. 1, pp. 267-281, 2005.
- [43] J. Fromm, and S. Lautner, "Electrical signals and their physiological significance in plants," *Plant, Cell and Environment*, vol. 30, pp. 249-257, 2007.
- [44] B. Bean, "The action potential in mammalian central neurons," *Nat. Rev. Neurosci.*, vol. 8, pp. 451-465, 2007.
- [45] L. Montagnier, J. Aïssa, S. Ferris, J. L. Montagnier, and C. Lavallée, "Electromagnetic signals are produced by aqueous nanostructures derived from bacterial DNA sequences," *Interdisciplinary Sciences: Computational Life Sciences*, vol. 1, pp. 81-90, 2009.
- [46] A. Widom, J. Swain, Y. N. Srivastava, and S. Sivasubramanian, "Electromagnetic Signals from Bacterial DNA," *Preprint* at <https://arxiv.org/abs/1104.3113>, 2011.
- [47] M. Cifra, J. Pokorný, D. Havelka, and O. Kučera, "Electric field generated by axial longitudinal vibration modes of microtubule," *Biosystems*, vol. 100, no. 2, pp. 122-131, 2010.
- [48] K. A. Thackston, D. D. Deheyn, and D. F. Sievenpiper, "Electric field generated from microtubule vibrations," *Phys. Rev. E*, vol. 100, pp. 022410, 2019.

- [49] D. Turton, *et al.*, “Terahertz underdamped vibrational motion governs protein-ligand binding in solution,” *Nat. Commun.*, vol. 5, 2014.
- [50] J. Xu, K. W. Plaxco, and S. J. Allen, “Probing the collective vibrational dynamics of a protein in liquid water by terahertz absorption spectroscopy,” *Protein Sci.*, vol. 15, no. 5, pp. 1175-1181, 2006.
- [51] N. Barani, and K. Sarabandi, “Electromagnetic Signaling and Quorum Sensing within Biofilms: Which Mechanism Is the Most Probable Means of Communication?,” *2020 42nd Annual International Conference of the IEEE Engineering in Medicine and Biology Society (EMBC)*, Montreal, QC, Canada, 2020.
- [52] M. E. Davey, and G. A. O’toole, “Microbial biofilms: from ecology to molecular genetics,” *Microbiol. Mol. Boil.*, vol. 64, no. 4, pp. 847-867, 2000.
- [53] M. Avila, D. M. Ojcius, and O. Yilmaz, “The oral microbiota: living with a permanent guest,” *DNA Cell Biol.*, vol. 28, no. 8, pp. 405-411, 2009.
- [54] L. Chen, and Y. M. Wen, “The role of bacterial biofilm in persistent infections and control strategies,” *Int. J. Oral Sci.*, vol. 3, no. 2, pp. 66-73, 2011.
- [55] B. Li, and T. J. Webster, “Bacteria antibiotic resistance: New challenges and opportunities for implant-associated orthopedic infections,” *J. Orthop. Res.*, vol. 36, no. 1, pp. 22-32, 2018.
- [56] <https://eyemicrobiology.upmc.com/PhotoGalleryBiofilms.html>
- [57] Y. Wu, J. Liang, K. Rensing, T. M. Chou, and M. Libera, “Extracellular matrix reorganization during cryo preparation for scanning electron microscope imaging of staphylococcus aureus biofilms,” *Microscopy and Microanalysis*, vol. 20, no. 5, pp. 1348-1355, 2014.
- [58] N. Barani, M. Kashanianfard, and K. Sarabandi, “A Mechanical Antenna with Frequency Multiplication and Phase Modulation Capability,” *IEEE Transactions on Antennas and Propagation*, 2020.
- [59] N. Barani, and K. Sarabandi, “Biological Cell Communication: Quorum Sensing Versus Electromagnetic Signaling,” *2020 IEEE International Symposium on Antennas and Propagation (APSURSI)*, Montreal, QC, Canada, 2020.
- [60] H. Mott, and A. Biggs, “Very-low-frequency propagation below the bottom of the sea,” *IEEE Transactions on Antennas and Propagation*, vol. 11, no. 3, pp. 323-329, May. 1963.
- [61] B. Benhabiles, P. Lacour, M. Pellet, C. Pichot, and A. Papiernik, “A study of VLF antennas immersed in sea water: theoretical, numerical, and experimental results,” *IEEE Antennas and Propagation Magazine*, vol. 38, no. 5, pp. 19-29, Oct. 1996.
- [62] L. Yan, J. Waynert, C. Sunderman, and N. Damiano, “Statistical analysis and modeling of VLF/ELF noise in coal mines for through-the-earth wireless communications,” *2014 IEEE Industry Application Society Annual Meeting*, Vancouver, BC, pp. 1-5, 2014.
- [63] M. Manteghi, “A navigation and positioning system for unmanned underwater vehicles based on a mechanical antenna,” *2017 IEEE International Symposium on Antennas and*

- Propagation & USNC/URSI National Radio Science Meeting*, San Diego, CA, pp. 1997-1998, 2017.
- [64] M. B. Cohen, U. S. Inan, M. Gołkowski, and N. G. Lehtinen, "On the generation of ELF/VLF waves for long-distance propagation via steerable HF heating of the lower ionosphere," *J. Geophys. Res.*, 115, July 2010.
- [65] D. Ciudad, P. C. Arribas, P. Sanchez, and C. Aroca, "RFID in metal environments: An overview on low (LF) and ultra-low (ULF) frequency systems," *Radio Frequency Identification Fundamentals and Applications*, IntechOpen, 2010.
- [66] V. Harid *et al.*, "Magnetic field penetration into a metal enclosure using an ELF/VLF loop antenna," *IEEE Transactions on Electromagnetic Compatibility*, doi:10.1109/TEMPC.2019.2952560.
- [67] H. Y. Kim *et al.*, "Imaging conductive objects through metal enclosures using ELF/VLF magnetic fields," in *IEEE Access*, vol. 8, pp. 79745-79753, 2020,
- [68] R. Azadegan, and K. Sarabandi, "A novel approach for miniaturization of slot antennas," *IEEE Transactions on Antennas and Propagation*, vol. 51, no. 3, pp. 421-429, Mar. 2003.
- [69] N. Behdad, and K. Sarabandi, "Bandwidth enhancement and further size reduction of a class of miniaturized slot antennas *IEEE Transactions on Antennas and Propagation*, vol. 52, no. 8, pp. 1928-1935, Aug. 2004.
- [70] T. Nan, *et al.* "Acoustically actuated ultra-compact NEMS magnetoelectric antennas, vol. 8, Aug. 2017.
- [71] I. F. Akyildiz, P. Wang and Z. Sun, "Realizing underwater communication through magnetic induction," *IEEE Communications Magazine*, vol. 53, no. 11, pp. 42-48, Nov. 2015.
- [72] H. C. Burch, A. Garraud, M. F. Mitchell, R. C. Moore and D. P. Arnold, "Experimental generation of ELF radio signals using a rotating magnet," *IEEE Transactions on Antennas and Propagation*, vol. 66, no. 11, pp. 6265-6272, Nov. 2018.
- [73] M. Moosavifar and D. Wentzloff, "Analysis of Design Trade-Offs in Ultra Low Power FSK Receivers for Phase-Based Ranging," 2021 IEEE Topical Conference on Wireless Sensors and Sensor Networks (WiSNeT), San Diego, CA, USA, 2021.
- [74] J. G. Proakis, M. Salehi, "Fundamentals of Communication Systems," 1st ed., Prentice Hall, 2004.
- [75] D. Dinn, "Underwater communications using a low-frequency magneto-inductive transceiver," *ULTRA ELECTRONICS MARITIME SYSTEMS*, 2008.
- [76] N. Strachen, J. Booske, and N. Behdad, "A mechanically based magneto-inductive transmitter with electrically modulated reluctance," *PLOS ONE*, 2018.
- [77] M. Gołkowski, J. Park, J. Bittle, B. Babaihgari, R. A. L. Rorrer and Z. Celinski, "Novel Mechanical Magnetic Shutter Antenna for ELF /VLF Radiation," *2018 IEEE International Symposium on Antennas and Propagation & USNC/URSI National Radio Science Meeting*, Boston, MA, USA, 2018.
- [78] E. F. W. Alexanderson, "Alternator for one hundred thousand cycles," *Proceedings of the American Institute of Electrical Engineers*, vol. 28, no. 6, pp. 655-668, June 1909.

- [79] J. D. Jackson, "Classical Electrodynamics," 3rd ed., New York, NY: Wiley, 1999.
- [80] <https://www.ansys.com/products/electronics/ansys-maxwell>
- [81] R. F. Harrington, "Time-Harmonic Electromagnetic Fields," Wiley-IEEE Press, September 2001.
- [82] N. Barani and K. Sarabandi, "A Frequency Multiplier and Phase Modulation Approach for Mechanical Antennas Operating at Super Low Frequency (SLF) Band," *2019 IEEE International Symposium on Antennas and Propagation & USNC-URSI Radio Science Meeting*, Atlanta, GA, USA, 2019.
- [83] N. Barani and K. Sarabandi, "A Phase Modulation Scheme for Super-Low Frequency Handheld Mechanical Antennas," *2020 IEEE International Symposium on Antennas and Propagation & USNC-URSI Radio Science Meeting*, Montreal, QC, Canada, 2020.
- [84] Sarabandi, K., and P.F. Polatin, "Electromagnetic Scattering from Two Adjacent Objects," *IEEE Transactions on Antennas and Propagation*, vol. 42, no. 4, pp. 510-517, April 1994.
- [85] Sarabandi, K., J. Choi, A. Sabet, and K. Sabet, "Pattern and Gain Characterization Using Non-Intrusive Very-Near-Field Electro-Optical Measurements over Arbitrary Closed Surfaces," *IEEE Transactions on Antennas and Propagation*, pp. 489-497, vol. 65, no. 2, February 2017.
- [86] J. M. Jin, "Theory and Computation of Electromagnetic Fields," 2nd ed., Wiley, 2010.
- [87] S. Tumanski, "Induction coil sensors—a review," *Measurement Science and Technology*, vol. 18, no. 3, January 2007.
- [88] M. B. Cohen, U. S. Inan and E. W. Paschal, "Sensitive broadband ELF/VLF radio reception with the AWESOME instrument," *IEEE Transactions on Geoscience and Remote Sensing*, vol. 48, no. 1, pp. 3-17, Jan. 2010.
- [89] A. Kulak *et al.*, "Extremely low frequency electromagnetic field measurements at the Hylaty station and methodology of signal analysis," *Radio Science*, vol. 49, no. 6, pp. 361-370, June 2014.
- [90] <http://www.magneticsciences.com/mc90r/>
- [91] Texas Instruments, "100-MHz Low-Noise High-Speed Amplifiers," THS403x datasheet, Jul. 1999 [Revised May 2018].
- [92] Y. Corre and Y. Lostanlen, "Three-Dimensional Urban EM Wave Propagation Model for Radio Network Planning and Optimization Over Large Areas," *IEEE Transactions on Vehicular Technology*, vol. 58, no. 7, pp. 3112-3123, Sept. 2009.
- [93] E. F. T. Martijn, and M. H. A. J. Herben, "Characterization of Radio Wave Propagation into Buildings at 1800 MHz," *IEEE Antennas and Wireless Propagation Letters*, vol. 2, no. 1, pp. 122-125, 2003.
- [94] F.T. Dagefu, G. Verma, C.R. Rao, L.Y. Paul, J.R. Fink, B. Sadler, and K. Sarabandi, "Short-Range Low-VHF Channel Characterization in Cluttered Environments," *IEEE Transactions on Antennas and Propagation*, vol. 63, no. 6, pp. 2719-2727, June. 2015.
- [95] J. Andrusenko, R. L. Miller, J. A. Abrahamson, N. M. Merheb Emanuelli, R. S. Pattay and R. M. Shuford, "VHF General Urban Path Loss Model for Short Range Ground-to-Ground

- Communications*,” *IEEE Transactions on Antennas and Propagation*, vol. 56, no. 10, pp. 3302-3310, Oct. 2008.
- [96] Y. J. Song and K. Sarabandi, “A Simultaneous Dual-Channel Micro-Radio-Repeater for Ad-Hoc Wireless Communication,” *IEEE Transactions on Antennas and Propagation*, vol. 62, no. 6, pp. 3378-3383, June. 2014.
- [97] Y. Song, and K. Sarabandi, “Miniaturized Radio Repeater for Enhanced Wireless Connectivity of Ad-hoc Networks,” *IEEE Transactions on Antennas and Propagation*, vol. 60, no. 8, pp. 3913-3920, August 2012.
- [98] S. M. Alamouti, “A simple transmit diversity technique for wireless communications,” *IEEE Journal on Selected Areas in Communications*, vol. 16, no. 8, pp. 1451-1458, Oct. 1998.
- [99] D. Gesbert, M. Shafi, Da-shan Shiu, P. J. Smith and A. Naguib, “From theory to practice: an overview of MIMO space-time coded wireless systems,” *IEEE Journal on Selected Areas in Communications*, vol. 21, no. 3, pp. 281-302, Apr. 2003.
- [100] D. Tse, and P. Viswanath, “Fundamentals of Wireless Communications,” *Cambridge University Press*, 2005.
- [101] D. Garrido Lopez, M. Ignatenko and D. S. Filipovic, “Low-Profile Tri-band Inverted-F Antenna for Vehicular Applications in HF and VHF Bands,” *IEEE Transactions on Antennas and Propagation*, vol. 63, no. 11, pp. 4632-4639, Nov. 2015.
- [102] T. Y. Shih and N. Behdad, “Bandwidth Enhancement of Platform-Mounted HF Antennas Using the Characteristic Mode Theory,” *IEEE Transactions on Antennas and Propagation*, vol. 64, no. 7, pp. 2648–2659, July. 2016.
- [103] M. Kashanianfard and K. Sarabandi, “Vehicular Optically Transparent UHF Antenna for Terrestrial Communication,” *IEEE Transactions on Antennas and Propagation*, vol. 65, no. 8, pp. 3942-3949, Aug. 2017.
- [104] R. A. Dalke, C. L. Holloway, P. McKenna, M. Johansson and A. S. Ali, “Effects of reinforced concrete structures on RF communications,” *IEEE Transactions on Electromagnetic Compatibility*, vol. 42, no. 4, pp. 486-496, Nov. 2000.
- [105] S. Y. Lim, Q. P. Soo, A. Adam, D. W. G. Lim, Z. Yun and M. F. Iskander, “Towards a Comprehensive Ray-Tracing Modeling of an Urban City With Open-Trench Drains for Mobile Communications,” *IEEE Access*, vol. 5, pp. 2300-2307, 2017.
- [106] H. Mosallaei, and K. Sarabandi, “Antenna miniaturization and bandwidth enhancement using a reactive impedance substrate,” *IEEE Transactions on Antennas and Propagation*, vol. 52, no. 9, pp. 2403–2414, Sept. 2004.
- [107] Y. Chen and C. F. Wang, “Electrically Small UAV Antenna Design Using Characteristic Modes,” *IEEE Transactions on Antennas and Propagation*, vol. 62, no. 2, pp. 535-545, Feb. 2014.
- [108] N. Barani, B. Yektakhah, and K. Sarabandi, “Parasitic antennas for small metallic platforms,” *IEEE International Symposium on Antennas and Propagation & USNC/URSI National Radio Science Meeting*, pp. 1995–1996, 2017.

- [109] K. Sarabandi, J. Oh, L. Pierce, K. Shivakumar and S. Lingaiah, "Lightweight, Conformal Antennas for Robotic Flapping Flyers," *IEEE Antennas and Propagation Magazine*, vol. 56, no. 6, pp. 29-40, Dec. 2014.
- [110] M. S. Sharawi, D. N. Aloï and O. A. Rawashdeh, "Design and Implementation of Embedded Printed Antenna Arrays in Small UAV Wing Structures," *IEEE Transactions on Antennas and Propagation*, vol. 58, no. 8, pp. 2531-2538, Aug. 2010.
- [111] X. Zhao, S. P. Yeo and L. C. Ong, "Planar UWB MIMO Antenna with Pattern Diversity and Isolation Improvement for Mobile Platform Based on the Theory of Characteristic Modes," *IEEE Transactions on Antennas and Propagation*, 2017.
- [112] X. Zhao, B. N. Tian, S. P. Yeo and L. C. Ong, "Wideband Segmented Loop Antenna with Dual-Polarized Omnidirectional Patterns for Mobile Platforms," *IEEE Transactions on Antennas and Propagation*, vol. 56, no. 2, pp. 883-8860, Feb. 2017.
- [113] C.A. Balanis, "Antenna theory: analysis and design," 3rd ed., Wiley, 2005.
- [114] G. Glinski, "Note on Circular Loop Antennas with Non-Uniform Current Distribution," *Journal of Applied Physics*, vol. 18, no. 7, pp. 638-644, 1947.
- [115] D. M. Pozar, "Microwave engineering," 3rd ed., Wiley. 1990.
- [116] Y. Shamis, *et.al*, "Specific Electromagnetic Effects of Microwave Radiation on Escherichia coli," *Applied and Environmental Microbiology*, pp. 3017-3023, 2011.
- [117] H. C. Flemming, T. R. Neu, and D. J. Wozniak, "The EPS matrix: the "house of biofilm cells". *J. Bacteriol.*, vol. 189, no. 22, pp. 7945-7947, 2007.
- [118] N. Van Gerven, S. E. Van der Verren, D. M. Reiter, and H. Remaut, "The role of functional amyloids in bacterial virulence," *Journal of Microbiology*, vol. 430, no. 20, pp. 3657-3684, 2018.
- [119] S. S. Rogers, P. Venema, J. P. M. Van Der Ploeg, E. Van Der Linden, L. M. C. Sagis, A. M. Donald "Investigating the permanent electric dipole moment of β -Lactoglobulin fibrils using transient electric birefringence," *Biopolymers*, vol. 82, pp. 241-252, 2006.
- [120] G. Yoon, J. Kwak, J. I. Kim, S. Na, and K. Eom, "Mechanical characterization of amyloid fibrils using coarse-grained normal mode analysis," *Arxiv*, May. 2011.
- [121] R. N. Rambaran, and L. C. Serpell, "Amyloid fibrils: abnormal protein assembly," *Prion*, vol. 2, no. 3, pp. 112-117, 2008.
- [122] G. Chen, *et.al*, "Amyloid beta: structure, biology and structure-based therapeutic development," *Acta Pharmacol. Sin.*, vol. 38, pp. 1205-1235, 2017.
- [123] N. Salinas, J. P. Colletier, A. Moshe, and M. Landau, "Extreme amyloid polymorphism in Staphylococcus aureus virulent PSM α peptides," *Nat Commun.*, vol. 9, no. 1, pp. 3512, 2018.
- [124] L. Pauling, and R. B. Corey, "Configurations of polypeptide chains with favored orientations around single bonds: two new pleated sheets," *Proc. Natl. Acad. Sci. U S A.*, vol. 37, no. 11, pp. 729-740, 1951.
- [125] Y. Wang, *et.al*, "Anti-biofilm activity of graphene quantum dots via self-assembly with bacterial amyloid proteins," *ACS Nano*, vol. 13, pp. 4278-4289, 2019.

- [126] <https://woundeducators.com/strategies-for-managing-biofilms/>
- [127] E. T. Fligelman, *et.al*, “The cytotoxic *Staphylococcus aureus* PSM α 3 reveals a cross- α amyloid-like fibril,” *Science*, vol. 355, no. 6327, pp. 831–833, 2017.
- [128] P. J. Wyatt, “Cell wall thickness, size distribution, refractive index ratio and dry weight content of living bacteria (*Staphylococcus aureus*),” *Nature*, vol. 226, pp. 277-279, 1970.
- [129] H. H. Tuson, *et.al*, “Measuring the stiffness of bacterial cells from growth rates in hydrogels of tunable elasticity,” *Mol. Microbiol.*, vol. 84, no. 5, pp. 874–891, 2012.
- [130] N. Kandemir, W. Vollmer, N. S. Jakubovics, and J. Chen, “Mechanical interactions between bacteria and hydrogels,” *Sci. Rep.*, vol. 8, pp. 10893, 2018.
- [131] E. Gil-Santos, *et.al*, “Optomechanical detection of vibration modes of a single bacterium,” *Nat. Nanotechnol.*, vol. 15, pp. 469–474, 2020.
- [132] B. Chen, K. R. Thurber, F. Shewmaker, R. B. Wickner, R. Tycko, “Measurement of amyloid fibril mass-per-length by tilted-beam transmission electron microscopy,” *Proc. Natl. Acad. Sci. USA*, vol. 106, pp. 14339–14344, 2009.
- [133] T. Doussineau, *et.al*, “Mass determination of entire amyloid fibrils by using mass spectrometry,” *Angew. Chem. Int. Ed.*, vol. 55, no. 7, pp. 2340-2344, 2016.
- [134] C. A. Van Eysden, and J. E. Sader, “Resonant frequencies of a rectangular cantilever beam immersed in a fluid,” *Journal of Applied Physics*, vol. 100, pp. 114916, 2006.
- [135] T. J. Paul, *et.al*. “Structural and mechanical properties of amyloid beta fibrils: a combined experimental and theoretical approach,” *J. Phys. Chem. Lett.*, vol. 14, pp. 2758-2764, 2016.
- [136] A. K. Chamberlain, *et.al*. “Ultrastructural organization of amyloid fibrils by atomic force microscopy,” *Biophysical Journal*, vol. 79, no. 6, pp. 3282-3293, 2000.
- [137] T. H. X. Zou, *et.al*. “Design and experimental investigation of a magnetically coupled vibration energy harvester using two inverted piezoelectric cantilever beams for rotational motion,” *Energy Conversion and Management*, vol. 148, pp. 1391-1398, 2017.
- [138] A. Deriglazov, “Classical Mechnaics: Lagrangian and Hamiltonian Formalism,” *Springer*, 2017.
- [139] J. E. Sader, “Frequency response of cantilever beams immersed in viscous fluids with applications to the atomic force microscope,” *Journal of Applied Physics*, vol. 84, pp. 64-76, 1998.
- [140] J. X. J. Zhang, and K. Hoshino, “Molecular Sensors and Nanodevices (Chapter 6- Mechanical transducers: *cantilevers, acoustic wave sensors, and thermal sensors*),” *William Andrew Publishing*, pp. 321-414, 2014.
- [141] A. Nafari, H. A. Sodano, “Electromechanical modeling and experimental verification of a direct write nanocomposite” *Smart Materials and Structures*, vol. 28, pp. 045014, 2018.
- [142] T. H. Fay, and S. D. Graham, “Coupled spring equations,” *International Journal of Mathematical Education in Science and Technolog*, vol. 34, no. 1, pp. 65-79, 2003.
- [143] W. E. Thomas, E. Trintchina, M. Forero, V. Vogel, and E. V. Sokurenko, “Bacterial adhesion to target cells enhanced by shear force,” *Cell*, vol. 109, no. 7, pp. 913-923, 2002.

- [144] T. R. H. Kouwen, *et.al*, “The large Mechanosensitive channel MscL determines bacterial susceptibility to the bacteriocin sublancin 168,” *American Society for Microbiology Journals*, vol. 53, no. 11, pp. 4702–4711, 2009.
- [145] A. E. H. Love, “A Treatise on the Mathematical Theory of Elasticity (4th ed.),” *New York: Dover*, 1944.
- [146] L. Saviot, and D. B. Murray, “Longitudinal versus transverse spheroidal vibrational modes of an elastic sphere,” *Phys. Rev. B.*, vol. 72, no. 20, pp. 205433–205438, 2005.
- [147] S. T. Rutherford, and B. L. Bassler, “Bacterial quorum sensing: its role in virulence and possibilities for its control,” *Cold Spring Harbor perspectives in medicine*, vol. 2, no. 11, pp. a012427, 2012.
- [148] L. Keller, and M. Surette, “Communication in bacteria: an ecological and evolutionary perspective,” *Nat. Rev. Microbiol.*, vol. 4, pp. 249–258, 2006.
- [149] F. T. Ulaby, R. K. Moore, and A. K. Fung, “Microwave remote sensing: active and passive,” *Addison-Wesley publishing group*, pp. 105–111, 2015.
- [150] A. B. Goryachev, D. J. Toh, and T. Lee, “Systems analysis of a quorum sensing network: Design constraints imposed by the functional requirements, network topology and kinetic constants,” *Biosystems*, vol. 83, no. 2, pp. 178–187, 2006.
- [151] J. Suzuki, T. Nakano, and M. J. Moore, “Modeling, methodologies and tools for molecular and nano-scale communications (1st edition),” *Springer*, 2017.
- [152] T. Nakano, Y. Okaie, and J. Liu, “Channel model and capacity analysis of molecular communication with Brownian motion,” *IEEE Communications Letters*, vol. 16, pp. 797–800, 2012.
- [153] Q. Liu, and K. Yang, “Channel capacity analysis of a diffusion-based molecular communication system with ligand receptors,” *International Journal of Communication Systems*, vol. 28, pp. 1508-1520, 2015.
- [154] Z. Hu, L. Cheng, and B. J. Berne, “First passage time distribution in stochastic processes with moving and static absorbing boundaries with application to biological rupture experiments,” *J. Chem. Phys.*, vol. 133, pp. 034105, 2010.
- [155] H. C. Berg, “Random walks in biology,” *Princeton University Press*, pp. 12–19, 1992.
- [156] A. E. Lindsay, A. J. Bernoff, and M. J. Ward, “First passage statistics for the capture of a Brownian particle by a structured spherical target with multiple surface traps,” *Multiscale Modeling and Simulation*, vol. 15, pp. 74-109, 2017.
- [157] E. Geisinger, E. A. George, J. Chen, T. W. Muir, and R. P. Novick, “Identification of ligand specificity determinants in AgrC, the *Staphylococcus aureus* quorum-sensing receptor,” *J. Biol. Chem.*, vol. 281, no. 14, pp. 8930-8938, 2008.
- [158] S. Saadat, H. Aghasi, E. Afshari and H. Mosallaei, “Low-Power Negative Inductance Integrated Circuits for GHz Applications,” *IEEE Microwave and Wireless Components Letters*, vol. 25, no. 2, pp. 118-120, 2015.
- [159] M. Fayazi, A. Fotowat, and Z. Kavehvas, “A Simplified Approach to Two-Port Analysis in Feedback,” *arXiv preprint arXiv:1908.10274*, 2019.

- [160] S. E. Lauro, A. Toscano, and L. Vegni, "Symmetrical coupled microstrip lines with epsilon negative metamaterial loading," *IEEE Transactions on Magnetics*, vol.45, no.3, pp. 1182-1185, 2009.
- [161] S. M. Hashemi, M. Soleimani, and S. A. Tretyakov, "Compact negative-epsilon stop-band structures based on double-layer chiral inclusions," *IET Microwaves, Antennas & Propagation*, vol. 7, no. 8, pp. 621-629, 2013.
- [162] B. C. Park, and J. H. Lee, "Omnidirectional Circularly Polarized Antenna Utilizing Zeroth-Order Resonance of Epsilon Negative Transmission Line," *IEEE Transactions on Antennas and Propagation*, vol. 59, no. 7, pp. 2717-2721, 2011.
- [163] S. Tretyakov, "Analytical Modeling in Applied Electromagnetics," *Artech House*, 2003.
- [164] R. W. Ziolkowski, and A. D. Kipple, "Application of double negative materials to increase the power radiated by electrically small antennas," *IEEE Transactions on Antennas and Propagation*, vol.51, no.10, pp. 2626-2640, 2003.